INVESTIGATION OF HARMONIC GENERATION

IN LASER PRODUCED PLASMAS.

by

NAEEM AHMAD SAYED.

A thesis submitted for
the Degree of Doctor of Philosophy
at the University of London.

Department of Physics,
Royal Holloway College,
Egham, Surrey TW20 0EX.

May 1986

INVESTIGATION OF HARMONIC GENERATION

IN LASER PRODUCED PLASMAS

ABSTRACT

A study of harmonic generation in laser produced plasmas is presented. Experiments were performed on Royal Holloway College's carbon-dioxide laser system and on the Rutherford Appleton Laboratory's neodymium-glass laser facility. Various targets were irradiated. The backscattered radiation was spectrally analysed in the vicinity of the incident(w_o) and twice incident frequency($2w_o$).

Optical and x-ray diagnostics were also undertaken.

Theoretical models for harmonic generation in laser produced plasmas by Cairns, Erokhin, Silin and others are reviewed and compared to the experimental results.

It is shown that theories due to Cairns and Silin give reasonable estimates of plasma temperature, from the experimental shift of the second harmonic(2w), though the former requires the plasma density scale-length to be known to a greater accuracy. However, Cairns explains satisfactorily the observed structure of the second harmonic spectra. Other theories account well for the observed dependence of the intensity of the second harmonic to that incident.

Finally, an attempt is made to explain features of the 2w spectrum in terms of plasma motion, resonance absorption, density profile modification and ponderomotive forces.

PREFACE

The work presented in this thesis was carried out, at Royal Holloway College and at the Central Laser Facility at the Rutherford Appleton Laboratory, between October '79 and December '82, under the supervision of Dr. Eric Wooding, to whom I am deeply indebted.

I would like to take this opportunity to thank the technical staff both at RHC and RAL, especially at RHC(particularly Leon Ellison, Reg Elton, Jack Henley & Brian Tait) for their invaluable assistance. Also I would like to thank my colleagues, Derek Brown, Jovan Elazar, John Foley, Phillip Marchington and Yogesh Sudera for their useful discussions, so necessary for conducting any fruitful research. I am grateful to PM and YS in allowing me to quote their results.

Finally, it is a pleasure to thank Culham Laboratory and the Science & Engineering Research Council for their financial assistance and use of the latter's Central Laser Facility at RAL.

This thesis is dedicated

to the memory

of my mother.

CONTENTS

LIST OF FIGURES.

LIST OF TABLES.

CHAPTER ONE

INTRODUCTION

1.1 MOTIVATION

The first serious use of a laser to produce a high density, high temperature plasma were presented by Basov and Krokhin [1] and by Dawson [3] in 1964. Since then much attention has been focused on the interaction of laser radiation with dense plasmas, especially in the context of laser fusion. In this study we shall discuss the mechanisms responsible for harmonic generation, particularly the second harmonic, in laser produced plasmas and relate these to the experimental results. The investigation was made using a neodymium(λ=1.06 μm) and CO_2(λ=10.6 μm) lasers' at RAL & RHC respectively. The laser intensities were high enough above threshold, for second harmonic generation.

Although this work involves only modest irradiances, a brief mention of fusion is appropriate as it is of great significance for the future of Mankind, especially for its energy requirements. Broadly, there are two approaches to this:-

(i) Magnetic confinement of hot plasma,

and (ii) inertial confinement.

Both must satisfy the Lawson's criterion [4]

$$n\tau > 10^{14} \ cm^{-3} sec \qquad (1.1)$$

for scientific breakeven.

One of the inertial confinement approaches is to bombard a pellet containing a mixture of deuterium-tritium fuel with extremely high powered laser beams so that the mixture is compressed to very high densities giving rise to a micro-explosion and thereby release of energy. This results as the fused nucleus, Helium, has a greater binding force then the two constituent nuclei.

1.2 LASER SYSTEMS

A brief description of the technological features of the two high-power laser systems currently employed in plasma production follows: The two main systems are the carbon-dioxide(CO_2) and the neodymium(Nd)-glass laser, the former being pumped by electrical energy, the latter by light from flashlamps in order to achieve a population inversion of the lasing levels. The Nd and CO_2 lasers operate at wavelengths of 1.06 μm and 10.6 μm respectively. A brief specification of the two laser systems used in this study is given in Table 3.1. At present many experiments are conducted with Nd laser systems because of its shorter wavelength and simpler detection techniques. However, problems of handling any high-power beams involves an understanding of many physical processes; viz. self-focusing and filamentation, as they determine the size and shape of amplifiers, especially for solid-state lasers [5].

Self-focusing is very important since it limits the power density in the Nd-glass rods in high power amplifiers. Indeed, self focusing can destroy the expensive rods if it leads to high density spots. The solution to this problem is to reduce the beam energy density by having large diameter rods. Also the glass must be of the highest quality as far homogeneity is concerned and free of any internal stresses.

A laser system is composed of components which prevent light flux feedback from reflections, as they can lead to an unstable and damaging system. Thus the use of either Faraday isolators or saturable dyes or both, where the former rotates the polarisation such that a double transit is suppressed. The dye is used to restrict the minimum oscillator power level.

The technology of CO_2 oscillators and amplifiers is presently undergoing rapid development. Here, the pumping is either via an electrically driven discharge or by the injection of electrons up to relativistic energies. High efficiencies(up to 10%) have been achieved for CO_2 systems.

A schematic of an experimental installation, that at the Rutherford Appleton Laboratory(RAL), is shown in Fig. 3.2. It shows the arrangement of the oscillator, amplifiers, apodizers, Faraday isolators, dye cells and spatial filters, which can produce two beams for laser interaction experiments in Target Area Two(TAII).

There are many other facilities scattered around the World, particularly in the United States, Soviet Union, France and Japan. Table 1.1 lists some of these laser systems and their gross parameters.

1.3 BASIC NOTIONS IN LASER PLASMAS

There are three conditions that an ionised gas must satisfy before being classified as a plasma. These are:-

(a) $\lambda_D << L$, i.e. the plasma must be dense enough such that the Debye length, λ_D, is much smaller than the dimension, L, of a system,

(b) $N_D >>> 1$, i.e. the number of particles within a sphere of radius, λ_D, be greatly in excess of unity,

and (c) $\omega\tau > 1$, i.e. the product of the frequency of plasma oscillations, w, and the mean time between collisions with neutral atoms, τ, be greater than unity.

TABLE 1.1 LASER SYSTEMS

S Y S T E M	LASER /type	NUMBER /beams	ENERGY /J	PULSE t/nsec	POWER /TW
NOVA LLNL, USA	Nd	8-10	100 k	$\leqslant 1$	300
ANTARES Los Alamos, USA	CO_2	24	25 k	$\leqslant 1$	100
RAL England	Nd	2-6	1 k	1	> 3
GARCHING Germany	Iodine	2	100	.3	< 1
Inst. of Plasma Phys. Poland	Nd	4	50-80	1-3	.03
KALMAR Lebedev, USSR	Nd	9	> 150	< 1	> .05
Laser Phys. Lab. Australia	Nd	1	50-100	1	.01
OCTAL France	Nd	8	100	.05	1-2
GEKKO-XII Japan	Nd	12	20 k	.5	40

NOTE : The above figures should only be taken as a rough guide (valid 1980) due to the continuing research and development in this field.

From the above conditions it is seen that plasmas exist in several areas and it is expected that similar theories hold for microwave experiments, explorations of the ionosphere and laser experiments. The corresponding scales of frequency, scale-lengths and applied external fields are shown in Fig. 1.1.

Plasmas can be characterised by the two parameters n_e and T_e; i.e. the electron density and electron temperature respectively. Figure 1.2 shows various plasma sources presently under study at different laboratories. The Figure includes the locus at which the Debye length, λ_D, becomes equal to the mean inter-electron separation, r_{oe}. Finally, the criterion for the electron De-Broglie wavelength(at the most probable thermal speed) to equal r_{oe} is plotted.

Irradiation of a solid target by an intense laser beam creates a hot dense plasma at the surface of the target. The density of this plasma may exceed the 'critical density', n_c, where the plasma frequency, w_p, equals the laser frequency, w_o. The critical density for ruby(λ_{ruby} = 0.6943 μm), CO_2 and Nd laser radiations' are indicated on Fig. 1.2.

The laser beam interacts predominantly with electrons which oscillate strongly in the incident field because of their small mass. At the critical surface the energy is equally shared between the electromagnetic field and the oscillating electrons. The light, therefore, becomes evanescent beyond n_c and is re-radiated in the backward direction by the oscillating electrons. This leads to a transfer of energy from the laser beam to the electrons. Subsequent transfer from electrons to the ions occur near the thermal front at a much higher density.

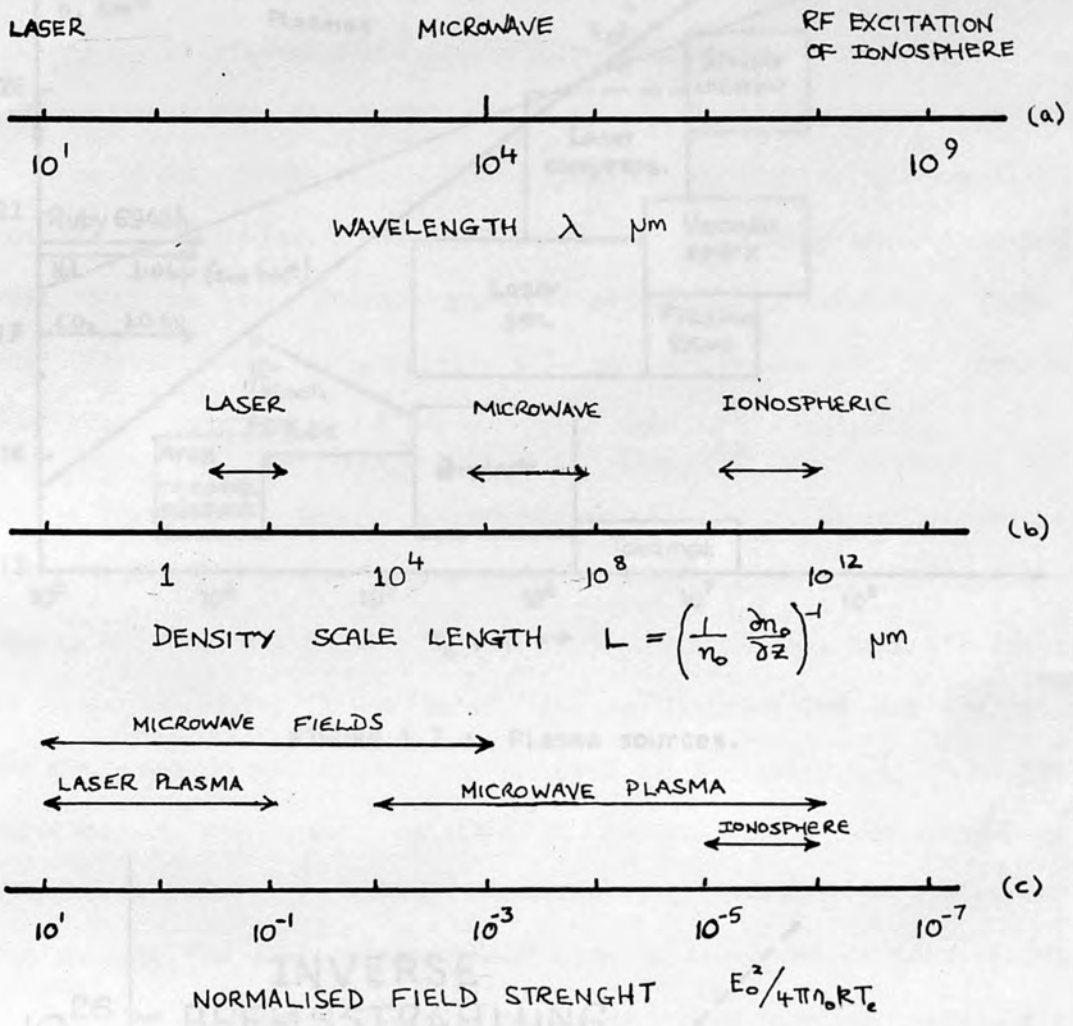

FIGURE 1.1 : A comparison of the experimental parameters, wavelength λ, density scale-length L, and applied external fields E_o^2 for the three cases of interest — laser plasma interactions; microwave simulation, and r-f excitation of the ionosphere. The microwave parameter regime overlaps the laser and ionospheric regimes in L/λ (number of free space wavelengths in a density gradient length) and the normalised field strength $E^2/4\pi n_o T$ where E is the self-consistent field in the plasma.

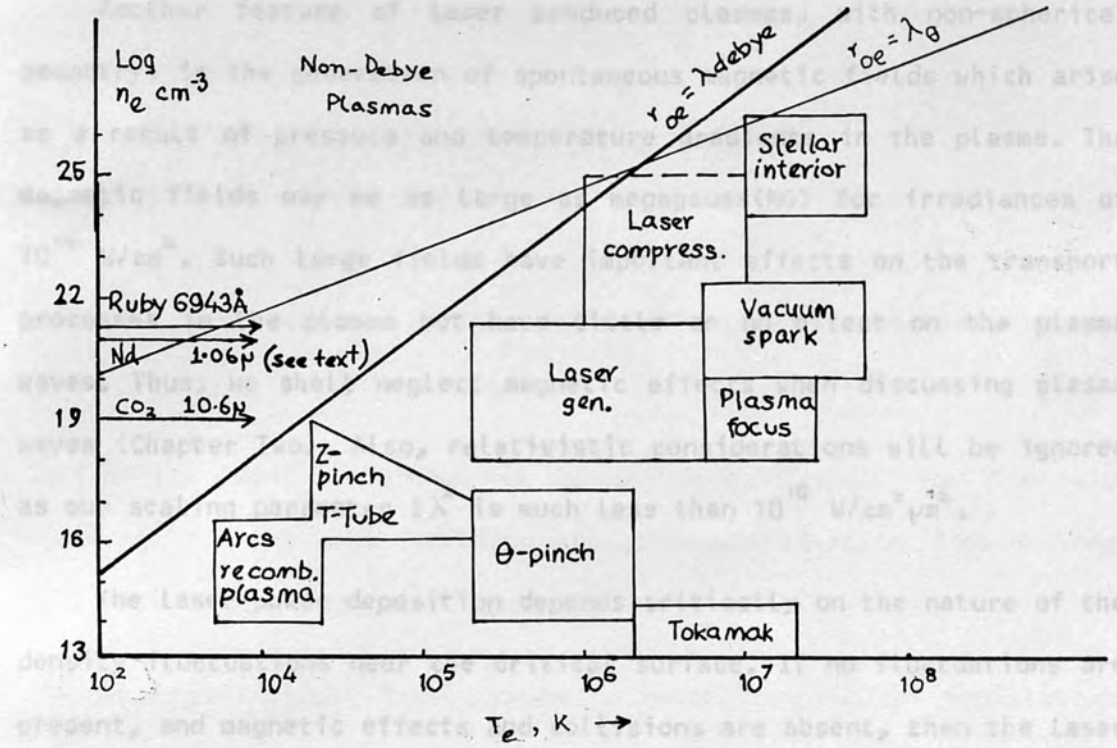

FIGURE 1.2 : Plasma sources.

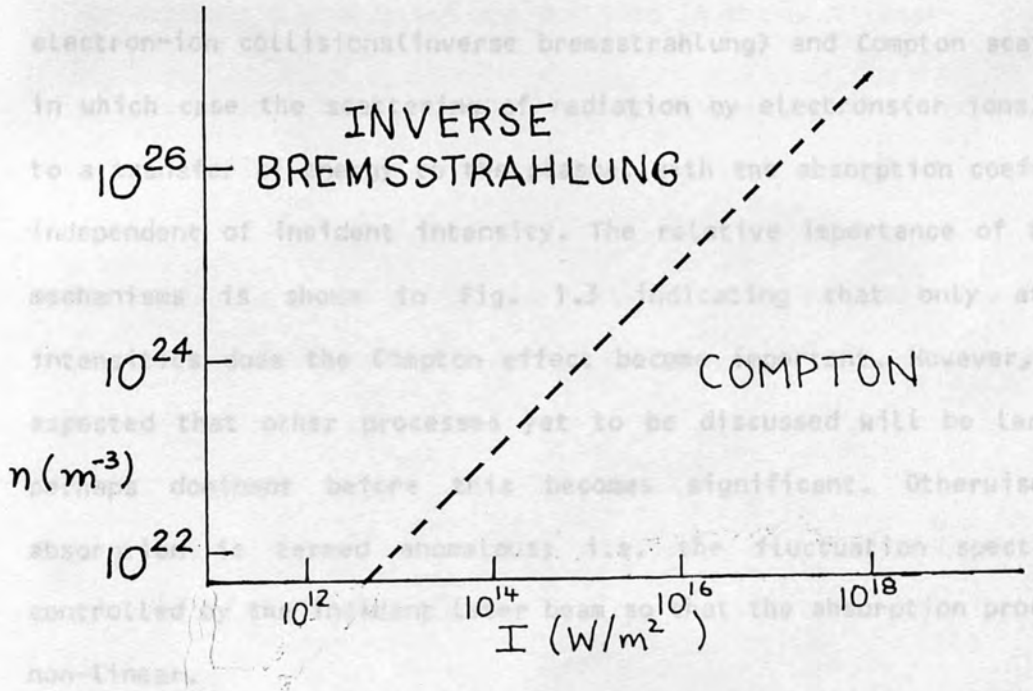

FIGURE 1.3 : The relative importance of inverse bremsstrahlung and Compton scattering at various electron densities(n_e) and incident laser intensity I.

Another feature of laser produced plasmas, with non-spherical geometry, is the generation of spontaneous magnetic fields which arise as a result of pressure and temperature gradients in the plasma. The magnetic fields may be as large as megagauss(MG) for irradiances of 10^{14} W/cm^2. Such large fields have important effects on the transport processes in the plasma but have little or no effect on the plasma waves. Thus, we shall neglect magnetic effects when discussing plasma waves (Chapter Two). Also, relativistic considerations will be ignored as our scaling parameter $I\lambda^2$ is much less than 10^{18} W/cm^2μm^2.

The laser power deposition depends critically on the nature of the density fluctuations near the critical surface. If no fluctuations are present, and magnetic effects and collisions are absent, then the laser beam would be perfectly reflected. If the fluctuations are thermal, then the concomitant absorption is said to be classical; i.e. the absorption of the laser radiation is assumed to be determined by electron-ion collisions(inverse bremsstrahlung) and Compton scattering in which case the scattering of radiation by electrons(or ions) leads to a transfer of energy to the plasma, with the absorption coefficient independent of incident intensity. The relative importance of the two mechanisms is shown in Fig. 1.3 indicating that only at high intensities does the Compton effect become important. However, it is expected that other processes yet to be discussed will be large and perhaps dominant before this becomes significant. Otherwise, the absorption is termed anomalous; i.e. the fluctuation spectrum is controlled by the incident laser beam so that the absorption process is non-linear.

A homogeneous electron and ion gas at T=0°K has collective modes at w_{pe} and w_{pi}, the electron-plasma oscillations and ion-plasma

oscillations respectively. A homogeneous plasma at temperature, T, supports three oscillation modes:-

(i) Transverse oscillations, at w_t

(ii) longitudinal high-frequency oscillations(langmuir waves), at w_l

and (iii) longitudinal low-frequency oscillations(ion-acoustic waves), at w_s

In the limit of increasing wavevector k, $w_s \rightarrow w_l$, the dispersion relations for the longitudinal oscillations, derived by Bohm & Gross [2], have been sketched in Figure 2.7.

At high incident laser intensity these longitudinal oscillations mainly provide the dominant absorption(anomalous) mechanism. Though many of the processes occur at the critical density(see Fig. 2.6), there are others that may dominate the absorption at $n_c/4$. Some of these absorption mechanisms are outlined in the next chapter.

Note that a key parameter in any discussion of radiation plasma interactions is the 'critical density', n_c, defined by

$$4\pi n_c e^2/m_e = w_o^2 \qquad (1.2)$$

where w_o is the frequency of the incident radiation. Normally incident light cannot penetrate beyond that defined by (1.2). We can re-write the above as

$$n_c\ (cm^{-3}) = 1.1*10^{21}\lambda^{-2}\ (\mu m) \qquad (1.3)$$

i.e. the critical density scales as the square of the reciprocal of wavelength of incident radiation.

1.4 SUMMARY OF CONTENTS

Although this report is primarily concerned with harmonic generation in laser produced plasmas, a brief outline of laser systems and an introduction to plasma physics would be of great benefit. This is presented in the following sections.

The theoretical basis of harmonic generation and associated interactions is presented in Chapter Two(**§2**). In the subsequent two chapters the experimental treatment and results are discussed in detail in relation to the theory presented earlier in **§2**. Finally appropriate conclusions are drawn.

REFERENCES :

1. Basov,N.G. & Krokhin,O.N. (1964) Sov. Phys.--JETP **19**,123

2. Bohm,D. & Gross,E.P. (1949) Phys. Rev. **75**,1851 & 1864

3. Dawson,J.M. (1964) Phys. Fluids 7,981

4. Lawson,J.D. (1957) Proc. Phys. Soc.(London) **B70**,6

5. Whitman,G.B. (1974) " Linear & Nonlinear Waves " Wiley Interscience, New York

CHAPTER TWO

THEORETICAL BASIS

2.1 INTRODUCTION

Recently, considerable attention has been focused on laser-induced-fusion schemes [129]. The interaction of intense laser radiation with a dense plasma is one of the most interesting phenomena in laser plasma research [21]. As a pre-requisite for economic power production, absorption in laser irradiated solid targets is a particularly important problem (§2.2). The dominant contribution to classical absorption of the light occurs [49] where the laser frequency is near the plasma frequency, and most collisionless mechanisms responsible for the anomalous absorption and reflection [51,77] are enhanced there. Indeed, the radiation-plasma interaction is sensitive to the homogeneity scale-length of the critical-density plasma [49,51,77]. Characterisation of this region (see Figure 2.6) in high energy experiments is therefore crucial to the understanding of laser-plasma physics.

The literature [25,28-9,39,56,59-61,148,156] strongly suggests that the origin of the second-harmonic light (§2.5) is in the region of the critical-density plasma, $n_c \sim 10^{21}$ cm^{-3} for $\lambda = 1$ μm ($n_c \sim 10^{19}$ cm^{-3} for $\lambda = 10.6$ μm) or $w_o = 2*10^{15}$ Hz. Nonlinear beating between the electron plasma waves at $w_p \sim w_o$ and the laser at w_o can be expected to emit $2w_o$ radiation from the inhomogeneous plasma (§2.5). The plasma waves at $w \sim w_o$ can result from either resonance absorption (§2.2.2) or nonlinear parametric processes (§2.2.3). Similarly the $3w_o/2$ light is likely to be emitted from the quarter-critical density (§2.6) [25,29], $n = n_c/4$, as a result of coalescence between the laser and plasma waves at $w_o/2$ arising from Stimulated Raman Scattering (§2.4) and two-plasmon decay instability (§2.2.3).

These harmonic signals leave the plasma normal to the density gradient as they are launched at densities well below their respective cut-offs, $4n_c$ for 2w and $9/4n_c$ for 3w/2. At the cut-off density (**§2.2**) the local plasma frequency, w_p (2.1), equals the incident frequency, w_o. This then becomes a reflection point, as the refractive index, n_{ref}, becomes zero (2.3) preventing further penetration of the incident wave

$$w_p^2 = 4\pi n_e e^2/m_e \tag{2.1}$$

at cut-off,

$$n_c = m_e w_o^2 / 4\pi e^2 \tag{2.2}$$

$$n_{ref} = (1 - w_p^2 / w_o^2)^{1/2} \tag{2.3}$$

Laser produced plasmas have been found to be rich sources of harmonics of the incident light (**§2.5**). The large electrostatic field near the critical density excited by resonant absorption can generate, by interaction with the incident radiation field, even higher harmonics of the incident light (**§2.5.5**).

In the following sections various absorption and conversion mechanisms operating in laser produced plasmas are examined. Their significance to harmonic generation, backscatter and reflectivity are also discussed.

2.2 ABSORPTION PROCESSES

Before examining the generation phenomena, it is important to understand the processes by which radiation is absorbed in the plasma and converted to other wave modes.

A plasma can absorb electromagnetic radiation either via a linear,

collisionless process such as resonance absorption or a nonlinear one, for example inverse bremsstrahlung. We shall now briefly discuss these processes with references to more detailed work.

2.2.1 INVERSE BREMSSTRAHLUNG

The lowest order absorption mechanism in laser plasmas is simply collisional or inverse bremsstrahlung absorption [49,69,101]. This should be evaluated before proceeding to higher order, collective processes as it may be important in allowing a weak precursor of a pulse to ionise the target. Basically the incident photon excites an electron which in turn interacts with the ion by Coulomb interaction. The low intensity expression for the collisional absorption coefficient is [149]

$$a_\omega = w_p^2 \nu_{ei} / 4\pi w_o^2 \qquad (2.4)$$

where the electron-ion collision rate for momentum transfer is,

$$\nu_{ei} = 4/3\sqrt{2\pi} * (n_e e^4 Z / m_e^2 v_t^2) \ln\Lambda \qquad (2.5)$$

and the plasma frequency

$$w_p^2 = 4\pi n_e e^2 / m_e, \qquad (2.6)$$

n_e is the electron density, Z is the effective charge, w_o is the laser frequency, m_e is the electron mass,

$$v_t = (T_e / m_e) \qquad (2.7)$$

is the mean electron thermal speed, T_e is the electron temperature in electron-volts and $\ln\Lambda$ is the Coulomb logarithm. Absorption increases with density and inversely with temperature.

The electric field, a part of the incident light, of amplitude E_o causes the electrons to 'quiver' at a velocity of amplitude

$$v_o = eE_o / m_e w_o \qquad (2.8)$$

The field strength parameter, η, is defined as:-

$$\eta = v_o / v_t \qquad (2.9)$$

For $\eta>1$, the intensity dependence of inverse bremsstrahlung due to the oscillating velocity of electrons in a laser field can lead to a reduction of the collision absorption efficiency. However, for the range of intensities used here, $\eta<1$, this problem does not arise. Calculation of the absorption rate (a_ω) from the effective electron-ion collision frequency (ν_{eff}), have concentrated on classical [46,149] and quantum [32,34,68,132,135] expressions. This is now discussed in relation to recent work.

Noting that the collision frequency, e.g. (2.5)

$$\nu_{ei} \propto \langle v^2 \rangle^{-3/2} \qquad (2.10)$$

where $\langle\ \rangle$ represents an averaged effect, and that in (2.4) only the thermal velocity component was considered. If the electron motion in an electromagnetic field is taken into account, then

$$\langle v^2 \rangle = v_t^2 + \langle 1/3 v_o^2 \rangle \qquad (2.11)$$

For $\eta \gtrsim 1$ it is expected that

$$\nu_{eff} = \nu_{ei}(1+\tfrac{1}{3}\eta^2)^{-3/2} \qquad (2.12)$$

Comparison of (2.12) with Brysk's [31] numerical results reveal agreement of the electron-ion collision frequency to be within 10% up to values of $\eta=10$. Also (2.12) indicates the collision frequency to scale as v_o^{-3} or E_o^{-3} or $I_o^{-3/2}$ and thus expect that absorption by inverse bremsstrahlung to drop off rapidly with intensity I_o; for example $\eta>1$ implies absorption to be down by a factor of two from its low intensity value in (2.4). The consequence of this will be made apparent later (**§4**).

The density scale-length variation of inverse bremsstrahlung has been discussed by Faehl & Roderick [69] and is seen to be significant

only where the scale-lengths are longer than a few wavelengths ($L>>\lambda_o$). This results in an inhomogeneous standing wave pattern, which is shown [129] to be remarkably close to an Airy pattern [78,51], for a wide range of conditions. The paper [69] also examines the intensity modifications induced by this nonuniform standing wave in the plasma both by a simple analytic model and exact 1-D calculations. Figure 2.1 shows the dependence of the absorption coefficient with scale-length for field strength parameter $\eta=1$. The solid line represents the evaluated results from model equations [69].

In conclusion, it has been shown that the absorption coefficient is dependent on the field strength parameter, η, and consequently on the irradiance as

$$a_\omega \propto I^{-3/2} \qquad (2.13)$$

Also the absorption is seen to be stronger in regions of large density scale-lengths.

2.2.2 RESONANCE ABSORPTION

Elementary plasma physics indicates many phenomena to be independent of particle collisions. One such phenomenon is the conversion of an electromagnetic wave into an electrostatic wave by a 'linear process'. This is a general effect, but the most dramatic form occurs in laser plasma interactions although it was first discussed in connection with the propagation of radio waves in the ionosphere (c.f. Budden [31], Denisov [49], Piliya [134] & Ginzburg [76]). The ideas behind the mechanism are quite simple though a full discussion requires some rather lengthy algebra; hence the abbreviated explanation:-

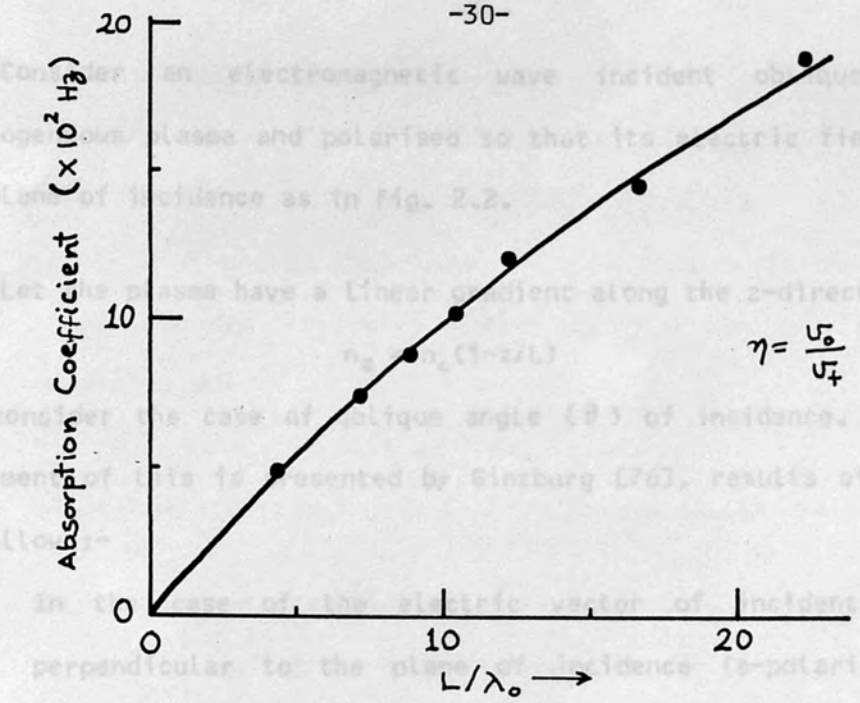

FIGURE 2.1 : Calculated absorption coefficient as a function of normalised scale-length(see text).

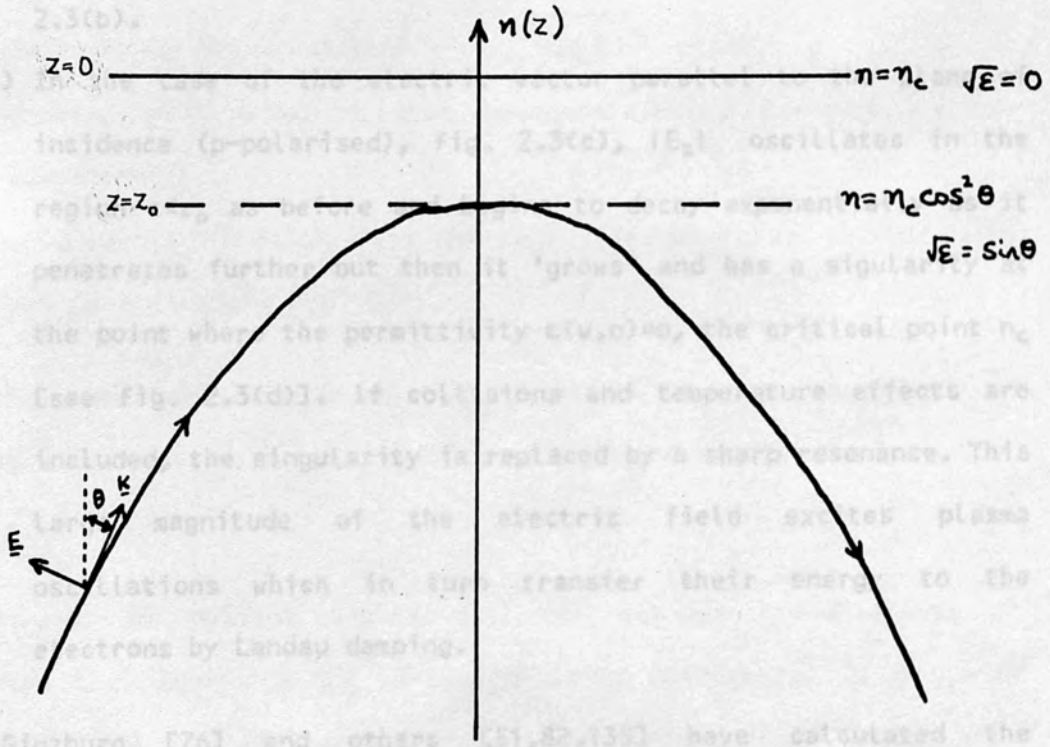

FIGURE 2.2 : P-polarised EM wave incident on plasma.

Consider an electromagnetic wave incident obliquely on an inhomogeneous plasma and polarised so that its electric field lies in the plane of incidence as in Fig. 2.2.

Let the plasma have a linear gradient along the z-direction,

$$n_e = n_c(1-z/L) \qquad (2.14)$$

and consider the case of oblique angle (θ) of incidence. A detailed treatment of this is presented by Ginzburg [76], results of which are as follows:-

(i) In the case of the electric vector of incident radiation perpendicular to the plane of incidence (s-polarised), Fig. 2.3(a), $|E_x|^2$ oscillates in the region $z<z_o$, where the refractive index, n_{ref}, is

$$n_{ref} = \sqrt{\varepsilon(w,z)} = \sin\theta \qquad (2.15)$$

For $z>z_o$ the electric field decay exponentially as in Fig. 2.3(b).

(ii) In the case of the electric vector parallel to the plane of incidence (p-polarised), Fig. 2.3(c), $|E_z|$ oscillates in the region $z<z_o$ as before and begins to decay exponentially as it penetrates further but then it 'grows' and has a sigularity at the point where the permittivity $\varepsilon(w,o)=o$, the critical point n_c [see Fig. 2.3(d)]. If collisions and temperature effects are included, the singularity is replaced by a sharp resonance. This large magnitude of the electric field excites plasma oscillations which in turn transfer their energy to the electrons by Landau damping.

Ginzburg [76] and others [51,82,135] have calculated the penetration depth z_o to be strongly dependent on the angle of incidence, θ_o. Taking a linear variation of the dielectric constant,

$\varepsilon'(z)$, of the plasma as

$$\varepsilon'(z) \approx 1 - 4\pi e^2 n(z)/mw\ (1+i\nu_{eff}/w) \qquad (2.16)$$

for $w^2 >> \nu_{eff}$

$$= \varepsilon(z) - i(w_p^2/w^2)\ \nu_{eff}/w \qquad (2.17)$$

where e,m is the charge and mass of electron, n_e is the electron density, ν_{eff} is the effective number of electron collisions with neutral molecules and

$$w_p^2 = 4\pi e^2 n/m_e \qquad (2.18)$$

is the natural oscillation frequency of plasma oscillations.

For a slow linear variation of $\varepsilon(z)$ along z,

$$\varepsilon'(z) = -az - i\nu_{eff}/w \qquad (2.19)$$

(where a>0 ; so for z>0, $\varepsilon(z)<0$)

At the resonance point where $\varepsilon(z)=0$, the magnitude of the electric field strength $|E_z|$ is given as

$$|E_z| = \varphi(\tau)/[\sqrt{2\pi p}\ |(az+i\nu_{eff}/w)|] \qquad (2.20)$$

where $p=wc/a=k_oL$, $t=p^{1/3}\alpha = (w/ca)^{1/3} \sin\theta_o = (k_oL)^{1/3} \sin\theta$

c-speed of light, a-plasma homogeneity=1/L, where L is the scale-length.

and the Ginzburg function $\varphi(\tau)$ is expressed in terms of the Airy functions (see Ginzburg [76] §20).

The dependence of the maximum value of $|E_z|$ on the angle of incidence is thus given by the function $\varphi(t)$, which is shown in Fig. 2.4.

A plot of optimum angles, θ_m, for various scale-lengths at neodymium (λ=1.06μm) and CO_2 (λ=10.6μm) laser wavelengths is shown in Fig. 2.5. The Figure indicates optimum angles around 7° increasing with decreasing scale-length and always being larger in the case of CO_2 laser radiation.

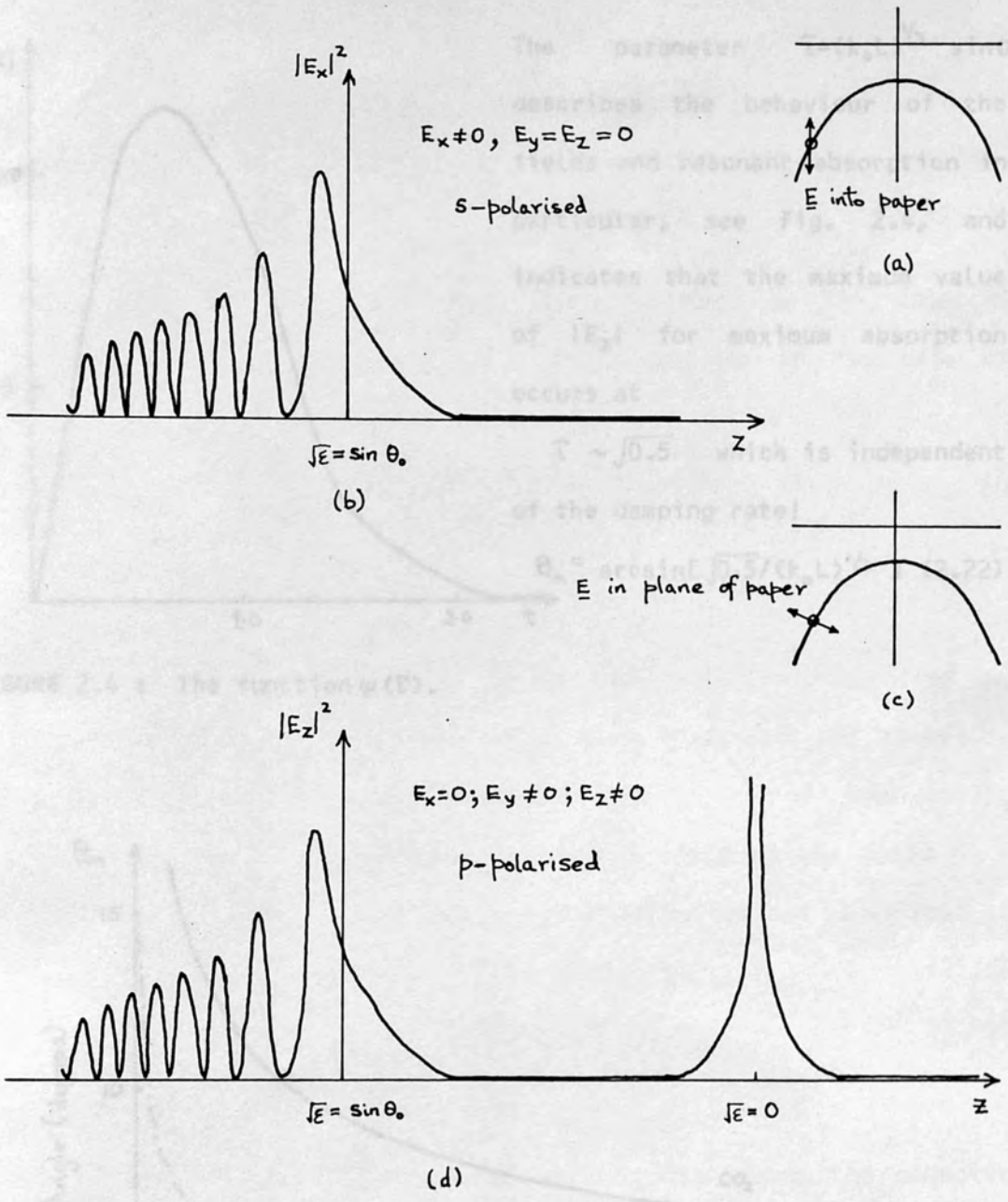

FIGURE 2.3 : Electric field component when an incident wave at angle θ_0 is reflected from an inhomogeneous layer with a linear density gradient.

(a) & (b) s-polarised wave with electric vector perpendicular to the plane of incidence.

(c) & (d) wave with electric vector in plane of incidence(p-polarised).

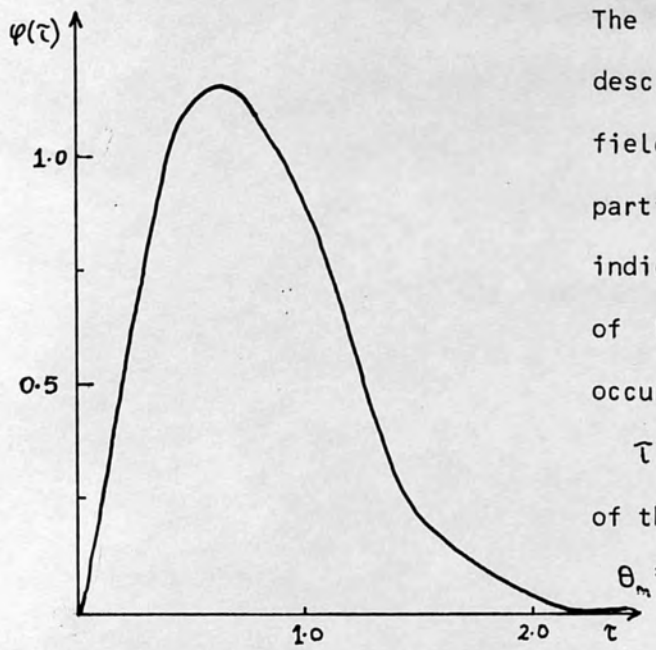

The parameter $\tilde{\tau}=(k_o L)^{1/3}\sin\theta$ describes the behaviour of the fields and resonant absorption in particular, see Fig. 2.4, and indicates that the maximum value of $|E_z|$ for maximum absorption occurs at

$\tilde{\tau} \sim \sqrt{0.5}$ which is independent of the damping rate!

$$\theta_m = \arcsin[\sqrt{0.5}/(k_o L)^{1/3}] \quad (2.22)$$

FIGURE 2.4 : The function $\varphi(\tilde{\tau})$.

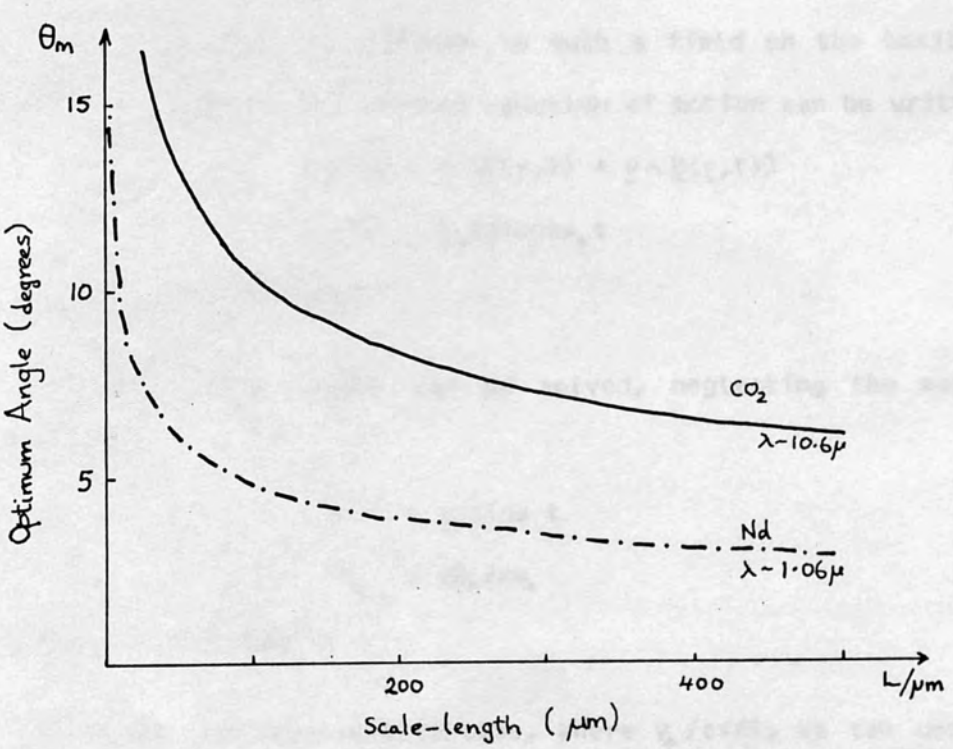

FIGURE 2.5 : Optimum angles for resonance absorption versus scale-length for Nd and CO_2 laser wavelengths.

The maximum value of the electric field,

$$|E_z| = 1.2\, w/\sqrt{2\pi\rho}$$

$$= 1.2\, w(2\pi k_o L)^{-1/2} / \nu_{eff} \qquad (2.23)$$

and the effective dimension of the resonance region from eqn(2.19) is

$$\Delta z = \nu_{eff} / wa = L\, \nu_{eff} / w \qquad (2.24)$$

The effect of resonance absorption is that in the case of p-polarised light, absorption is twice as much as in the case of s-polarised light.

PONDEROMOTIVE FORCE :

From the above discussion it is clear that the process of resonance absorption gives rise to a very localised and therefore spatially inhomogeneous electrostatic field. It is of interest to examine the behaviour of a plasma in such a field on the basis of a single particle model. The Lorentz equation of motion can be written as

$$m\,dv/dt = e\,[\underline{E}(\underline{r},t) + \underline{v} \wedge \underline{B}(\underline{r},t)] \qquad (2.25)$$

where

$$\underline{E}(\underline{r},t) = E_o(\underline{r})\cos w_o t \qquad (2.26)$$

and B is the magnetic field.

To lowest order (2.25) can be solved, neglecting the magnetic field to give

$$\underline{v} = \underline{v}_o \sin w\, t \qquad (2.27)$$

where

$$v_o = eE_o / mw_o \qquad (2.28)$$

is the 'quiver velocity'.

Taking the non-relativistic case, where $v_o/c \ll 1$, we can use $\underline{v}^{(1)}$ to solve to next order taking into account the inhomogeneity of the field and expanding E(r) about the initial position of the electron,

i.e.

$$\underline{E}(\underline{r}) = E(r_o) + (d\underline{r}.\nabla)\underline{E} + \ldots \qquad (2.29)$$

$$d\underline{r} = \int \underline{v}^{(1)}\, dt = -eE_o \cos w_o t/mw_o^2 \qquad (2.30)$$

So to second order

$$m dv^{(2)}/dt = e[(d\underline{r}.\nabla)\underline{E}(r_o) + \underline{v}^{(1)} \wedge \underline{B}(r_o)]$$

$$= -(e/mw_o^2)[(E_o.\nabla)E \cos^2 w_o t + E_o \wedge \nabla \wedge E_o \sin^2 w_o t] \qquad (2.31)$$

Time-averaging this equation gives an expression for the secular force acting on the electron,

$$\langle \underline{F} \rangle = (-e^2/mw_o^2)\,[\,(E_o.\nabla)\,E_o + \underline{E}_o \wedge \nabla \wedge \underline{E}_o\,] \qquad (2.32)$$

parametric instabilities / Drift along $\underline{k}$

The first term in (2.32) is due to the excursions of the electron in its oscillation into regions of differing field strength. This term vanishes if the electromagnetic wave is incident normally on an inhomogeneous plasma. The second term is due to the magnetic field of the incident radiation which distorts the orbit of the electron and causes a small drift of the electron in the direction of the wave.

Re-writing (2.32) as

$$\langle \underline{F} \rangle = -[e^2/4mw_o^2\,]\nabla(\underline{E}_o.\underline{E}_o) = -(e^2/2mw_o^2)\nabla \langle E^2 \rangle \qquad (2.33)$$

and summing over all the electrons in unit volume gives $\langle n_o F \rangle = \langle F_{PM} \rangle$, the ponderomotive force, i.e.

$$\langle F_{PM} \rangle = -(w_p^2/w_o^2)\nabla(E^2/8\pi) \qquad (2.34)$$

There is a corresponding force on the ions which is m_i/m_e times smaller and is transmitted to the ions via the self-consistent fields provided F_{PM} varies with time more slowly than the ion plasma frequency.

Thus have now established that there will be powerful ponderomotive forces acting on the plasma as a consequence of the resonant fields at the critical surface, n_c. The outcome of this is the

expulsion of the plasma from the region of the critical surface leaving behind it some sort of a cavity. Evidence for such a cavity formation was first obtained from computer simulations at Livermore [24]. The cavity formation results in a steep density profile with plasma pressure gradients being balanced by the ponderomotive force [66,71-2,142].

The implication, of the above, can lead to density jumps from $1/2n_c$ to $2n_c$ over a distance of a wavelength, which in turn can lead to strong resonance absorption [13,15,61-2,82,111,126,131] with peaks over a wide range of angles! This can also result in electron heating [62,73-4] and high magnetic fields [121,149,151,155]. Other theoretical treatment for resonance absorption also exists [97,110,115,120,143], most of which take the effect of density profile into account.

2.2.3 PARAMETRIC PROCESSES

A pump field oscillating at frequency w_o with a mode of oscillation at w_1, which can couple to the pump, produces beating at $w_o - w_1$. If a mode at frequency

$$w_2 = w_o - w_1 \tag{2.35}$$

also exists then pump coupling with this will generate w_2. In principle can have various wave couplings but the simplest and the most important is the above. Parametric effects are particularly important in plasmas in view of the many possible modes, at both high and low frequency, which can be excited.

The relation (2.35) above expresses conservation of wave energy and its counterpart,

$$k_o = k_1 + k_2 \tag{2.36}$$

where k_i are the wave numbers, expresses the conservation of wave momentum.

The various coupling mechanisms of interest in laser produced plasmas are summarised below, where t denotes an electromagnetic transverse wave, l a langmuir plasma wave and s an ion acoustic wave, the latter two being longitudinal.

(i) t -> l + s parametric decay instability (PDI)

(ii) t -> t'+ s stimulated Brillouin scattering (SBS)

(iii) t -> t'+ l stimulated Raman scattering (SRS)

(iv) t -> l + l two-plasmon decay instability (TPDI)

Figure 2.6 shows regions where these & other processes occur on a density profile plot.

Of particular concern is the scattering processes in which one of the decay products is itself a transverse wave (SBS or SRS) which leaves the system and so transports energy out of the system. These will be dealt in subsequent sections. Here, we confine ourselves to the absorption mechanisms, PDI & TPDI.

The dispersion relations obeyed by the waves taking part are:-

$$t \qquad w_t^2 = w_p^2(z) + k_t^2 c^2 \qquad (2.37)$$

$$l \qquad w_l^2 = w_p^2(z) + k_l^2 v_l^2 \qquad (2.38)$$

$$s \qquad w_s = k_s c_s \qquad (2.39)$$

(where c is the speed of light, v_l is the electron's thermal velocity and c_s is the ion speed sound). These have been plotted in Figure 2.7 on a (w-k) plot.

Using Maxwell's equations, the growth rates and thresholds for the various processes above can be calculated. Essentially the threshold depends on the product of the damping rates of the two decay waves.

Another general property of such instabilities is that the energy is divided between the decay waves in proportion to their frequencies, a consequence of the Manley-Rowe relations [46].

Since wavenumbers only match, in general, around a certain value of z the effect is to make the system less unstable than the homogeneous equivalent. If the decay wave propagates in opposite directions it is possible to have an 'absolute instability', in which a perturbation grows in time at a fixed point in space. The growth rate is less than the growth rate in a homogeneous plasma and depends on the scale-length gradient, as well as the pump amplitude. If, however, damping is large and scale-length short there may be a 'convective instability'. In this case a perturbation localised in space does not grow in time.

(a) PARAMETRIC DECAY INSTABILITY (t -> l + s)

Since $w_t \sim w_l$ this process is confined to the region around the critical surface in order to satisfy the matching condition(2.35). Moreover since both decay products are electrostatic it can in priciple contribute to the absorption. On the other hand if the density profile is steepened then this implies that the relation(2.36) can only be satisfied over a very limited spatial region, so reducing the effectiveness of parametric decay as an absorption mechanism.

The theory of PDI has been dealt by Nishikawa [124-5] with a similar treatment by Hughes [86].

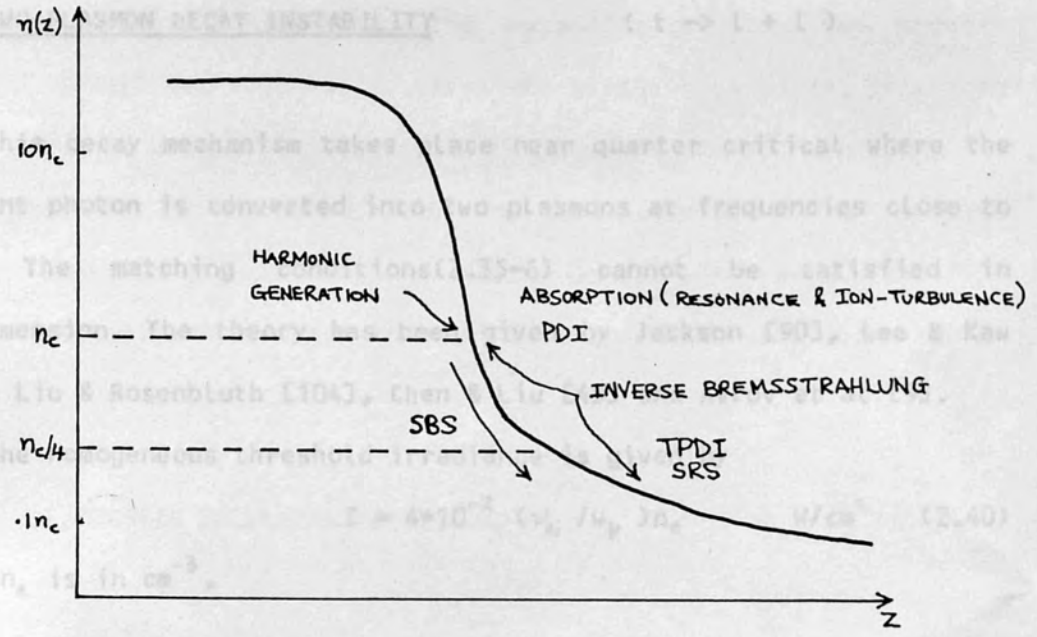

FIGURE 2.6 : Plasma density profile plot(schematic).

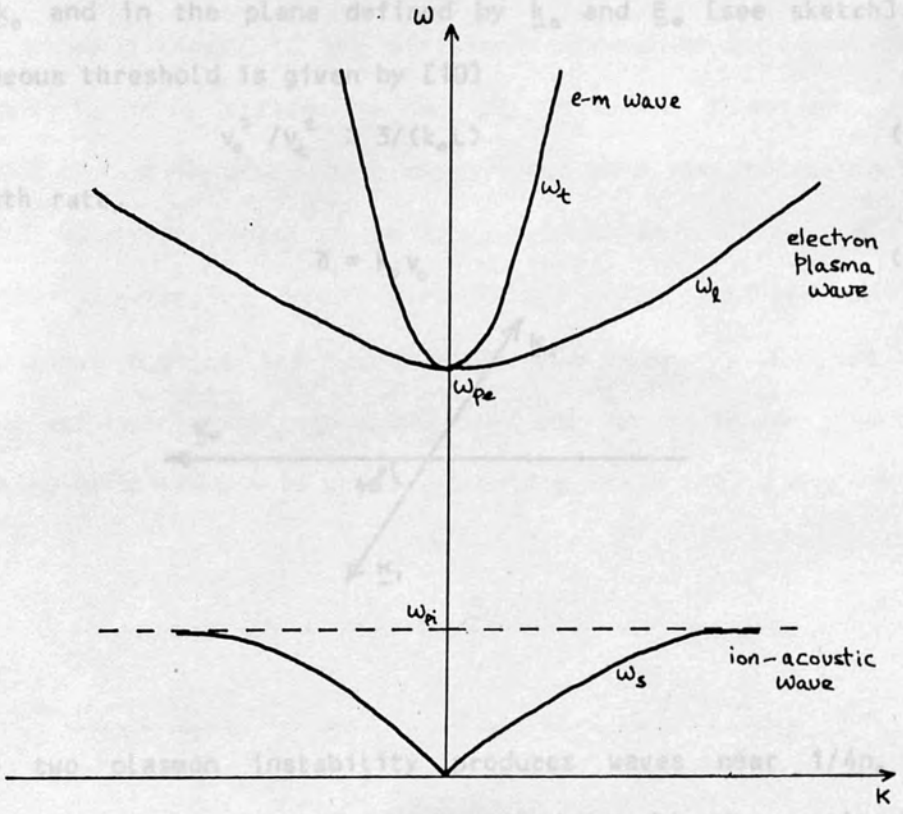

FIGURE 2.7 : Dispersion curves for waves inside a plasma. There is one transverse wave(frequency w_t) and two longitudinal waves(frequency w_ℓ and w_s).

(b) TWO-PLASMON DECAY INSTABILITY (t -> l + l)

This decay mechanism takes place near quarter critical where the incident photon is converted into two plasmons at frequencies close to $w_o/2$. The matching conditions(2.35-6) cannot be satisfied in one-dimension. The theory has been given by Jackson [90], Lee & Kaw [100], Liu & Rosenbluth [104], Chen & Liu [45] and Avrov et al [9].

The homogeneous threshold irradiance is given by

$$I = 4*10^{-2} (\nu_{ei}/w_p) n_e \quad W/cm^2 \quad (2.40)$$

where n_e is in cm^{-3}.

For k_1, $k_2 >> k_o$ [in eqn.(2.36)] the two plasma waves travel in almost opposite directions, at about 45° and -135° to the incident wave vector $\underline{k}_o$ and in the plane defined by $\underline{k}_o$ and $\underline{E}_o$ [see sketch]. The inhomgeneous threshold is given by [10]

$$v_o^2/v_t^2 > 3/(k_o L) \quad (2.41)$$

and growth rate,

$$\gamma = k_o v_o \quad (2.42)$$

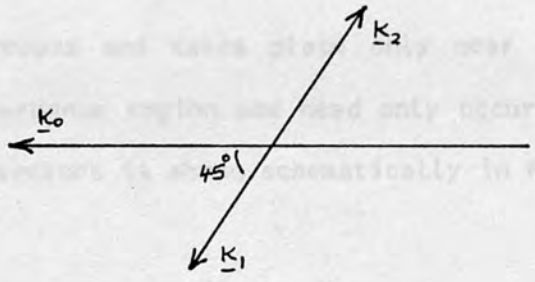

The two plasmon instability produces waves near $1/4n_c$ with consequent high electric field fluctuations in the region. The ponderomotive forces due to these fluctuations may result in a density cavity (caviton) around n_c which in turn may reduce the instability growth rate and eventually quench it. After the cavity has moved off

down the density gradient in the expanding plasma, the process restarts. Direct experimental observations of the decay waves generated by the TPDI in plasmas irradiated by intense CO_2 laser radiation, the modification of the density profile and subsequent quenching has been made by Baldis et al [10]. In most other experiments the TPD instability has been inferred from the 3w/2 radiation [33,88].

2.3 STIMULATED BRILLOUIN SCATTERING t -> t + s

The parametric conversion of a laser photon into another photon and ion-acoustic photon is known as stimulated Brillouin scattering (SBS). This may have serious consequences for laser plasma interactions since it poses a threat to the efficient absorption of light by the plasma due to much scattering in the backward direction. For a homogeneous plasma highest growth rates occur when the transverse decay wave is in opposite direction to the incident wave (recall $E_t \propto w_t$). Unlike the parametric decay instability which is inherently a two-dimensional process and takes place only near n_c, SBS can occur throughout the underdense region and need only occur in one dimension. The matching of k vectors is shown schematically in Fig. 2.8.

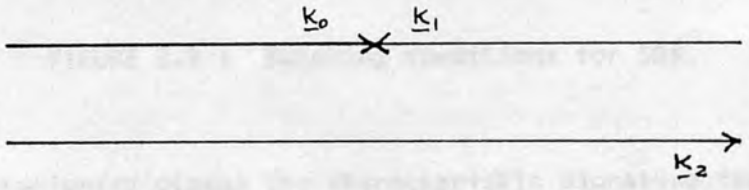

FIGURE 2.8 : Matching of k vectors.

Since $|\underline{k}_o| \sim |\underline{k}_1|$ it follows that $\underline{k}_1 \sim \underline{k}_o$ and thus $\underline{k}_2 \sim 2\underline{k}_o$. The matching conditions(2.35-6) have been represented in a w-k plot in Fig. 2.9. From the Figure it can be seen that matching is satisfied over a wide range of w and k. Since $w_t >> w_s$ very little of the incident energy is transferred to the ion wave. Thus SBS poses a threat to any scheme to heat and compress matter using laser radiation and consequently received much attention both theoretically [51,68-70,91,105-6] and experimentally [114,122,128-9].

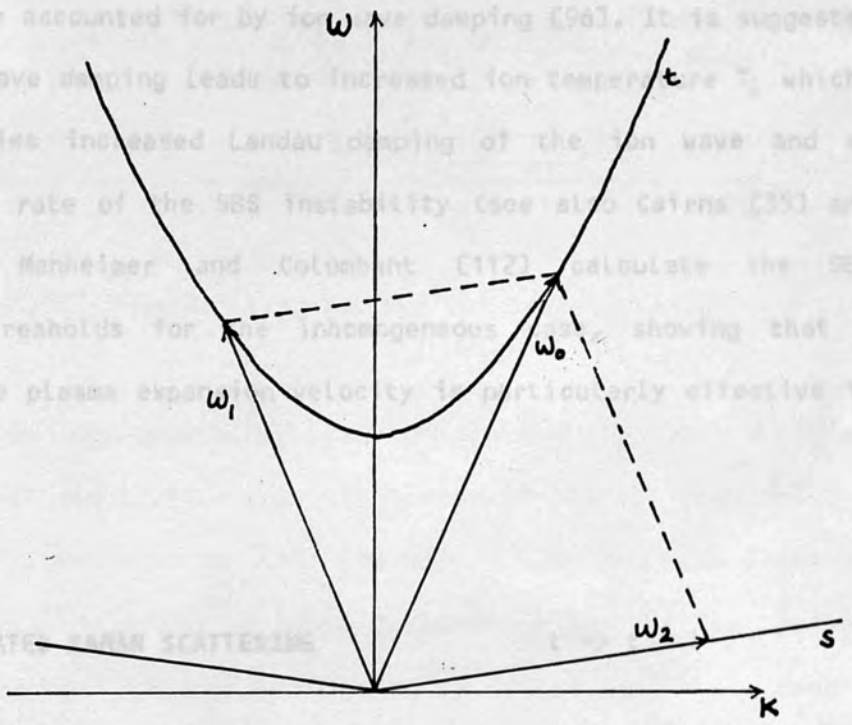

FIGURE 2.9 : Matching conditions for SBS.

For a stationary plasma the characteristic signature for SBS would be a red shift in the scattered radiation at w_o by the amount of the ion wave frequency. In laser plasma interactions, however, the plasma expands outwards giving rise to a blue Doppler shift and thus net shift can be either blue or red depending on flow being sub- or super-sonic.

In an inhomogeneous plasma it is the density gradient scale-length, L, which effectively determines the intensity threshold and an approximate field strength parameter for this case [91,106] is

$$(v_o / v_t)^2 = 4/(k_o L) \qquad (2.43)$$

where it is assumed that the temperature scale-length is much greater than L. Thus expect instability to be a serious problem for plasmas generated by long pulses, where scale-lengths are relatively larger.

However, measurements showing a less rapid increase in SBS than expected can be accounted for by ion wave damping [96]. It is suggested that the ion wave damping leads to increased ion temperature T_i which, in turn, implies increased Landau damping of the ion wave and so reduced growth rate of the SBS instability (see also Cairns [35] and Evans [64]). Manheimer and Colombant [112] calculate the SBS instability thresholds for the inhomogeneous case, showing that a gradient in the plasma expansion velocity is particularly effective in reducing SBS.

2.4 STIMULATED RAMAN SCATTERING $t \rightarrow t + l$

The parametric conversion of a laser photon into a lower energy photon and a plasmon is known as stimulated Raman scattering (SRS). Unlike SBS this is more localised since the frequency matching conditions(2.35-6) imply the incident wave frequency to be twice the plasma frequency (see Fig. 2.10). Thus SRS only occurs at electron desities not exceeding a quarter-critical ($1/4n_c$). Moreover, since the decay products have roughly equal frequencies, not more than $w_o/2$, then not more than 50% of the incident energy, from the Manley-Rowe relations, is scattered.

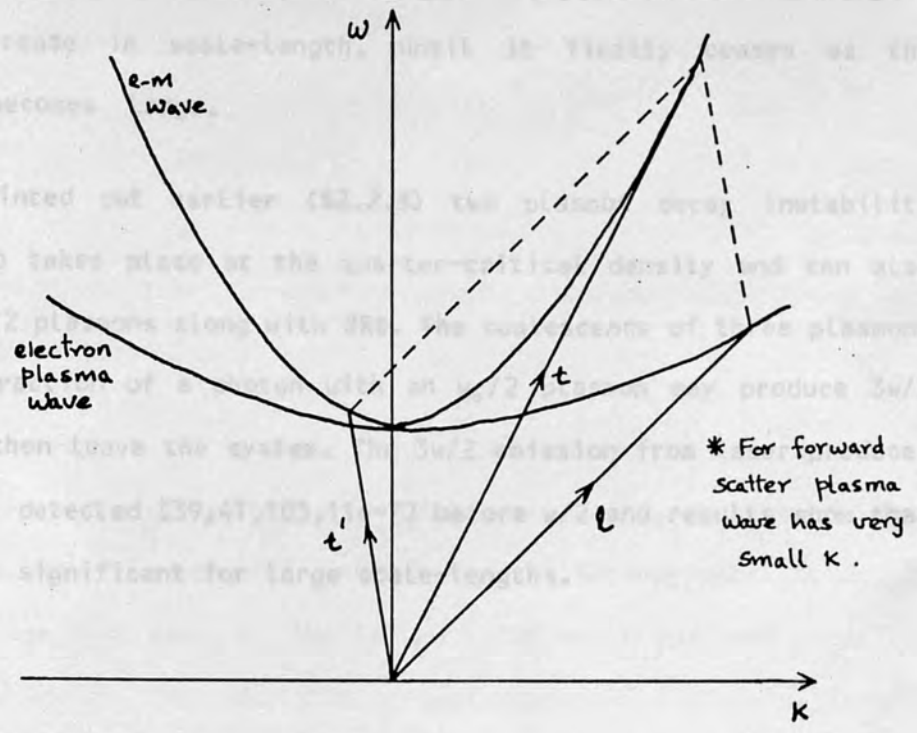

FIGURE 2.10 : Matching conditions for backscatter SRS.

SRS has maximum growth rate at $n=n_c/4$ and for $n<n_c/4$ strong damping gives reduced backscatter. The theory of SRS has been dealt by Liu et al [106], Drake et al [51] and others [80,84]. The threshold irradiance I_o at which SRS absolute backscatter instability develops is related through the quiver velocity (2.8) to the density scale-length L by the condition:

$$(v_o/c)^{3/2} \quad k_o L > 1 \qquad (2.44)$$

with growth rate

$$\gamma = k_o v_o/2 \qquad (2.45)$$

For sidescatter the threshold is lower than that in (2.44). The Raman instability should generate scattered light at a frequency close to $w_o/2$ and experiments at RAL [56] and Lebedev [93] have detected this. Forward SRS [92] may be important as it is not heavily damped so it could be driven to high amplitudes. Also it has a high phase velocity accelerating trapped particles to high velocities. This

eventually results in a ponderomotive plasma expulsion from $n_c/4$ region and a decrease in scale-length, until it finally ceases as the threshold becomes large.

As pointed out earlier (**§2.2.3**) two plasmon decay instability (TPDI) also takes place at the quarter-critical density and can also produce $w_o/2$ plasmons along with SRS. The coalescence of three plasmons or an interaction of a photon with an $w_o/2$ plasmon may produce 3w/2 which can then leave the system. The 3w/2 emission from laser produced plasmas was detected [39,41,103,116-7] before w/2 and results show that SRS is more significant for large scale-lengths.

2.5 SECOND & HIGHER HARMONIC GENERATION

2.5.1 INTRODUCTION

Nonlinear interactions of electromagnetic waves with a plasma described above can lead to anomalous absorption of laser radiation [135] and the deformation of the spectrum of the radiation reflected from the plasma. The latter has been studied in considerable detail. In particular, deformation of the spectra near the laser frequency [22,48,94,156] and second harmonic generation [42] were observed. The present section is devoted to a brief introduction, with subsequent sections dealing with particular theories on the subject, with a mention of higher harmonic generation in laser produced plasmas.

In a homogeneous isotropic plasma, the process

$$t + t \rightarrow t \qquad (2.46)$$

of coalescence of two transverse waves t with frequencies w' and w" and

wavevectors k' and k" into a transverse electromagnetic wave, t, with frequency, w, and wavevector, k, is forbidden [152] because matching conditions,

$$w' + w'' = w \qquad (2.47)$$

$$k' + k'' = k \qquad (2.48)$$

are not satisfied. These conditions can be interpreted as energy and momentum conservation laws.

The generation of a transverse electromagnetic wave with the doubled frequency w=2w ($w'=w''=w_o$) in such a plasma is possible only if at least one of the combining waves is a longitudinal oscillation, l, with a frequency w equal to the frequency of the transverse wave. The processes which are then possible, of coalescence of a plasmon, l, with either itself or a transverse wave, t, into another transverse wave:-

$$t + l \rightarrow t' \quad , \quad l + l \rightarrow t' \qquad (2.49)$$

In an inhomogeneous plasma, the wave vector still depends on the coordinates, so that the matching condition (2.48) is satisfied only for certain points in space. If there are no such points on the electron density profile, then the probability of the effect is exponentially small. The second harmonic energy flux is proportional to the energy fluxes of the interacting waves and is significant only when the intensity levels of the electron plasma oscillations and the transverse waves are high enough. Therefore, in order to generate the second harmonic effectively it is necessary, that a powerful longitudinal wave be formed and that there exists a point on the electron density profile where the matching conditions (2.47-8) are fulfilled for one of the processes in (2.49)

2.5.2 CAIRNS' THEORY

Briefly Cairns [37] theory assumes that plasma waves generated by resonant absorption at n_c couple to a series of side-bands via an ion-sound wave. The resultant broadening of the plasma wave spectrum being reflected in the second harmonic(2w) emission. Also if the ion sound wave propagates outwards, then for suitable parameters, a large number of side-bands on the long-frequency side are excited and consequently reflected in the 2w emission. The theoretical model is briefly discussed below.

The second harmonic can be generated as a result of coalescence of a photon and a plasmon,

$$t + l \rightarrow t' \qquad (2.50)$$

The dominant mechanism of plasma wave generation, near the critical surface (n_c), is resonant absorption as steepening of the density profile occurs (**§2.2.2**) during laser plasma interactions, making the decay instability ineffective. In a stationary plasma one expects plasmons to have the same frequency as that of incident photons to satisfy matching condition(2.35). However, heat flux instabilities and other mechanisms may generate ion sound waves along with plasmons with a different frequency near n_c.

The theory considers a 1-D model where the density varies as:-

$$n_o(x) + \hat{n}_i(x,t) \qquad (2.51)$$

where n_o is the average density which varies linearly outwards

$$n_o(x) = n_c(1 - x/L) \qquad (2.52)$$

where n_c is the density at the critical surface and L is the scale-length.

The fluctuating density $\tilde{n}_i$ is the result of an ion sound wave and varies according to

$$\tilde{n}_i = n_i(x)e^{i\Omega t} + n_i^*(x)e^{-i\Omega t} \qquad (2.53)$$

where n_i^* is the complex conjugate and Ω is the ion sound frequency. The plasma velocity $\tilde{v}_i$ varies in a similar manner.

An oscillating high-frequency field $E_o e^{i\omega t}$ along the density gradient, produced by an obliquely incident component of the laser radiation, drives the plasma waves near n_c - The linearised equations for the electron response can then be written:-

$$dn/dt + d/dx[(n_o+\tilde{n}_i)v] = 0 \qquad (2.54)$$

$$dv/dt + \tilde{v}_i\, dv/dx = e/m(E+E_o e^{i\omega t}) - 3T_e\, dn/dx \qquad (2.55)$$

$$dE/dx = ne/\varepsilon_o \qquad (2.56)$$

where n and v represent electron density and velocity respectively.

Assuming $$n = \sum_\ell n_\ell e^{i\omega t + i\ell\Omega t} \qquad (2.57)$$

i.e. sum over all electron, langmuir and ion-acoustic oscillations.

Similarly for v and E one obtains a similar set of equations.

Using the continuity equations relating $\tilde{n}_i$ and $\tilde{v}_i$ and taking the Debye length as the shortest characteristic length for variation of E_o, then can neglect coupling terms involving $\tilde{v}_i$ as small in comparison to those involving $\tilde{n}_i$. With change of variables y=x/L gives

$$\beta\, d^2E/dy + (y-2l\Omega/w)E_\ell = \xi e^{-iky} E_{\ell-1} + \xi e^{iky} E_{\ell+1} + \text{driving terms} \qquad (2.58)$$

where $$= 3v_e^2/(w^2L^2) \qquad (2.59)$$

and K, the wavenumber of ion sound wave is in units of 1/L. If the electron temperature is taken in keV and L in units of λ_o(incident wavelength) then

$$\beta \approx 1.5*10^{-4}\, T/L^2 \qquad (2.60)$$

The set of equations(2.58) describes the generation of, and

coupling amongst, a set of plasma waves of frequencies differing from the laser frequency by multiples of Ω, the ion sound frequency.

Numerical results can be obtained for(2.58) using the boundary conditions that

(i) E decays for $n>n_c$ and

(ii) behaves like outward propagating wave for $n<n_c$

Obviously a solution will be dependent on parmeters β, ε, Ω/w and K where the latter two are related through the dispersion relation. Numerical results indicate solutions sensitive to changes in K, controlling the effectiveness with which energy is transferred from driven modes into low frequencies reaching a maximum for K=35. Near the critical surface the wavenumber of the plasma is [113] $2/3\pi\beta^{-1/3}$ (in units of 1/L) which is 39.5, i.e. expect maximum transfer for similar value of K, which was found to be the case! Since $k \propto \beta^{-1/3}$ at critical surface expect that the optimum value of K to vary similarly.

If β and K are fixed, then the width of plasma wave spectrum is found to increase with permittivity ε. However, as the mode coupling varies as $\varepsilon\beta^{-1/3}$ one expects similar spectral shape for constant $\varepsilon\beta^{-1/3}$ but not identical because driving terms scale differently.

The spectral broadening and shift in second harmonic emmision is thus a consequence of the corresponding broadening and shift in the spectrum of plasma waves excited near the critical surface. The wavelength shift in the second harmonic spectrum is given by

$$d\lambda/\lambda_o = 1/4*\Omega/w_o \qquad (2.61)$$

where λ_o is the laser wavelength and Ω is the frequency shift. If the effects of plasma motion are neglected, the ion sound frequency is

$$\Omega = (Z/A)^{1/2} (m_e/m_i) v_e k_{is} = (Z/A)^{1/2} (m_e/m_i)^{1/2} K(\beta/3)^{1/2} w_o \qquad (2.62)$$

where K being the ion-sound wavenumber in unit of 1/L. As the most important value of K is $2/3\pi\beta^{-1/3}$, as argued above, then

$$d\lambda = 47\lambda_o \beta^{1/6} \quad \text{Å} \tag{2.63}$$

$$= 47\lambda_o [1.5*10^{-4} T/L\ ]^{1/6} \quad \text{Å} \tag{2.64}$$

where A/Z~2, T in keV and L in units of λ_o.

For a moving plasma $d\lambda$ may change and it would be possible for adjacent side-bands to be a few Å apart, the total 2w spectrum being built up from ten or more such bands. This would give rise to extra structure in the 2w spectrum.

The consequences of these results are discussed later(**§4**) for neodymium and CO_2 laser produced plasmas.

2.5.3 THEORY OF PARAMETRIC PLASMA RESONANCE

INTRODUCTION :

Many authors have concerned themselves with the theory of parametric plasma resonance leading to the excitation of the longitudinal perturbation. Amongst the first was that by DuBois and Goldman [52] based on a cumbersome Feynmann diagram technique of quantum statistics and they later adopted a kinetic approach [53], Lee and Su [102] in their approach, used the hydrodynamic equations of a collisionless charged fluid. Nishikawa [125] allowed for collisions of charged particles, a fundamental characteristic of parametric resonance in weak fields. A detailed theory of the parametric instability of a fully ionised plasma with regards to the excitation of longitudinal perturbations in a weak field was built up in the paper of Andreev, Kyrii and Silin [5]. Here the paper by Silin [146] is reviewed.

SILINS' THEORY :

The second harmonic can arise as a result of another coalescence process, that of two electron langmuir waves,

$$l + l \rightarrow t \qquad (2.65)$$

One source of the generation of intense electron langmuir oscillations is the parametric buildup of plasma oscillations in the presence of a powerful electromagnetic wave [5,135]. The mechanism of parametric buildup consists, for example, in decay of an incident electromagnetic wave into electron plasma oscillations and ion-sound oscillation (a non-linear transformation). According to the results of Pustovalov and Silin [135] the longitudinal wave amplitude is at a maximum along the electric field intensity vector of the radiation incident on the plasma. Thus expect the second harmonic radiation due to parametric resonance to be directed perpendicular to the incident light beam. The theory presented by Silin [146] takes the situation where the frequency of the external field is close to the frequency of plasmons,

$$|w_o - w_p| \ll w_p \qquad (2.66)$$

noting that relatively long-wave oscillations grow when the external-field frequency approaches w_p . Also assumed is that the wavelength of this oscillation is much greater than the Debye wavelength of electrons.

In common with other theories of parametric resonance in a plasma, the spectrum of the longitudinal oscillations and the corresponding instability condition for a fully ionised plasma are determined by the conditions that a solution exists for the set of equations for the electron and ion charge densities n_e and n_i. For a weak field, $v_t > v_o$ and appropriate approximations lead to the dispersion equation of

plasmons and consequently an expression for the dielectric constant

$$\varepsilon = 1 - (w_p/w_o)^2 (1+i\nu/w_o) \qquad (2.67)$$

The dispersion relation predicts the existence of an aperiodic instability at $w_o < w_p$ just as the hydrodynamic theory of parametric resonance [125] does, though the relation so obtained includes the effect of thermal motion of ions.

The consequences of the dispersion equation for parametric plasma instability are:-

(i) an instability is produced aginst the buildup of oscillations with frequencies equal to zero and w_o for which the minimal threshold intensity of the external field is determined only by the frequency of electron-ion collisions - oscillations at w_o can be distinguished from the external field by their phase shifts.

(ii) an instability connected with growth of almost periodic oscillations is possible when $w_o > w_p$. Here, depending on the collision frequency and on the frequency deviation, two possibilties arise:-

(a) under the decay conditions ($\delta w = w_s$) the oscillations with frequencies w and $w-w_o$ increase with $w=w_o$, and

(b) oscillations with frequencies $w+w_o$ and $w-w_o$ are possible with approximately equal amplitudes, whilst w can greatly exceed the ion-acoustic frequency even at the threshold.

The oscillation buildup in a plasma, investigated in [5,146] can lead to the appearance of a turbulent state, and consequently to a nonlinear absorption (and reflection) of the external field; in the case of laser produced plasmas, this can lead to parametric absorption and harmonic emission.

The above theory of parametric resonance offers a possibility of determining the dependence of shift of the intensity maximum of the second harmonic line on such parameters as the electron temperature, T_e, ion content and radiation flux, I_o [136]. A comparison of the experimental shift of 2w with the theoretical formula makes it possible to determine the temperature T_e for a given laser-radiation flux, I_o. The red shift δw is determined by the expression by Krokhin [95] [cf. Silin [146], eqn.(9.9)].

$$\delta w = \sqrt{3} w_{pi} [v_t^2 / c^2 + (v_o^2 w_o / 4c^2 \Delta w_o(x))] \qquad (2.68)$$

where w_{pi} is the ion plasma frequency, v_t is the electron thermal velocity, c is the speed of light, v_o is the amplitude of the velocity of the electron oscillation in the incident electromagnetic field and $\Delta w_o(x)$ is the detuning

$$\Delta w_o = w_o - w_p(x) \simeq w_o(x/2L) \qquad (2.69)$$

(where L is the characteristic dimension of the plasma inhomogeneity) is larger than the long-wave ion-sound oscillations.

Since the structure of the electromagnetic wave near the critical surface is described by an Airy function [76] (**§2.2.2**), the characteristic dimension in formula(2.69) can be chosen to be $(c^2 L / w_o^2)^{1/3}$, which is of the order of the distance between the first maximum of this function and the critical point.

For a laser produced plasma, formula(2.68) can be represented by the relation [95]

$$\delta\lambda = \delta w / 4w_o = (Z/A)^{1/2} \lambda_o [20T_e + 1.3*10^{-14} (I_o \lambda_o^2)(L/\lambda_o)^{2/3}]^{1/2}$$

taking $A/Z \sim 2$

$$\simeq [10T_e + 6.3*10^{-15} I_o \lambda_o^2 (L/\lambda_o)^{2/3}]^{1/2} \qquad (2.70)$$

relating the red shift $\delta\lambda$, measured in angstroms, and the electron temperature T_e (in keV), the energy flux of the incident light wave

I_o(in Wcm^{-2}) and the characteristic dimension, L, of the inhomogeneity.

The above formula(2.70) allows the electron temperature T_e to be determined in the range of irradiances, I_o, where the first term is not small in comparison with the second. At larger fluxes, when the second term predominates, the shift $\delta\lambda$ ceases to depend on the plasma temperature.

Further treatment of the above candidate theories, for 2w, is left to the discussion chapter (§4), where tests will reveal the best theory to fit the experimental results.

2.5.4 OVERVIEW OF 2W GENERATION

Second harmonic generation in laser produced plasmas has received much theoretical treatment [3,4,8,20,23,27-8,36,50,57-60,148,153-4] and experimental attention [10-1,14,26,34,38,42,54,83,87,101,108,118, 141,144].

The source of plasmons in the combination(2.49) leading to second harmonic is either via a resonance or a parametric process though the former has received greater attention and analysis. The effect of p- or s- polarised light [3,8,14,50,108,144,154], density scale lengths [8,38,60], angles of incidence [3,36,108,144,153], ponderomotive forces [3,148], density profile steepening [3,8,36,38], temperature [3,8,57,59,153], magnetic fields [28,60], etc have all been discussed. A comprehensive review of second harmonic generation in laser plasmas is given by Basov et al [20] and references therein. Some important aspects, from the above mentioned papers, have been sifted and outlined below.

A 1½D code [28] shows that a strong magnetic field near the critical surface can lead to significant absorption and thus second harmonic, whilst a 2D code [38] indicates that harmonics offer means of measuring upper density shelf structure and its dynamics. This has also been demonstrated by Auer [8]. The efficiency of conversion to second harmonic has been determined by several authors [50,60,144,153] and range from 0.001 to 10^{-6} of incident intensity dependent on the polarisation of the light, plasma temperature and plasma density structure. For a density profile steepened near the critical surface the second harmonic emission, resulting from resonance absorption, may have oscillations as a function of angle although the overall shape of the envelope is roughly the same as the absorption curve [36]. A density profile with a caviton can lead to large enhancement of harmonic emission [3] because of the formation of electrostatic resonant structures —this effect becomes important when the density profile is deformed by the ponderomotive force.

Finally, from theory, it is expected that the amplitude of the second harmonic radiation be proportional to the square of the amplitude of the fundamental. This arises because the intensity for a given radiation field, E is given by

$$I = (c/8\pi)\varepsilon E^2 \tag{2.71}$$

where ε is the dielectric constant of the medium, so it is obvious that

$$I_{2\omega} \propto |E_o|^4 \tag{2.72}$$

or

$$I_{2\omega} \propto I_o^2 \tag{2.73}$$

Thus expect that the intensity of the second harmonic [144] scales with the square of the incident intensity.

2.5.5 HIGHER HARMONIC GENERATION

Higher integer harmonic generation (nw) can result from further coalescence of plasmons or plasmons with scattered or incident photons.

$$l + l + l \rightarrow t' \tag{2.74}$$

$$l + l + t \rightarrow t' \quad \text{etc..} \tag{2.75}$$

Once again the matching conditions must be satisfied, viz. conservation of energy and momentum. Higher harmonic generation is thus likely to occur close to the critical region, where fudamental and local plasma frequencies are approximately equal. observation of higher integer harmonics(nw) are expected to reveal information on density gradients and electric fields prevalent in this region of the plasma.

For obvious reasons the threshold intensity increases with increasing n and the intensity of nw should be related to the incident intensity I_o by the nth power,

$$I_{n\omega} \propto I_o^n \tag{2.76}$$

Finally expect the line profile of nw to be characteristic of the ion wave spectrum.

Higher harmonics have been observed for CO_2 [12,34,65] and Nd-laser produced plasmas [48].

2.6 HALF HARMONIC GENERATION

At the quarter-critical surface two processes — stimulated Raman scattering, SRS(**§2.4**), and the two-plasmon decay(TPD) instability(**§2.2.3**)- can produce $w_o/2$ plasmons. Photons at $w_o/2$ can

then be generated either by Stokes Raman scattering of the incident pump wave off these plasmons or by linear mode conversion. Bobin et al [26] first observed light at $w_o/2$ and recently has been detected at Lebedev [93] and Rutherford by RHC members [56,117].

From the thresholds of SRS and TPD and recent simulations [25,98] combined with the growth rates indicate that TPD may be more significant than SRS for $w_o/2$ generation. Observation of $w_o/2$ provides a measure of the plasma frequency and hence can be used to estimate the electron temperature at the quarter-critical.

A $3w_o/2$ photon can result from either an interaction of $w_o/2$ plasmon with an incident, reflected or scattered w_o photon or a coalescence of three $w_o/2$ plasmons. This has been observed experimentally [39,41,103,116] and dealt with theoretically [9,40]. For short pulses and small scale-lengths, TPD is the dominant mechanism for $w_o/2$ plasmons whilst for long pulses and large scale-lengths SRS competes strongly. Experiments have shown a spectrum consisting of two peaks symmetrically displaced to the red and blue of the $3w_o/2$ frequency. According to Barr's theory [40] the spacing between the peaks is related to the electron temperature T_e at the quarter-critical through

$$\Delta\lambda(\text{Å}) = 48.6\ T_e \quad (\text{keV}) \tag{2.77}$$

Carter and Wooding [39] estimate the plasma density scale-length from the relative intensities of the blue and red shifted satellites of 3w/2. Lin [103], on the other hand, argues that these shifts can be explained by an unstable filamentation model, where the frequency shift of 3w/2 emission is mainly due to the Doppler shift of the density contours, inside the filament, during their formation and collapse.

The five-halves harmonic, 5w/2 has been shown to occur only in the presence of a $2w_o$ probe beam which combines with a $w_o/2$ plasmon [17]. Similarly for higher half-integer harmonics.

2.7 BACKSCATTER & REFLECTIVITY

Several processes result in reflection particularly stimulated Brillouin scattering (§2.3), which has the most drastic affect on backscatter from laser produced plasmas. The effect of density profile modification with or without fluctuations, the light polarisation, angle of target, target material and irradiance on reflectivity have been investigated experimentally [1,2,6,7,55,78,89,107,109,137-9,150] and theoretically [1,2,16,19,63,112,145,150]. A brief review of some of the experimental and theoretical work is presented below.

For irradiance $I_o<10^{11}$ Wcm^{-2}, absorption takes place primarily through high collision rate of the electron gas [2] which can be inferred from the blue shift of the reflected light [150]. A few experiments [6,78] have used an integrating sphere photometer to accurately determine the absorption. Anthes et al [6] observed the absorption to decrease linearly from 0.9 to 0.8 whilst the intensity increased from 10^{13} Wcm^{-2} to 10^{14} Wcm^{-2} and was independent of the target material, Z. However, Arad et al [7] measured the absorption to be Z-dependent with stimulated scatter independent of Z over the intensity range 10^{13}-10^{16} Wcm^{-2} and Jackel et al [89] indicated reduced reflectivity, from high Z targets, for specularly reflected light. At higher irradiances absorption was limited by increased stimulated scatter rather than decreased efficiency [7].

The reflectance for normal incidence is seen to be greater than 60% having a minimum for angle of incidence, $\theta \sim 20^{\circ}-30^{\circ}$ for p-polarised light [78]. On the other hand, Maaswinkel [107,109] observed 80% absorption for normal incidence with little dependence on I_o, wavelength or pulse. Again the characteristic behaviour of resonance absorption was observed for p-polarised light and angled illumination. Also increased backscatter resulted as a consequence of a weak prepulse just before the main laser pulse [138].

Finally, Ripin [139] measured the reflectivities to lie in the range of 20-50% remaining approximately constant for illuminations at $\theta=0^{\circ}$ to 60°, implying the existence of steep density gradients near n_c or absorption of light in underdense region of plasma.

Due to the varied nature of the above results, interest in backscatter measurements continues; to determine responsible parameters. The optimisation of these parameters for maximum absorption is then crucial for any inertial fusion scheme.

One such parameter concerns nonpropagating density ripples, which are produced in a flowing laser produced plasma by the ponderomotive force of incident and reflected light from the critical surface(These ripples being an equilibrium feature of flow rather than being related to any instabilities). For certain conditions these can significantly increase specular reflection and thereby reduce the amount of light reaching the critical surface [145]. Thus a need to minimise this effect to reduce reflectivity losses becomes paramount.

2.8 PLASMA TEMPERATURE

Amongst the plasma parameters required to fully understand the second harmonic are the plasma temperature, density structure and scale-length along with their spatial distributions and temporal behaviour. However, here we shall only characterise the plasma temperature leaving the latter parts to be discussed together with the results.

The variation of the hot-electron temperature with scaling parameter $I\lambda^2$ was obtained from a modified hydrodynamic code, LASNEX [81,119] which solves the single-fluid, two-temperature Lagrangian hydrodynamic equations in two-dimensional axi-symmetric geometry.

The modifications include x-ray and hot-electron generation and multigroup flux-limited diffusion transport. Laser light is taken to be absorbed by inverse bremsstrahlung up to the critical surface. At the critical surface a selectable fraction of the remaining laser energy is deposited to simulate resonant absorption. Other additions to code include the ponderomotive force(2.34) and the hot-electron temperature T_h is taken as [73]

$$T_h = \alpha (I\lambda^2)^p T_e^q \qquad (2.78)$$

where α is chosen to agree with numerical plasma simulations and experiments. T_e is the background electron temperature at the critical surface. The powers p and q lie in the range 0.25-0.33 and 0.33-0.50 respectively, as found from plasma simulation [73]. This work also shows that the generation of such fast electrons to be dependent on the profile modification due to ponderomotive forces, neglecting thermal flux limitations. In the simulated results [77], presented below, only the absorbed laser intensity was variable, all other potential

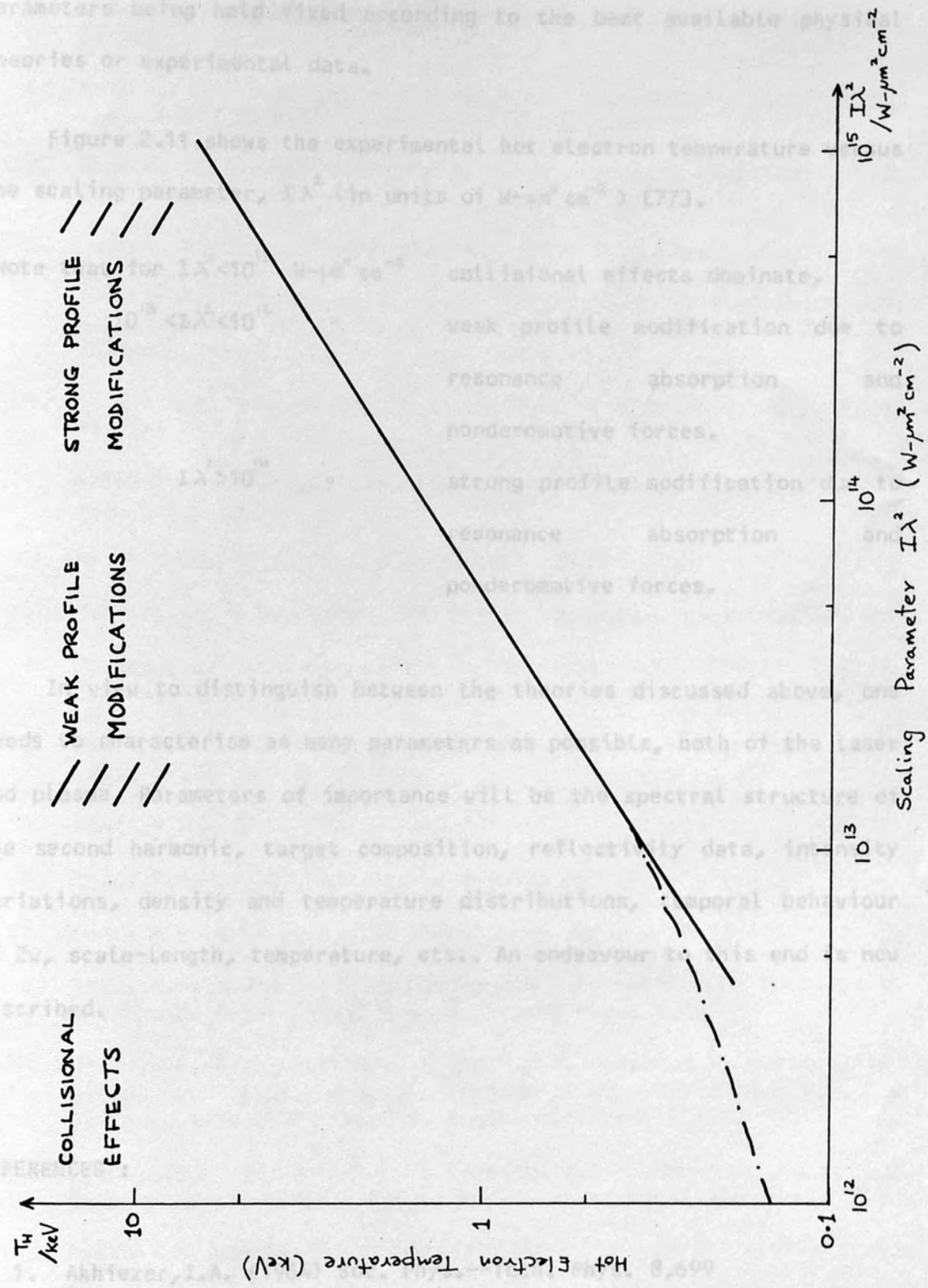

FIGURE 2.11 : Variation of hot electron temperature with $I\lambda^2$

parameters being held fixed according to the best available physical theories or experimental data.

Figure 2.11 shows the experimental hot electron temperature versus the scaling parameter, $I\lambda^2$ (in units of $W\text{-}\mu m^2\,cm^{-2}$) [77].

Note that for $I\lambda^2<10^{13}$ $W\text{-}\mu m^2\,cm^{-2}$ collisional effects dominate,

$10^{13}<I\lambda^2<10^{14}$ " weak profile modification due to resonance absorption and ponderomotive forces.

$I\lambda^2>10^{14}$ " strong profile modification due to resonance absorption and ponderomotive forces.

In view to distinguish between the theories discussed above, one needs to characterise as many parameters as possible, both of the laser and plasma. Parameters of importance will be the spectral structure of the second harmonic, target composition, reflectivity data, intensity variations, density and temperature distributions, temporal behaviour of 2w, scale-length, temperature, etc.. An endeavour to this end is now described.

REFERENCES :

1. Akhiezer,I.A. (1964) Sov. Phys.--Tech. Phys. **8**,699
2. Amman,F. Banfi,G.P. Gobbi,P.G. Morosi,S. & Reali,G.C. (1980) Plasma Phys. **22**,453
3. Andreev,N.E. (1981) Phys. Fluids **24**,1492
4. Andreev,N.E. Artsimovich,V.L. Kasyanov,Yu.S. Krobin,V.V. Silin,V.P. & Stenchikov,G.L. (1980) Sov. Phys.--JETP Lett. **31**,603

5. Andreev,N.E. Kiryi,A.Yu. & Silin,V.P. (1970) Sov. Phys.--JETP **30**,559

6. Anthes,J.P. Palmer,M.A. Gusinow,M.A. & Matzen,M.K. (1979) Appl. Phys. Lett. **34**,841

7. Arad,B. Eliezer,S. Gazit,Y. Jackel,S. Karmi,Y. Loebenstein,H.M. & Zigler,A. (1980) Appl. Phys. Lett. **37**,774

8. Auer,G. Sauer,K. & Baumgartel,K. (1979) Phys. Rev. Lett. **42**,1744

9. Avrov,A.I. Bychenkov,V.Yu. Krokhin,O.N. Pustovalov,V.V. Rupasov,A.A. Silin,V.P. Sklizkov,G.V. Tikhonchuk,V.T. & Shikanov,A.S. (1977) Sov. Phys.--JETP **45**,507

10. Baldis,H.A. Samson,J.C. & Corkum,P.B. (1978) Phys. Rev. Lett. **41**,1719

11. Baldis,H.A. Pepin,H. Johnston,T.W. & Parbhakar,K.J. (1975) Phys. Rev. Lett. **35**,37

12. Baldis,H.A. (1975) Appl. Phys. Lett. **27**,291

13. Balmer,J.E. & Donaldson,T.P. (1977) Phys. Rev. Lett. **39**,1084

14. Balmer,J.E. Schwarzenbach,A.P. & Weber,H.P. (1982) Optics. Commun. **42**,121

15. Banfi,G.P. Gobbi,P.G. Morosi,S. & Reali,G.C. (1980) Appl. Phys. Lett. **37**,23

16. Banfi,G.P. (1981) Phys. Lett. **83A**,167

17. Basov,N.G. (1980) Phys. Lett. **77A**,163

18. Basov,N.G. & Krokhin,O.N. (1964) Sov. Phys. JETP **19**,123

19. Basov,N.G. Boiko,V.A. Danilychev,V.A. Zvorykin,V.D. Kholin,I.V. & Chugunov,A.Yu. (1979) Sov. J. Plasma Phys. **5**,407

20. Basov,N.G. Bychenkov,V.Yu. Krokhin,O.N. Osipov,M.V. Rupasov,A.A. Silin,V.P. Sklizkov,G.V. Starodub,A.N. Tikhonchuk,V.T. & Shikanov,A.S. (1979) Sov. J. Quant. Electron. **9**,1081

21. Basov,N.G. Kriukov,P.G. Zakharov,S.D. Senatsky,Yu.V. & Tchekalin,S.V. (1968) IEEE J. Quant. Electron. **4**,864

22. Belland,P. DeMichelis,C. Mattioli,M. & Papoular,R. (1971) Appl. Phys. Lett. **18**,542

23. Bezzerides,B. Jones,R.D. & Forslund,D.W. (1982) Phys. Rev. Lett. **49**,202

24. Bezzerides,B. DuBois,D.F. Forslund,D.W. & Lindman,E.L. (1977) Phys. Rev. Lett. **38**,495

25. Biskamp,D. & Welter,H. (1975) Phys. Rev. Lett. **34**,312

26. Bobin,J.L. Decroisette,M. Meyer,B. & Vitel,Y. (1973) Phys. Rev. Lett. **30**,594

27. Bobin (1977) in " Plasma Physics - Nonlinear theory & Experiment " ed. Wilhelmsson,H., Plenum Press (USA) p.102-21

28. Boyd,T.J.M. (1979) J.de. Physique **40**, C7-551

29. Brysk,H. (1975) Plasma Phys. **17**,473

30. Brysk,H. (1975) J. Phys. **A8**,1260

31. Budden (1966) ' Radio Propagation in the Ionosphere ' Cambridge

32. Bunkin,F.V. & Fedorov,M.V. (1966) Sov. Phys.--JETP **22**,844

33. Burnett,N.H. Baldis,H.A. Enright,G.D. Richardson,M.C. & Corkum,P.B. (1977) J. Appl. Phys. **48**,3727

34. Burnett,N.H. Baldis,H.A. Richardson,M.C. & Enright,G.D.(1977) Appl. Phys. Lett. **31**,172

35. Cairns,R.A.(1982) Plasma Phys. **24**,109

36. Cairns,R.A.(1981) Plasma Phys. **23**,705

37. Cairns,R.A.(1979) J. Plasma Phys. **22**,149

38. Carman,R.L. Forslund,D.W. & Kindel,J.M. (1981) Phys. Rev. Lett. **46**,29

39. Carter,P.D. & Wooding,E.R. (1982) Phys. Lett. **87A**,407

40. Carter,P.D. Sim,S.M.L. Barr,P. & Evans,R.G. (1980) Optics Commun. **44**,1407

41. Carter,P.D. Sim,S.M.L. & Wooding,E.R. (1980) Optics Commun. **32**,443

42. Caruso,A. DeAngelis,A. Gatti,G. Gratton,R. & Martellucci,S. (1970) Phys. Lett. **33A**,29

43. Catto,P.J. & More,R.M. (1977) Phys. Fluids **20**,704

44. Catto,P.J. & Speziale (1977) Phys. Fluids **20**,167

45. Chen,H.H. & Liu,C.S. (1977) Phys. Rev. Lett. **39**,881

46. Davidson (1972) " Methods in Nonlinear Plasma Physics ", Academic Press

47. Dawson,J. Kaw,P. & Green,B. (1968) Phys. Fluids **12**,875

48. Decroisette,M. Piar,G. & Floux,F. (1970) Phys. Lett. **32A**,249

49. Denisov,N.G. (1957) Sov. Phys.--JETP **4**,544

50. Dragila,R. (1982) Phys. Rev. **25A**,1127

51. Drake,J.F. Kaw,P.K. Lee,Y.C. Schmidt,G. Liu,C.S. & Rosenbluth,M.N. (1975) Phys. Fluids **17**,778

52. DuBois,D.F. & Goldman,M.V. (1965) Phys. Rev. Lett. **14**,544

53. DuBois,D.F. & Goldman,M.V. (1967) Phys. Rev. **164**,207

54. Eidmann,K. & Sigel,R. (1975) Phys. Rev. Lett. **34**,799

55. Eidmann,K. & Sigel,R. (1973) Paper presented at the 3rd Workshop on 'Laser interactions & related phenomena' at Rensselaer Polytechnic Institute, Troy, N.Y. Aug. 13-17.

56. Elazar,J. Toner,W.T. & Wooding,E.R. (1981) Plasma Phys. **23**,813

57. Erokhin,N.S. Moiseev,S.S. & Mukhin,V.V. (1974) Nuc. Fusion **14**,333

58. Erokhin,N.S. & Moiseev,S.S. (1970) Sov. Phys.--Tech. Phys. **15**,885

59. Erokhin,N.S. Zakharov,V.E. & Moiseev,S.S. (1969) Sov. Phys.--JETP **29**,101

60. Erokhin,N.S. Moiseev,S.S. & Shuklin,A.P. (1980) Sov. Phys.--JETP **52**,1088

61. Estabrook,K.G. Valeo,E.J. & Kruer,W.L. (1975) Phys. Fluids **18**,1151

62. Estabrook,K.G. & Kruer,W.L. (1978) Phys.Rev. Lett. **40**,42

63. Estabrook,K.G. Harte,J. Campbell,E.M. Ze,F. Phillion,D.W. Rosen,M.D. & Larsen,J.T. (1981) Phys. Rev. Lett. **46**,724

64. Evans,R.G. (1981) Plasma Phys. **23**,99

65. Fabre (1976) in " Proc. IAEA 6th Int. Conf. on Plasma Physics and Controlled Nuclear Fusion Research " Berchtesgaden, West Germany. -Paper IAEA-CN-35/G 3-4

66. Faehl,R.J. & Roderick,N.F. (1977) Phys. Fluids **20**,1279

67. Faehl,R.J. & Roderick,N.F. (1978) Phys. Fluids **21**,793

68. Forslund,D.W. Kindel,J.M. & Lindman,E.L. (1973) Phys. Rev. Lett. **30**,739

69. Forslund,D.W. Kindel,J.M. & Lindman,E.L. (1975) Phys. Fluids **18**,1002

70. Forslund,D.W. Kindel,J.M. & Lindman,E.L. (1975) Phys. Fluids **18**,1017

71. Forslund,D.W. Kindel,J.M. Lee,K. Lindman,E.L. & Morse,R.L. (1975) Phys. Rev. **11A**,679

72. Forslund,D.W. Kindel,J.M. Lee,K. & Lindman,E.L. (1976) Phys.

Rev. Lett. **36**,35

73. Forslund,D.W. Kindel,J.M. & Lee,K. (1977) Phys. Rev. Lett. **39**,284

74. Freidberg,J.P. Mitchell,R.W. Morse,R.L. & Rudsinski,L.I. (1972) Phys. Rev. Lett. **28**,795

75. Galeev,A.A. (1974) Sov. Phys.--JETP **38**,482

76. Ginzburg,V.L. (1970) " The Propagation of Electromagnetic Waves in Plasmas " 2nd edition Oxford, Pergammon

77. Gitomer,S.J. & Henderson,D.B. (1979) Phys. Fluids **22**,364

78. Godwin,R.P. Sachsenmaier,R. & Sigel,R. (1977) Phys. Rev. Lett. **39**,1198

79. Golant,V.E. & Piliya,A.D. (1972) Sov. Phys.--USPEKHI **14**,413

80. Gorbunov,L.M. & Shirokov,A.S. (1980) Sov. J. Plasma Phys. **6**,364

81. Haas,R.A. Mead,W.C. Kruer,W.L. Phillion,D.W. Kornblum,H.N. Lindl,J.D. MacQuigg,D. Rupert,V.C. & Tirsell,K.G. (1977) Phys. Fluids **20**,322

82. Hammerling,P. (1978) Plasma Phys. **19**,669

83. Herbst,M.J. Stamper,J.A. Whitlock,R.R. Lehmberg,R.H. & Ripin,B.H. (1981) Phys. Rev. Lett. **46**,328

84. Hordvick,A. & Collins,R.J. (1970) IEEE J. Quantum Electron. **6**,254

85. Hughes,T.P & Nicholosen-Florence,M.B. (1968) J. Phys. **A1**,588

86. Hughes,T.P. (1980) in " Laser Plasma Interactios " , Proc. of 20th SUSSP edited by Cairns,R.A.& Sanderson SUSSP (Edinburgh)

87. Jaanimagi,P.A. Enright,G.D. & Richardson,M.C. (1979) IEEE Trans. Plasma Sci. **PS-7**,166

88. Jackel,S. (1976) Phys. Rev. Lett. **37**,95

89. Jackel,S. Leobenstein,H.M. Zigler,A. Zmora,H. & Zweigenbaum,S. (1980) Appl. Phys. Lett. **36**,34

90. Jackson,E.A. (1967) Phys. Rev. **153**,235

91. Jorna,S. (1974) Phys. Fluids **17**,765

92. Joshi,C. Tajima,T. Dawson,J.M. Baldis,H.A. & Ebrahim,N.A. (1981) Phys. Rev. Lett. **47**,1285

93. Kil'pio,A.V. Malyutin,A.A. & Pashinin,P.P. (1980) Sov. Phys.--JETP Lett. **32**,499

94. Krasyuk,I.K. Pashinin,P.P. & Prokhorov,A.M. (1970) Sov.

Phys.--JETP Lett. **12**,305

95. Krokhin,O.N. Putovalov,V.V. Rupasov,A.A. Silin,V.P. Sklizkov,G.V. Starodub,A.N. Tikhonchuk,V.P. & Shikanov,A.S. (1975) Sov. Phys.--JETP Lett. **22**,21

96. Kruer,W.L. (1980) Phys. Fluids **23**,1273

97. Kruer,W.L. (1982) Phys. Fluids **25**,2324

98. Kruer,W.L. Estabrook,K.G. & Sinz,K.H. (1973) Nuc. Fusion **13**,952

99. Langdon,A.B. (1980) Phys. Rev.Lett. **44**,575

100. Lee,Y.C. & Kaw,P.K. (1974) Phys. Rev. Lett. **32**,135

101. Lee,P. Giovanielli,D.V. Godwin,R.P. & McCall,G.H. (1974) Appl. Phys. Lett. **24**,406

102. Lee,Y.C. & Su,C.H. (1966) Phys. Rev. **152**,129

103. Lin,Z. (1982) Optics Commun. **42**,351

104. Liu,C.S. & Rosenbluth,M.N. (1976) Phys. Fluids **19**,967

105. Liu,C.S. Rosenbluth,M.N. & White,R.B. (1973) Phys. Rev. Lett. **31**,697

106. Liu,C.S. Rosenbluth,M.N. & White,R.B. (1974) Phys. Fluids **17**,1211

107. Maaswinkel,A.G.M. (1980) Opt. Commun. **33**,62

108. Maaswinkel,A.G.M. (1980) Opt. Commun. **35**,236

109. Maaswinkel,A.G.M. Eidmann,K. & Sigel,R. (1979) Phys. Rev. Lett. **42**,1625

110. Malone,R.C. & Morse,R.L. (1975) Phys. Fluids **21**,143

111. Manes,K.R. Rupert,V.C. Auerbach,J.M. Lee,P. & Swain,J.E. (1977) Phys. Rev. Lett. **39**,281

112. Manheimer,W.M. & Colombant,D.G. (1981) Phys. Fluids **24**,2319

113. Manheimer,W.M. & Klein,H.H. (1975) Phys. Fluids **18**,1299

114. Massey,R.S. Pietrzyk,Z.A. & Scudder,D.W. (1978) Phys. Fluids **21**,396

115. Mayer,F.J. Osborn,R.K. Daniels,D.W. & McGrath,J.F. (1978) Phys. Rev. Lett. **40**,30

116. McGoldrick,E.M. & Sim,S.M.L. (1981) Optics Commun. **39**,172

117. McGoldrick,E.M. & Sim,S.M.L. (1980) Optics Commun. **40**,433

118. McLean,E.A. Stamper,J.A. Ripin,B.H. Griem,H.R. McMahon,J.M. &

Bodner,S.E. (1977) Appl. Phys. Lett. **31**,825

119. Mead,W.C. Haas,R.A. Kruer,W.L. Phillion,D.W. Kornblum,H.N. Lindle,J.D. MacQuigg,D.R. & Rupert,V.C. (1976) Phys. Rev. Lett. **37**,489

120. Montes,A. & Hubbard,M. (1978) Plasma Phys. **21**,885

121. Mora,P. & Pellat,R. (1979) Phys. Fluids **22**,2408

122. Ng,A. Pitt,L. Salzmann,D. & Offenberger,A.A. (1979) Phys. Rev. Lett. **42**,307

123. Nicholson-Florence,M.B. (1971) J. Phys. **A4**,574

124. Nishikawa,K. (1968) J. Phys. Soc. Jpn. **24**,916

125. Nishikawa,K. (1968) J. Phys. Soc. Jpn. **24**,1152

126. Nishimura,H. Mima,K. Yanabe,Y. Banjoya,N. Fujita,H. Iba,K. Matoba,M. Nakai,S. & Yamanka,C. (1980) Plasma Phys. **21**,69

127. Nuckolls,J. Wood,L. Thiessen,A. & Zimmerman,G. (1972) Nature (London) **239**,139

128. Offenberger A.A. Cervenan,M.R. Yam,A.M. & Pasternak,A.W. (1976) J. Appl. Phys. **47**,1451

129. Offenberger A.A. Ng,A. & Cervenan,M.R. (1977) Cand. J. Phys. **56**,381

130. Osborn,R.K. (1972) Phys. Rev. **A5**,1660

131. Pearlman,J.S. & Matzen,M.K. (1977) Phys. Rev. Lett. **39**,140

132. Pert,G.J. (1978) Plasma Phys. **20**,175

133. Pert,G.J. (1972) J. Phys. **A5**,1221

134. Piliya,A.D. (1966) Sov. Phys.--Tech. Phys. **11**,609

135. Pustovalov,V.V. & Silin,V.P. (1971) Sov. Phys.--JETP **32**,1198

136. Pustovalov,V.V Silin,V.P Starodub,A.N. & Tikhonchuk,V.T. (1974) Paper at Second Int. Conf. on Plasma Theory, Kiev, 1974

137. Ripin,B.H. McMahon,J.M. McLean,E.A. Manheimer,W.M. & Stamper,J.A. (1974) Phys. Rev. Lett. **33**,634

138. Ripin,B.H. Young,F.C. Stamper,J.A. Armstrong,C.M. Decoste,R. McLean,E.A. & Bodner,S.E. (1977) Phys. Rev. Lett. **39**,611

139. Ripin,B.H. (1977) Appl. Phys. Lett. **30**,134

140. Rosenbluth,M.N. (1972) Phys. Rev. Lett. **29**,565

141. Saleres,A. & Decroisette,M. in Paper at 7th Euro Conf. on Controlled Fusion & Plasma Physics, Lausanne 1975, p.72

142. Sauer,K. (1978) Phys. Lett. **66A**,37

143. Sauer,K. Baumgartel,K. & Auer,G. (1979) Phys. Lett. **74A**,211

144. Schwarzenbach,A.P. Ladrach,P. & Balmer,J.E. (1980) Optics Commun. **39**,247

145. Short,R.W. & Williams,E.A. (1981) Phys. Rev. Lett. **47**,337

146. Silin,V.P. (1973) in " Parmetricheskoe vozdeistvie izlucheniya bol'shoi moschchnosti na plazmu " , Nauka Moscow --paragraphs 7-9 of Chap. II have been translated by RAL.-"Parametric action of high intensity radiation on plasma."

147. Silin,V.P. (1965) Sov. Phys.--JETP **20**,1510

148. Sodha,M.S. Sharma,J.K. Tewari,D.P. Sharma,R.P. & Kaushik,S.C. (1978) Plasma Phys. **20**,825

149. Stamper,J.A. (1977) Appl. Phys. Lett. **31**,574

150. Tarvin,J.A. & Schroeder,R.J. (1981) Phys. Rev. Lett. **47**,341

151. Thomson,J.J. Max,C.E. & Estabrook,K. (1975) Phys. Rev. Lett. **35**,663

152. Venedov (1961) Nuc. Fusion **1**,82

153. Vinogradov,A.V. & Pustovalov,V.V. (1973) Sov. Phys.--JETP **36**,492

154. Vladimirskii,A.B. & Silin,V.P. (1980) Sov. J. Plasma Phys. **6**,196

155. Woo,W & DeGroot,J.S. (1978) Phys. Fluids **21**,124

156. Zaritskii,A.R. Zakharov,S.D. Kryukov,P.G. Matveets,Yu.A. & Fedosimov,A.I. (1972) Sov. Phys.--JETP Lett. **15**,127

CHAPTER THREE

EXPERIMENTAL APPARATUS AND PROCEDURE

3.1 INTRODUCTION

To investigate the second harmonic requires the study of the interaction of intense laser radiation with a dense plasma by spectral measurements of the scattered radiation. It has been possible to make these measurements with two different wavelengths of incident radiation. At Royal Holloway College (RHC) a carbon-dioxide (CO_2) laser provided pulses of 10.6 μm radiation and at the Rutherford Appleton Laboratory (RAL) a neodymium (Nd) laser gave radiation of 1.06 μm. The scaling parameter $I\lambda^2$ was well above 10^{12} W/cm^2μm^2, the threshold for second harmonic generation. Lower intensities or gaseous targets would not give plasmas of sufficiently steep density gradients for large radiation absorption and subsequent conversion to 2w. Table 3.1 presents some of the laser characteristics.

The following sections will briefly describe the two laser systems along with the diagnostics used to characterise the laser radiation and to determine the plasma parameters.

TABLE 3.1 LASER CHARACTERISTICS

LASER SYSTEM	CO_2	Nd	
Wavelength,	10.6	1.06	μm
Max. Energy	25	100	J
Peak Power	0.5	60	GW
Irradiance(max)	$1.5*10^{12}$	$2*10^{14}$	W/cm^2
Spot size	<200	100	μm
Duration	50	1.7	nsec

3.2 CO_2 LASER SYSTEM

3.2.1 INTRODUCTION

At RHC a tranversely excited atmospheric pressure (TEA) CO_2 laser provided pulses of ~50 nsec duration at 10.6 μm with energies of up to 15 J. The interaction of this intense radiation with a dense target was studied in order to confirm or deny related theoretical concepts.

The TEA CO_2 laser used in this study has been described before [1,7], so the treatment presented here will be brief, emphasising any additions and improvements made. The important characteristics of the laser have been noted earlier in Table 3.1 and in the following Table 3.3.

A succinct historical account of the CO_2 laser is presented in Apppendix A along with its theory of operation.

3.2.2 GENERAL DESCRIPTION

The laser was a pulsed TEA (transversely excited atmospheric) CO_2 laser [1,7] with either a grating-mirror or an unstable mirror cavity as shown schematically in Figure 3.1. The oscillator and amplifier modules were interconnected and filled with a gas mixture of helium, carbon-dioxide and nitrogen at atmospheric pressure. The optimum mixture of the gases was, experimentally, found to be in the ratio 6:3:2 for $He:CO_2:N_2$ (see later).

Lasing takes place between the rotational levels of the symmetric and asymmetric mode of vibration of the CO_2 molecule provided a

population inversion exists between these levels (see appendix A for a more complete theory of operation). The inversion arises by exciting the higher CO_2 levels vibrationally via excited N_2 molecules. The process being highly efficient since the thermal energy at room temperatures ~1/40 eV (200 cm^{-1}) whilst separation of the CO_2 and N_2 levels is only ~1/400 eV (18 cm^{-1}). The helium gas ensures a satisfactory discharge, a rapid depopulation of the lower levels and cooling thereafter.

The gas mixture was excited by applying a 2 μsec pulse of 50 KV across the electrodes (Figure 3.1). A uniform gas discharge was then initiated by putting the full voltage to the trigger wires in glass capillary tubes (approx. 160 of them placed into grooves in the cathode). This provided pre-ionisation and prevented arcing on most occasions (see circuit diagrams in figs. 3.6-3.8). A poor nonuniform discharge resulted during arcing, leading to a weak laser output. Thus care was taken to prevent this by ensuring that

(a) a correct gas mix flowed for a sufficient time (~1/2 hr) before the first shot. If no arcing resulted then a shot every two minutes was possible,

(b) the electrode plates were clean and parallel with a separation of ~5 cm. Cleaning being necessary every 8-10 weeks, and

(c) the trigger rods were clean.

PULSE SHAPE :

Figures 3.2(a,b) show typical CO_2 laser temporal profiles. It is seen that the laser power output consists of an initial sharp spike followed by a lower intensity broad tail of radiation. The existence of the tail can be deduced from the solution of the coupled set of rate

equations for the $He:CO_2:N_2$ mixture [8]. Basically the N_2 excited level has a large population density existing for a long time, which vibrationally transfers to the CO_2 molecule giving a rapid initial pulse. Since excited N_2 molecules still exist, further transfers give weaker and weaker pulses leading to the observed tail. Over 50% of the energy is in the shorter pulse, so that in terms of power and irradiance this is the most effective.

BEAM QUALITY :

A CO_2 laser burn pattern on exposed polaroid is shown in figs. 3.3 & 3.4. Both indicate an intense central feature surrounded by a weaker feature. The burn shot (Fig. 3.3) which is nearly circular was taken without any apertures from a mirror cavity. Figure 3.4 is from a grating cavity - note that it consists of intense stripes with a central hot region and also shows that the grating is rectangular.

GAS MIXTURE :

The optimum gas mix was determined by monitoring the variation in output energy with changes in the gas flow. A calorimeter (Gentec Model ED-500) was used to monitor the laser energy (see figs. 3.1 & 3.18) by inserting a salt flat in the beam. One gas flow was varied at a time whilst the other two were held fixed and about ten minutes were allowed for the mixture to settle before taking five or more results. The averaged results are plotted in Fig. 3.5(a-c) for the three gases - Note that after determining an optimum for one gas it was then fixed at this value for the next set of data. From the plots we conclude optimum flow values of 6:2:3 for $He:N_2:CO_2$ respectively. The CO_2 laser was operated at these optimum values from then on.

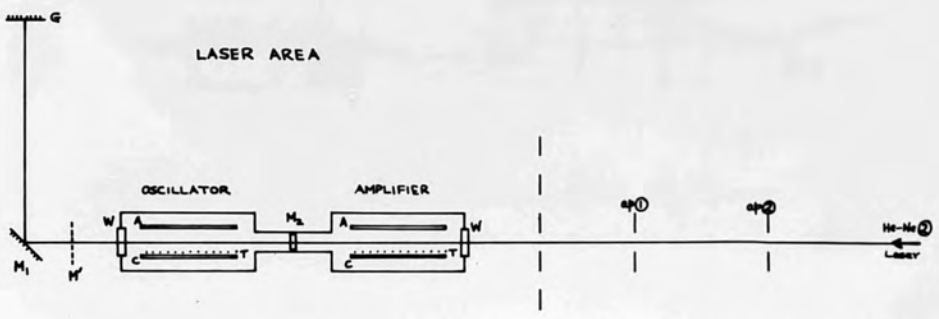

FIGURE 3.1 : CO_2 LASER
(OSCILLATOR & AMPLIFIER).

W - Salt(KCl) or Zinc Selenide(ZnSe) windows AR coated for 10.6 μm

M_1- 100% reflecting Au-Cu mirror (75 mm diam.)

M_2- 66%R, 33%T at 10 μm Germanium mirror(50mm)

G - Grating (see Table 3.2)

*A - Anode electrode (110*7*1.5 cm)*

*C - Cathode electrode (100*7*1.5 cm)*

M'- Au-Cu concave mirror (f~10m, diam.~50mm)

T - Preionising glass trigger rods (~155) 4.5mm diam. with 0.4mm Nichrome wire.

ap- Variable apertures.

AC- Electrode seperation ~5 cm.

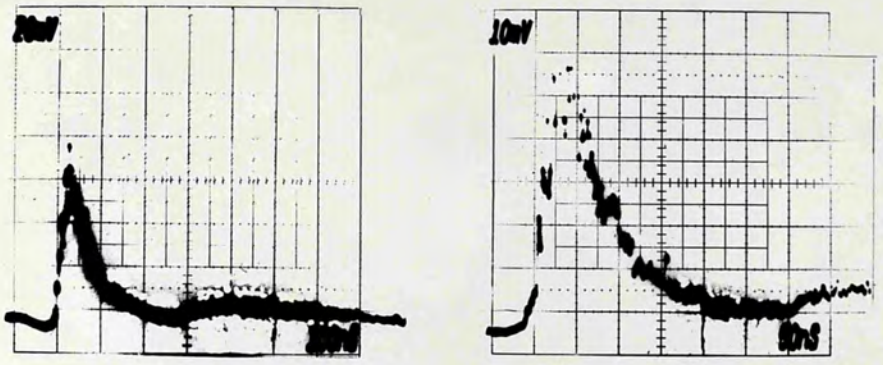

FIGURE 3.2 : Temporal profiles of CO_2 laser

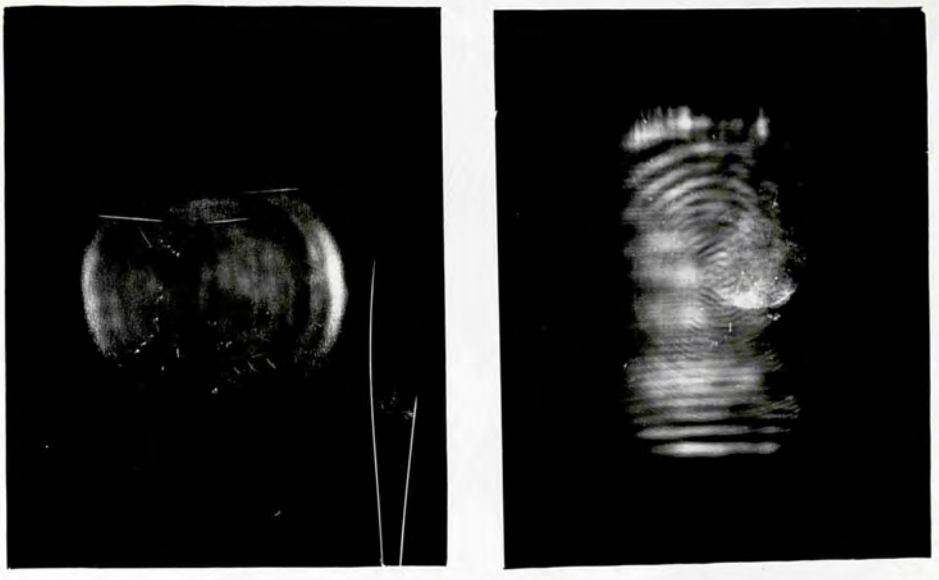

3.3 : Mirror Cavity 3.4 : Grating Cavity

FIGURES 3.3 & 3.4 : CO_2 burn patterns on exposed polaroid

TABLE 3.2

CO_2 LASER GRATING.

Size	: 50*25	mm
Ruling	: 135	lines/mm
Blaze	: 10.6	μm
Blaze Angle	: 45	degrees
Reflectivity	: 98%	@ 10.6μm
Damage threshold	: >10	J/cm^2
Angular dispersion	: 55	Å/mrad

TABLE 3.3

TEA CO_2 LASER CHARACTERISTICS.

Gas mix	: $He:CO_2:N_2$ - 6:3:2	
Charging voltage	: 50	kV
Charging current	: <20	kA
Wavelength	:10.5-10.6	μm
Energy	: <20	J
Pulse(fwhm)	: 50	nsec
Power	: <400	MW
Irradiance	: $<10^{12}$	W/cm^2
Linewidth	: <80	Å for grating cavity,
	100	Å for mirror cavity.
Divergence	: 5-10	mrad
Cavity length	: >4 meters(~2m for mirror cavity)	
Critical density(n_c)	: $9.96*10^{18}$	cm^{-3}

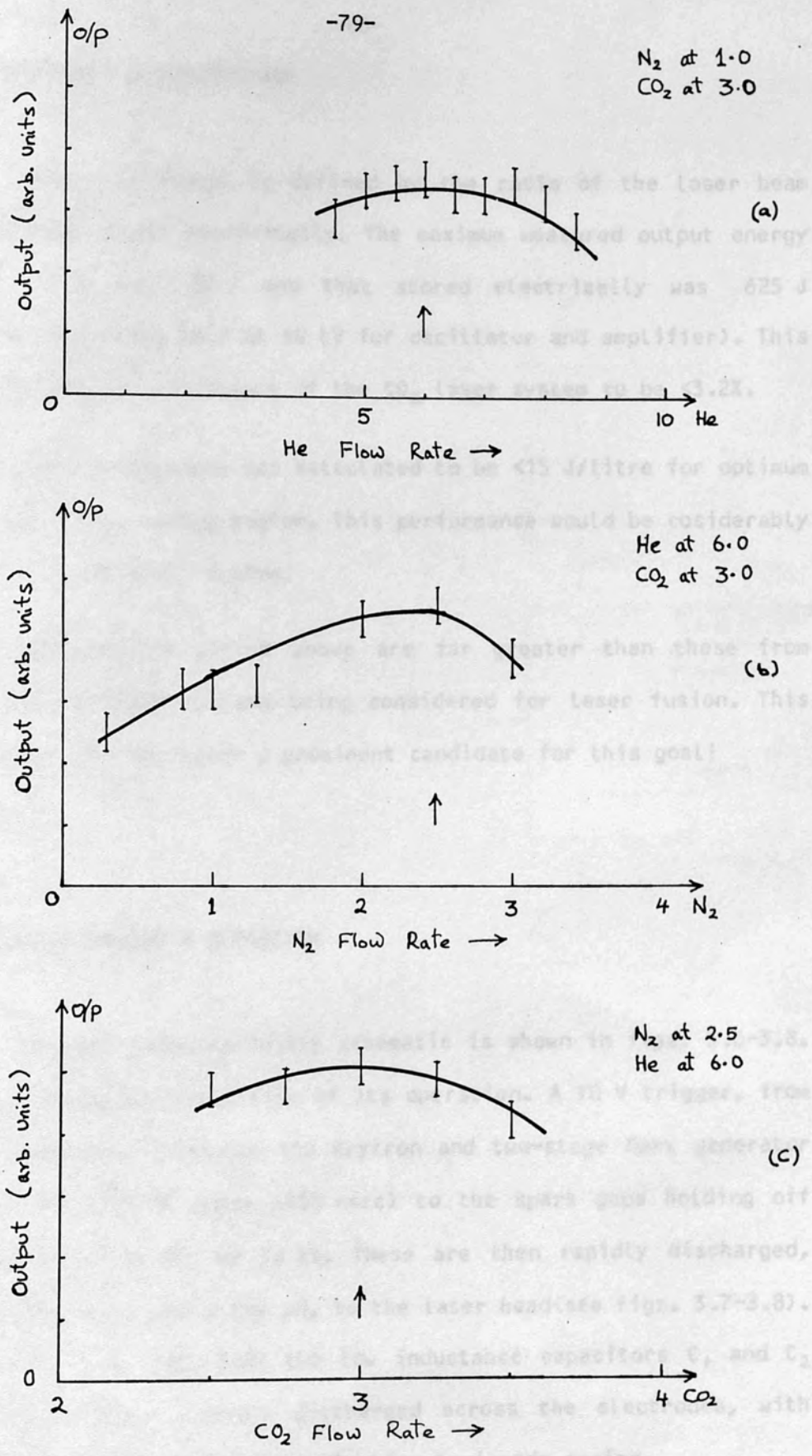

FIGURE 3.5 : CO_2 laser output energy for various gas flows.

3.2.3 EFFICIENCY & PERFORMANCE

The laser efficiency is defined by the ratio of the laser beam energy to that stored electrically. The maximum measured output energy from the laser was 20 J and that stored electrically was 625 J (2*0.25 μF capacitors held at 50 kV for oscillator and amplifier). This implies the overall efficiency of the CO_2 laser system to be <3.2%.

The laser performance was calculated to be <15 J/litre for optimum gas mixture in the lasing region. This performance would be cosiderably greater for a multipass system.

The efficiencies quoted above are far greater than those from neodymium-glass laser systems being considered for laser fusion. This is what made the CO_2 laser a prominent candidate for this goal!

3.2.4 CIRCUIT DESIGN & OPERATION

The relevant laser circuitry schematic is shown in figs. 3.6-3.8. Figure 3.6 shows the simplicity of its operation. A 10 V trigger, from a pulse generator, initiates the Krytron and two-stage Marx generator to give a rapid 30 kV pulse (<10 nsec) to the spark gaps holding off capacitors (of 0.25 μF) at 50 kV. These are then rapidly discharged, via an inductance L_o of a few μH, to the laser head(see Figs. 3.7-3.8). At the laser head (Fig. 3.8) the low inductance capacitors C_1 and C_2 are pulsed and then rapidly discharged across the electrodes, with R_1/C_3 combination providing preionisation to impede arcing.

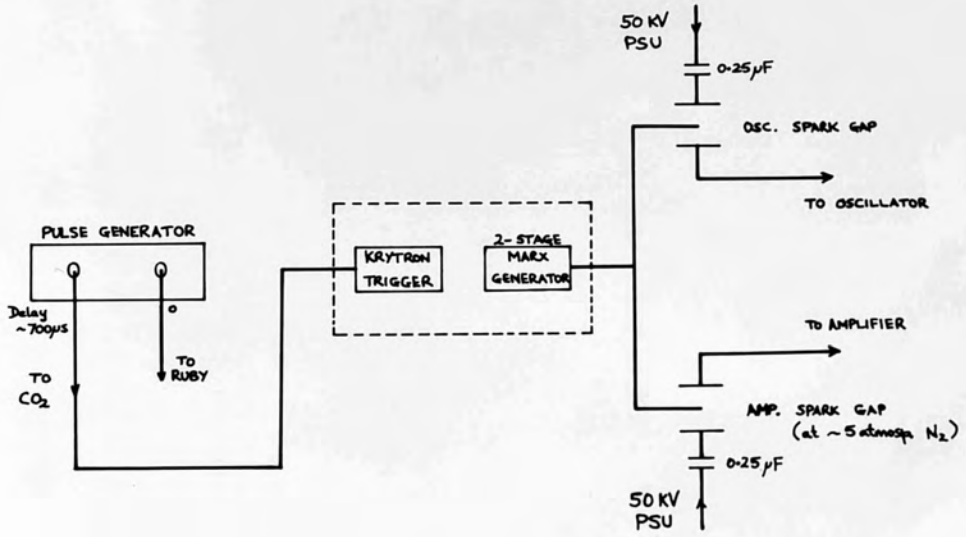

FIGURE 3.6 : General arrangement of laser circuitry

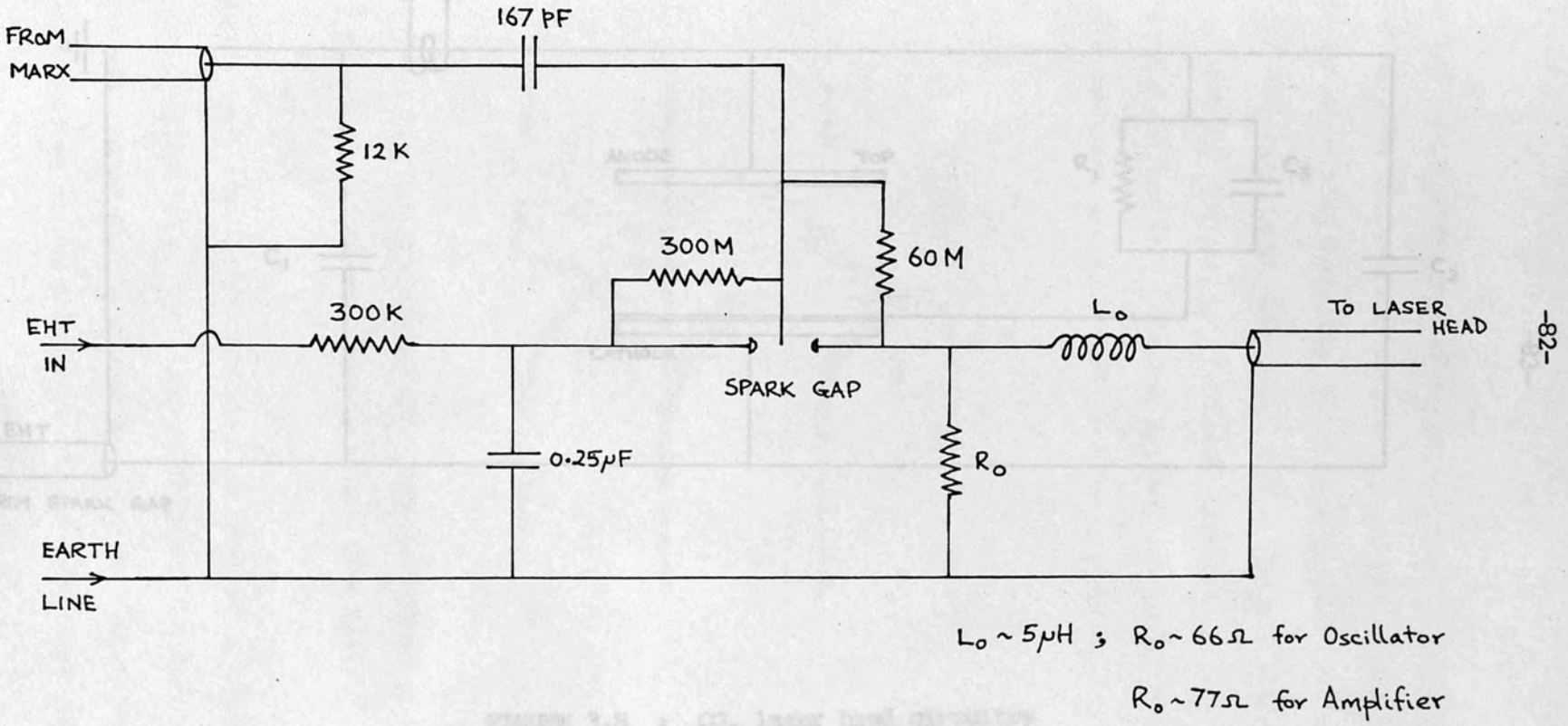

FIGURE 3.7 : Spark-gap circuitry

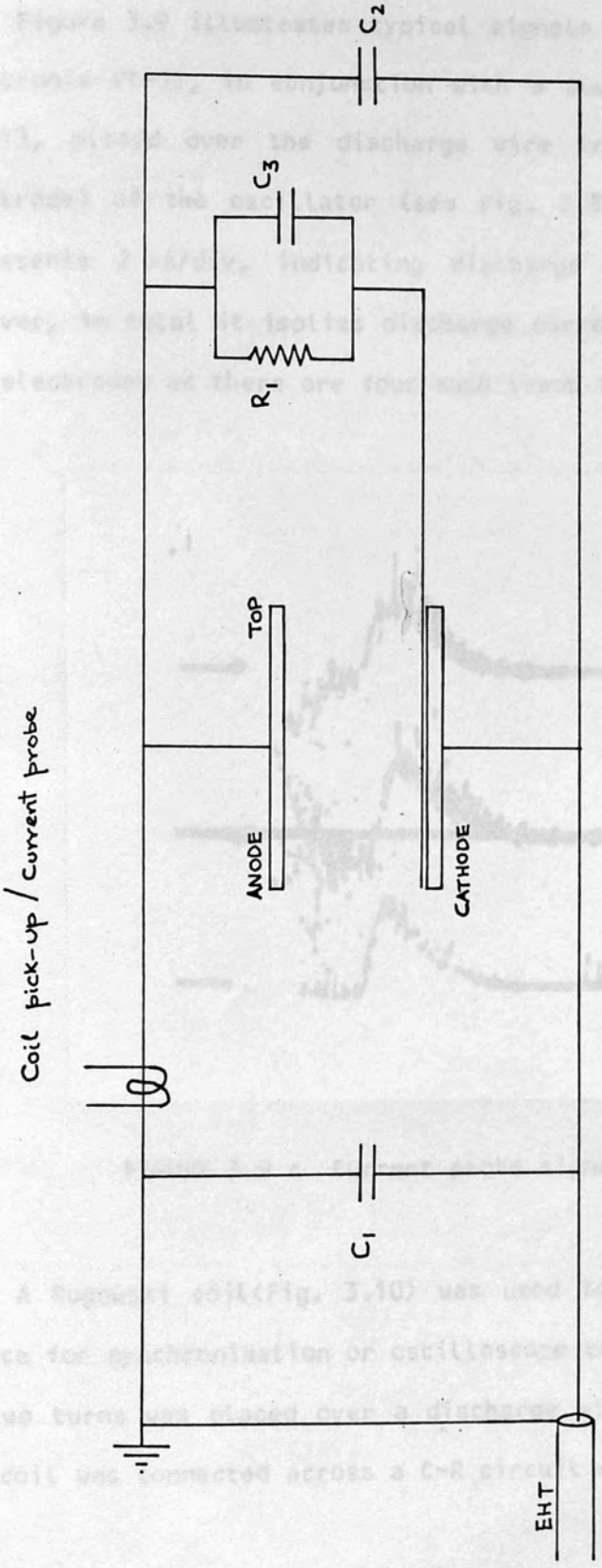

FIGURE 3.8 : CO_2 laser head circuitry

Figure 3.9 illustrates typical signals from a high current probe [Tektronix CT-5], in conjunction with a low current probe [Tektronix P6021], placed over the discharge wire from C_1 to the anode (top electrode) of the oscillator (see Fig. 3.8). The oscilloscope trace represents 2 kA/div, indicating discharge currents of up to 5 kA. However, in total it implies discharge currents of up to 20 kA between the electrodes as there are four such leads to the anode.

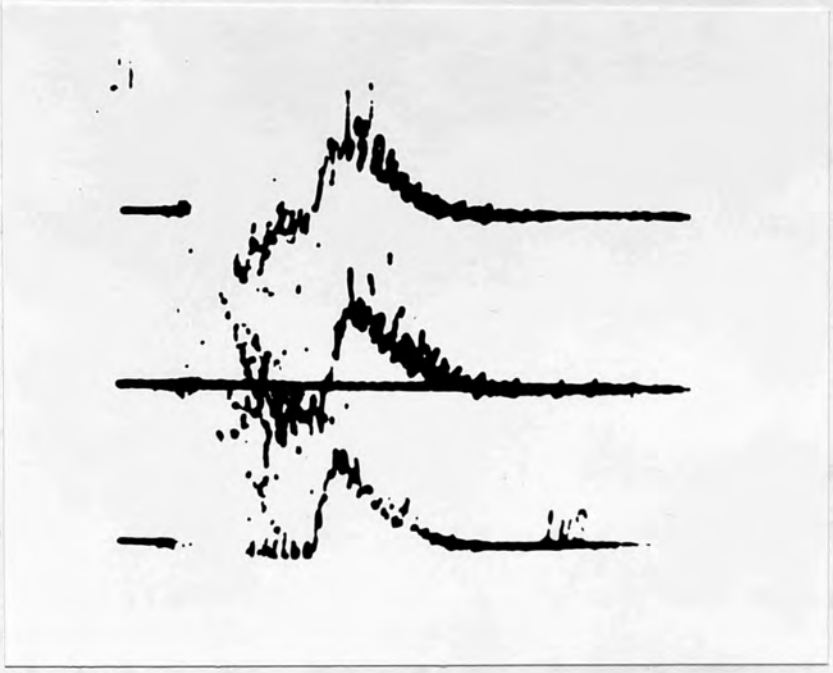

FIGURE 3.9 : Current probe signals (see text).

A Rogowski coil(Fig. 3.10) was used to provide a timing/trigger source for synchronisation or oscilloscope trigger. The coil consisting of two turns was placed over a discharge wire, as with current probe. The coil was connected across a C-R circuit where C=120 pF and R=150Ω.

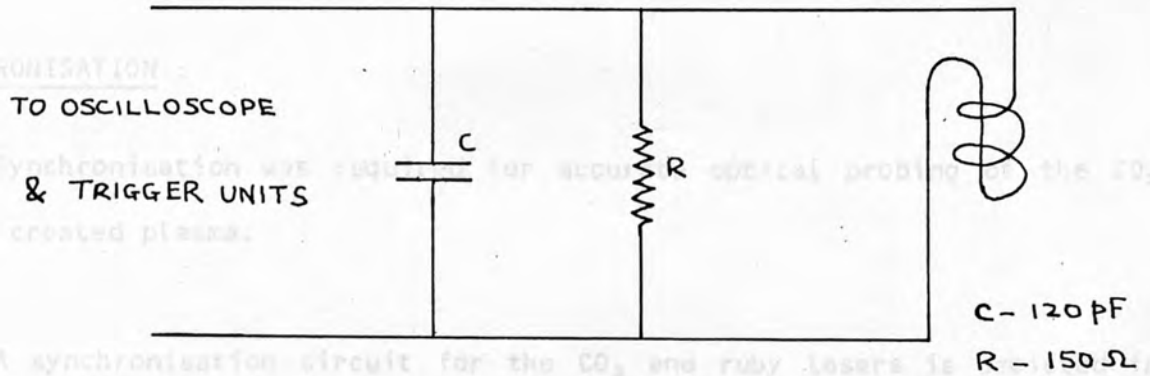

FIGURE 3.10 : Rogowski coil pick-up

An example of the pulse from this coil is shown in Fig. 3.11. This shows clearly the noise due to the Marx and spark-gaps preceding the signal.

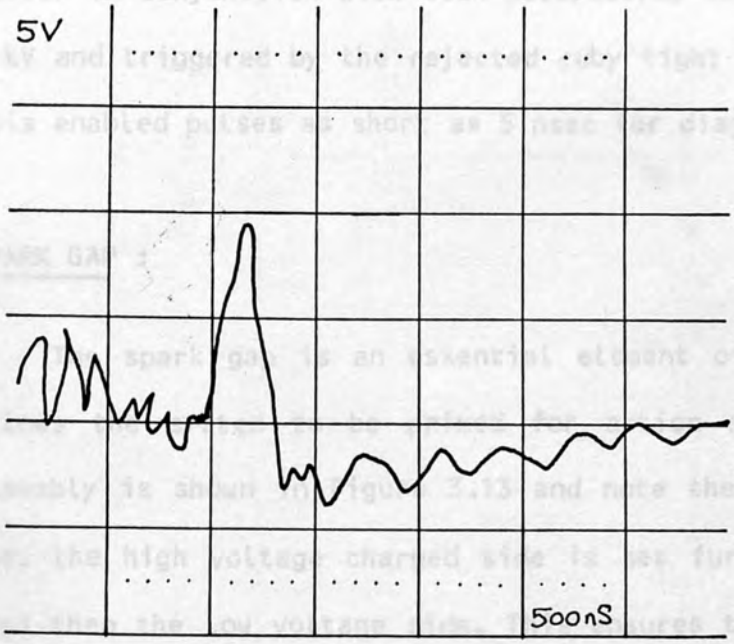

Note that the signal is +ve during discharge before going -ve as the discharge fades. The noise level is below 5 V and thereby does not initiate the trigger unit whilst the coil signal does.

FIGURE 3.11 : Typical coil signal.

The coil provided a stable trigger source for the oscilloscopes and timing with a jitter <10 nsec. The Marx trigger, without the coil, had a jitter of >4 μsec, due to the unpredictability of the spark gap. The CO_2

laser output followed the coil signal with a delay of ~1 μsec.

SYNCHRONISATION :

Synchronisation was required for accurate optical probing of the CO_2 laser created plasma.

A synchronisation circuit for the CO_2 and ruby lasers is depicted in Fig. 3.12. This makes use of the Rogowski coil pick-up signal to trigger the cavity pockell cell of the ruby laser with an appropriate delay. The ruby flashlamps having been triggered some 700 μsec before the CO_2 Marx to allow for sufficient population inversion in the ruby rod. The ruby pulse ($\hat{\tau} \sim 40$ nsec) could be further clipped using a laser triggered spark gap (LTSG) in conjunction with Glan-polarisers. The LTSG was usually charged to 7 kV and triggered by the rejected ruby light off the first Glan-polariser. This enabled pulses as short as 5 nsec for diagnostics [9].

SPARK GAP :

The spark gap is an essential element of the CO_2 laser system as it allows the system to be primed for action and fired at will. The spark assembly is shown in Figure 3.13 and note the asymmetry of the electrodes, i.e. the high voltage charged side is set further from the centre trigger pins then the low voltage side. This ensures the stability of the system [A symmetrical configuration was tried but failed to hold off the high voltages as it often self-triggered]. The spark gap was pressurised to ~ 5 atmosphere with nitrogen gas to prevent self-triggering. One cause for self-triggering was the bad state of the gap and electrodes. These required cleaning every six to eight weeks if the laser was used extensively.

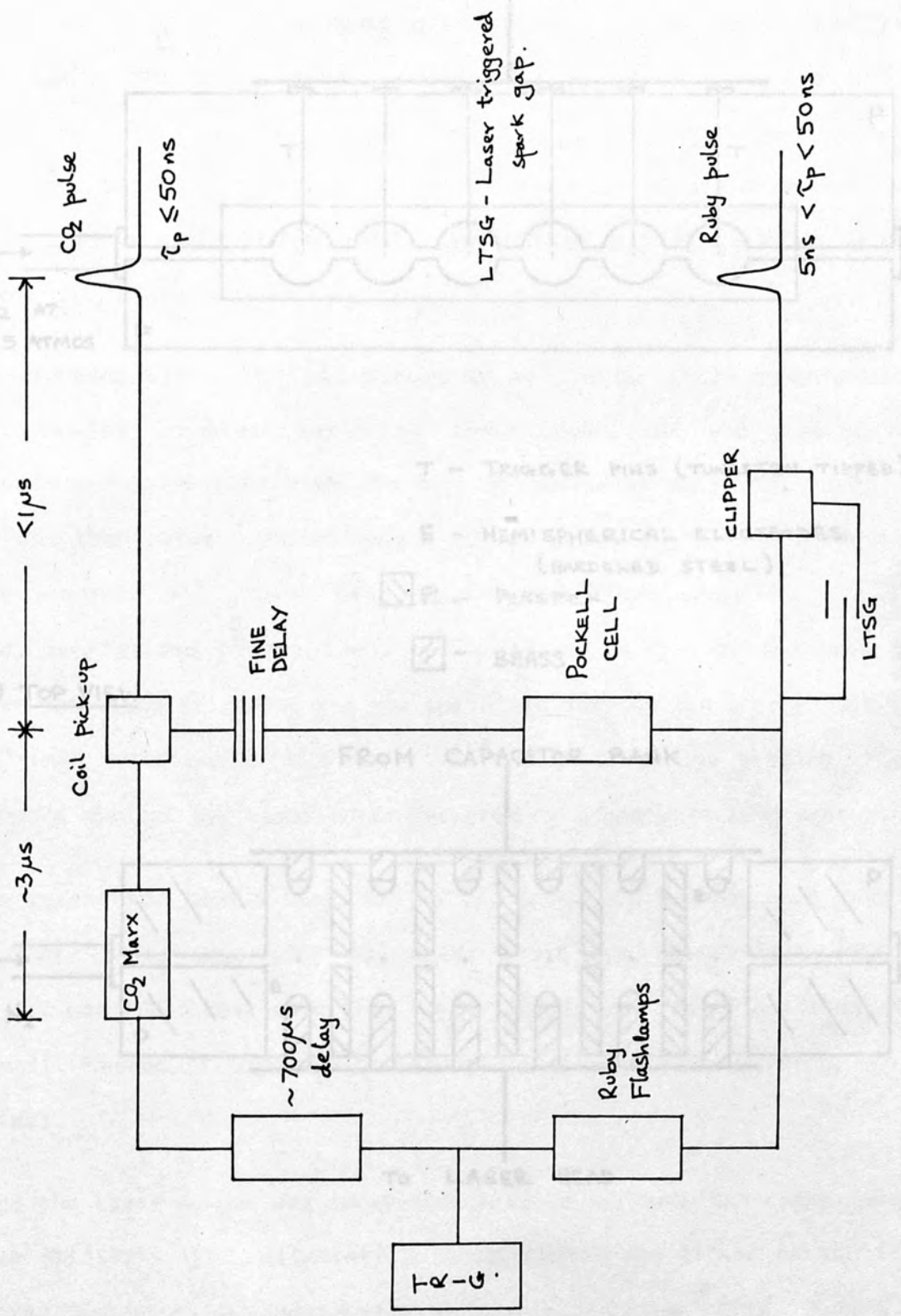

FIGURE 3.12 : Synchronisation of CO_2 and ruby lasers

(a) SIDE VIEW

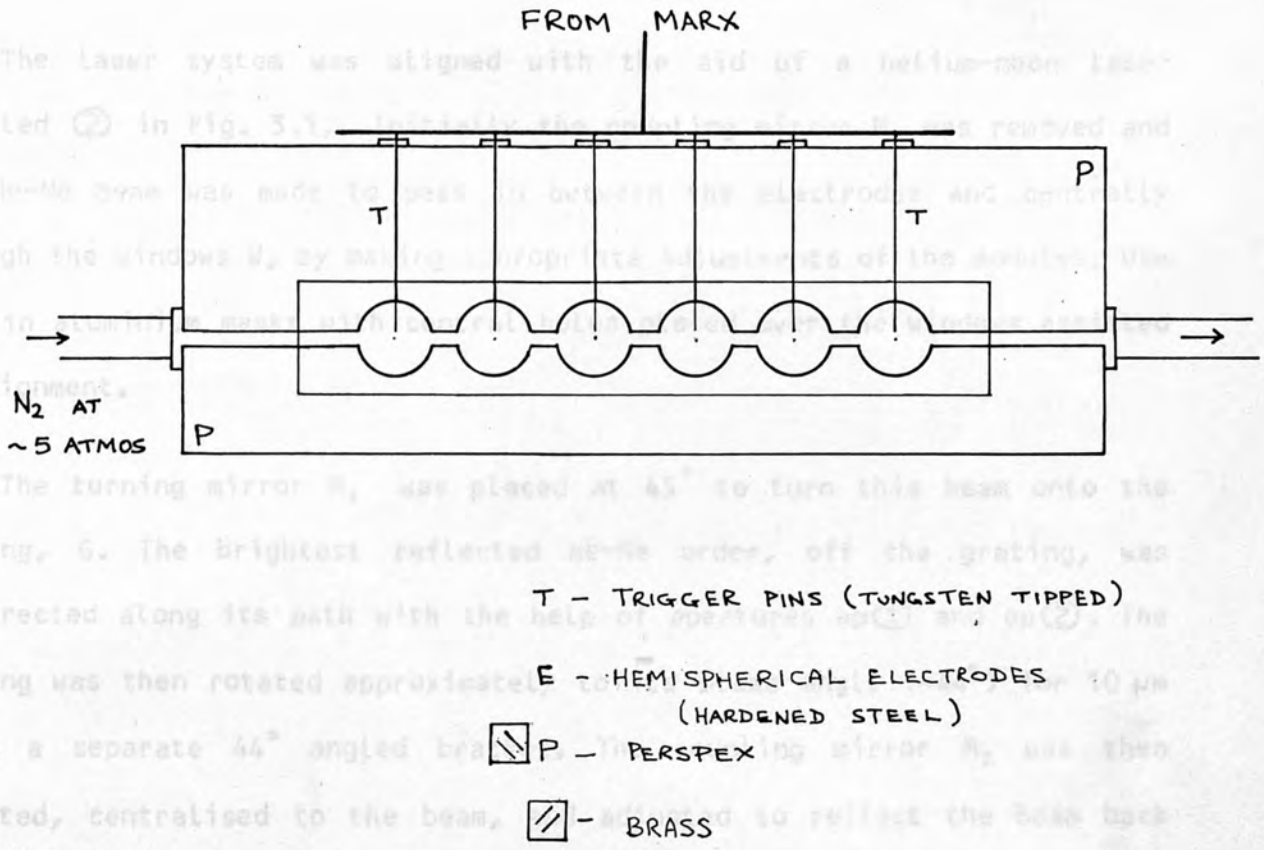

(b) TOP VIEW

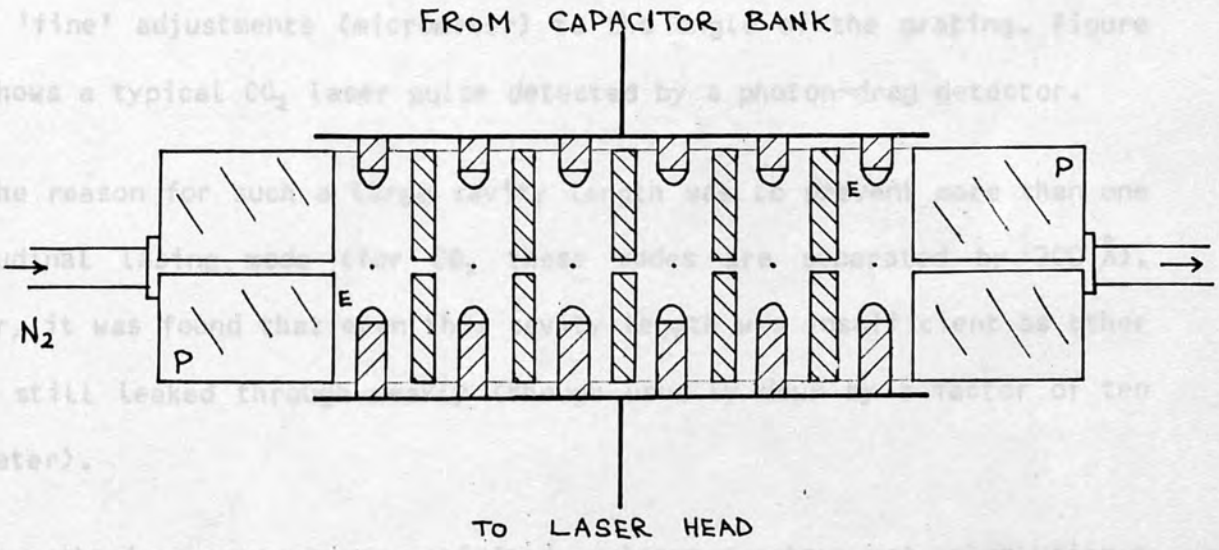

FIGURE 3.13 : CO_2 laser spark-gap assembly.

3.2.5 ALIGNMENT

The laser system was aligned with the aid of a helium-neon laser labelled ② in Fig. 3.1. Initially the coupling mirror M_2 was removed and the He-Ne beam was made to pass in between the electrodes and centrally through the windows W, by making appropriate adjustments of the modules. Use of thin aluminium masks with central holes placed over the windows assisted in alignment.

The turning mirror M_1 was placed at 45° to turn this beam onto the grating, G. The brightest reflected He-Ne order, off the grating, was re-directed along its path with the help of apertures ap① and ap②. The grating was then rotated approximately to its blaze angle (~44°) for 10 μm using a separate 44° angled bracket. The coupling mirror M_2 was then inserted, centralised to the beam, and adjusted to reflect the beam back along its path. The alignment was now optimised for maximum energy output by making 'fine' adjustments (micrometer) to the angle of the grating. Figure 3.2 shows a typical CO_2 laser pulse detected by a photon-drag detector.

The reason for such a large cavity length was to prevent more than one longitudinal lasing mode (for CO_2 these modes are separated by 200 Å). However, it was found that even this cavity length was insufficient as other orders still leaked through weakly (though usually down by a factor of ten or greater).

Once the laser output was optimised, a laser spectrum was taken using a salt beam splitter, lens, attenuators, spectrometer and either an amplified photon-drag detector or gold-doped germanium detector (Fig. 3.18). An example is shown in Fig. 3.14 for a grating cavity. This could be repeated for different micrometer readings (tilt of grating). It was then possible to tune to a particular grating line using the plot of output energy versus

micrometer reading (Fig. 3.15) [Note that if the laser was discharged at full voltage (50 kV) then it was difficult to observe the tuning feature of the grating so 45 kV was used instead].

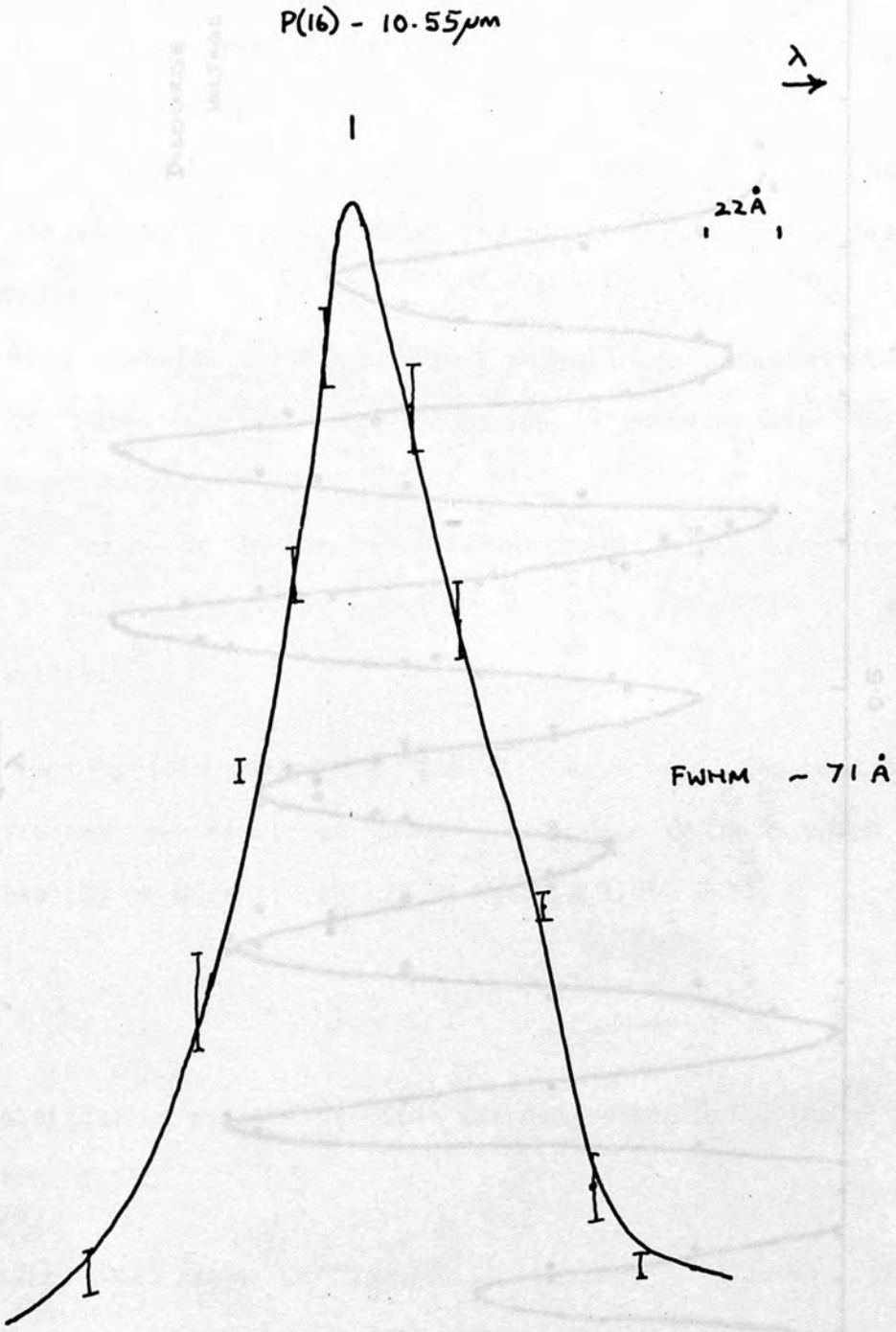

FIGURE 3.14 : CO_2 laser spectrum with a grating cavity.

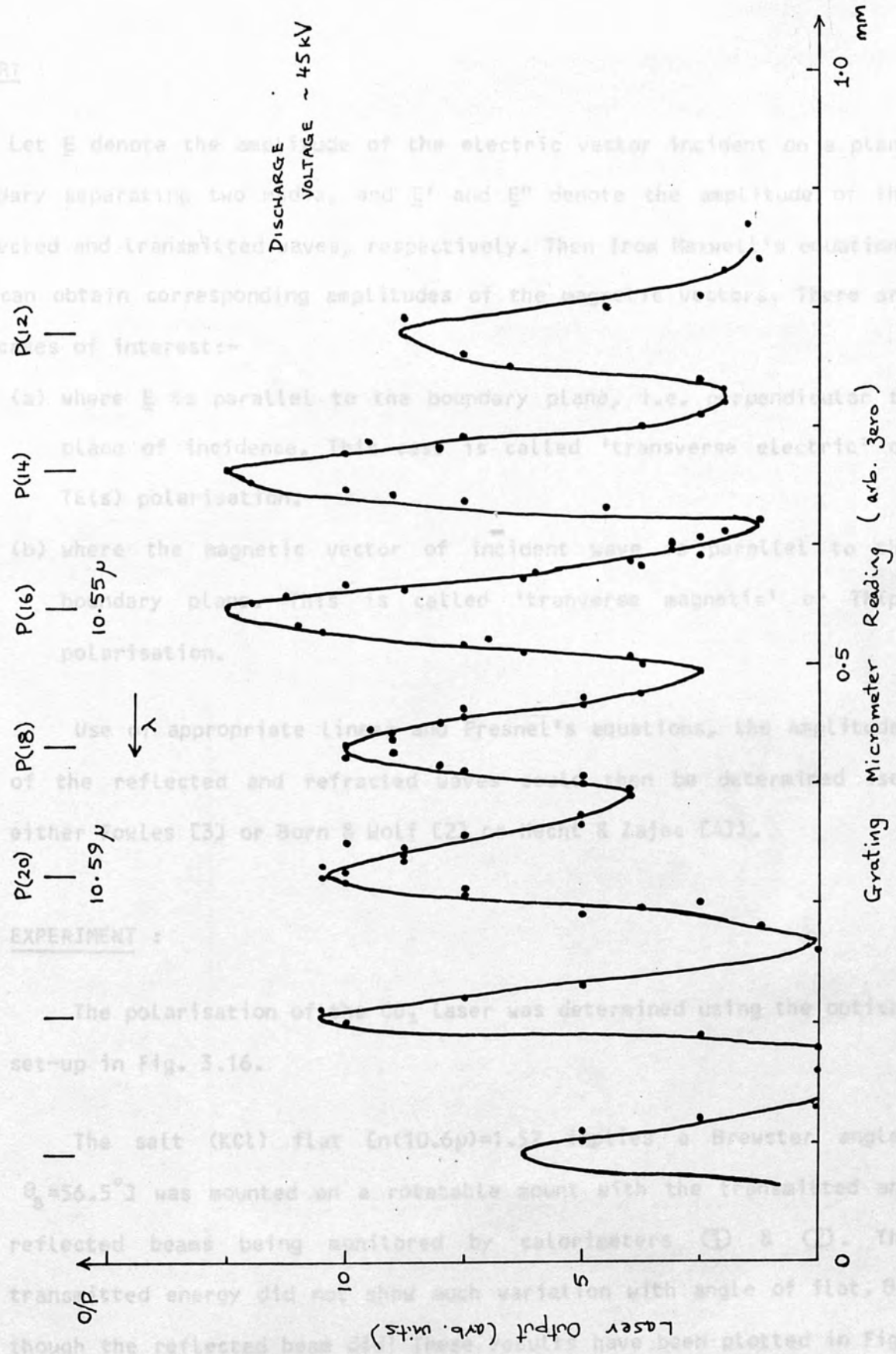

FIGURE 3.15 : Grating line selection

3.2.6 CO_2 POLARISATION

THEORY :

Let $\underline{E}$ denote the amplitude of the electric vector incident on a plane boundary separating two media, and $\underline{E}'$ and $\underline{E}''$ denote the amplitude of the reflected and transmitted waves, respectively. Then from Maxwell's equations one can obtain corresponding amplitudes of the magnetic vectors. There are two cases of interest:-

(a) where $\underline{E}$ is parallel to the boundary plane, i.e. perpendicular to plane of incidence. This case is called 'transverse electric' or TE(s) polarisation.

(b) where the magnetic vector of incident wave is parallel to the boundary plane. This is called 'tranverse magnetic' or TM(p) polarisation.

Use of appropriate linear and Fresnel's equations, the amplitudes of the reflected and refracted waves could then be determined (see either Fowles [3] or Born & Wolf [2] or Hecht & Zajac [4]).

EXPERIMENT :

The polarisation of the CO_2 laser was determined using the optical set-up in Fig. 3.16.

The salt (KCl) flat [$n(10.6\mu)=1.52$ implies a Brewster angle, $\theta_B=56.5^\circ$] was mounted on a rotatable mount with the transmitted and reflected beams being monitored by calorimeters ① & ②. The transmitted energy did not show much variation with angle of flat, θ, though the reflected beam did! These results have been plotted in Fig. 3.17.

The results imply that the laser is essentially p-polarised (TM mode), i.e. the magnetic vector of the incident wave is parallel to the boundary plane (see theory above). When the experiment was repeated for the salt flat on a horizontal mount no polarisation feature was observed, indicating that it was not partially s-polarised.

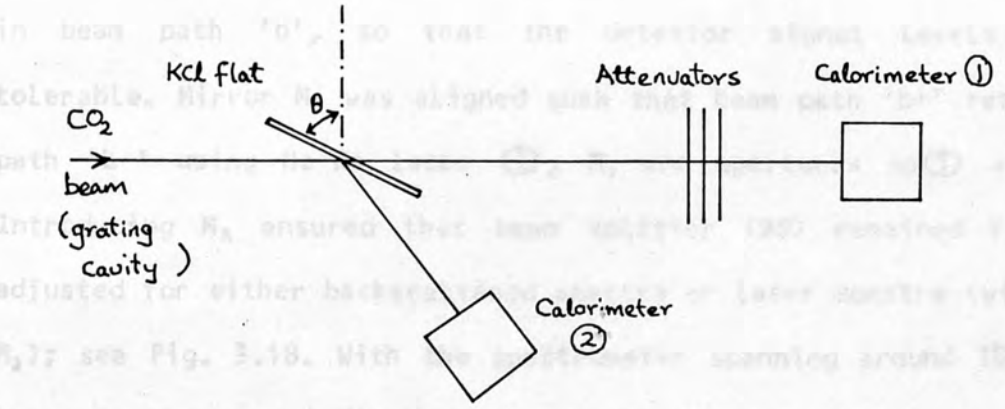

FIGURE 3.16 : Optical arrangement to determine the CO_2 laser polarisation.

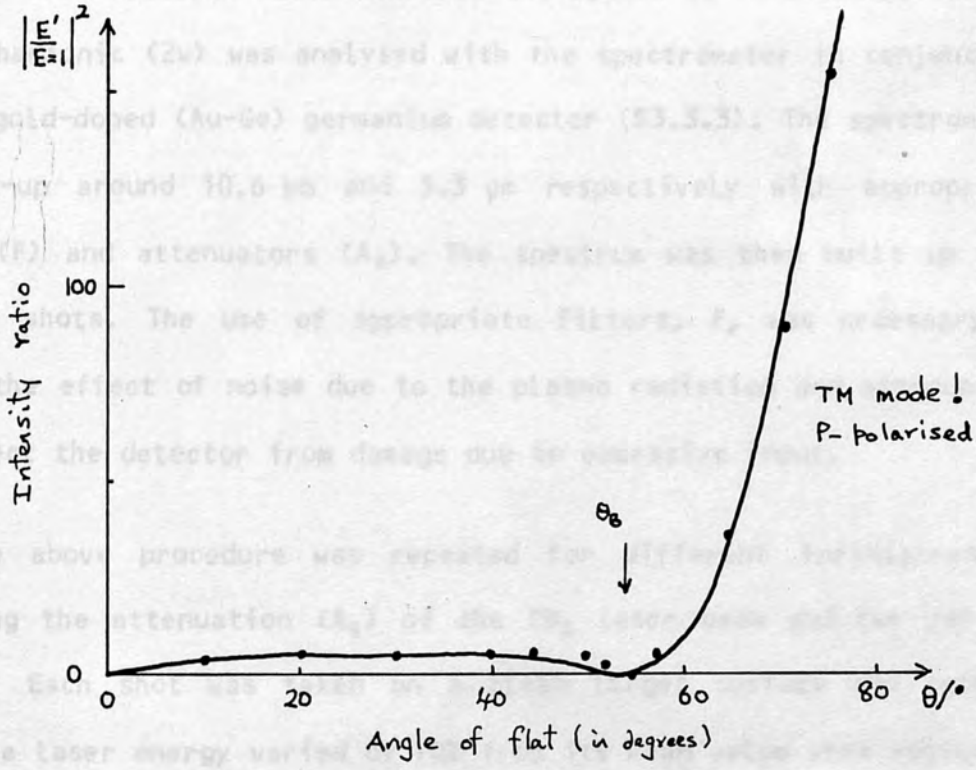

FIGURE 3.17 : Polarisation of CO_2 laser.

3.3 PROCEDURE (CO_2 SYSTEM)

3.3.1 OPTICAL LAYOUT

Figure 3.18 shows the general optical layout used to obtain spectral data for fundamental and second harmonic. The laser spectrum was obtained using sufficient attenuators Ⓐ with mirror M_2 introduced in beam path 'b', so that the detector signal levels remained tolerable. Mirror M_1 was aligned such that beam path 'b+' retraced its path 'b-' using He-Ne laser ①, M_1 and apertures ap① and ap②. Introducing M_2 ensured that beam splitter (BS) remained fixed once adjusted for either backscattered spectra or laser spectra (with mirror M_2); see Fig. 3.18. With the spectrometer scanning around 10.6 μm the laser spectrum was built up from over 80 shots.

The backscattered radiation from the plasma at fundamental (w) and second harmonic (2w) was analysed with the spectrometer in conjunction with a gold-doped (Au-Ge) germanium detector (**§3.3.3**). The spectrometer was set-up around 10.6 μm and 5.3 μm respectively with appropriate filter (F) and attenuators (A_2). The spectrum was then built up from over 80 shots. The use of appropriate filters, F, was necessary to reduce the effect of noise due to the plasma radiation and attenuators to protect the detector from damage due to excessive input.

The above procedure was repeated for different irradiances by adjusting the attenuation (A_1) of the CO_2 laser beam and for various targets. Each shot was taken on a clean target surface and results where the laser energy varied by 10% from its mean value were rejected. The target chamber was typically pumped down to pressures of less than 10^{-3} torr for all experiments.

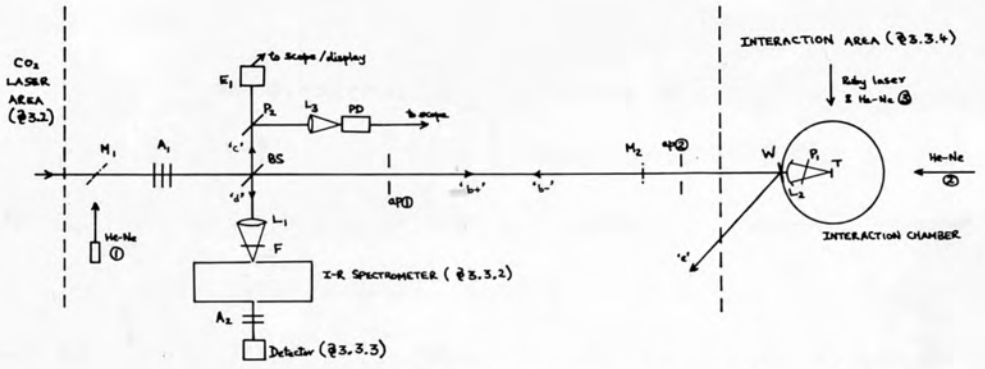

B.S. - Salt(KCl) beam splitter (T>85%; R<15% @ 10μm)
P_1, P_2 - Pellicle(Polythene) (T>85%; R<15% @ 10μm)
L_1, L_3 - KCl lenses.
L_2 - Germanium meniscus focusing lens (F/2, d~60mm)
PD - Photon drag detector (§3.3.3)
E_1 - Calorimeter (§3.3.3)
He-Ne (1)&(2) used for CO_2 alignment.
He-Ne (3) used for target & Ruby laser alignment.

A_1, A_2 - Attenuators
M_1, M_2 - Au-Cu Mirrors
ap(1)&(2) Large apertures
W - Chamber window (ZnSe or KCl)
b,c,d,e- beam paths (see text)
F - Filters
T - Target
He-Ne - Helium neon lasers

FIGURE 3.18 : OPTICAL LAYOUT (RHC).

3.3.2 INFRA-RED SPECTROMETER

The spectrometer was of Czerny-Turner type configuration [5]. It basically consisted of a set each of slits, plane mirrors M_3, M_6 and 20 cm diameter concave mirrors M_4, M_5 (see Fig. 3.19). In addition to these there was a rotatable table on which two gratings (Table 3.4) and a mirror were mounted.

The spectrometer (Fig. 3.19 and Table 3.4) was aligned using He-Ne laser ① with mirrors M_1 and M_2 (Fig. 3.18) in beam path 'b'. The He-Ne laser being first directed, by M_1, along the CO_2 beam axis with the aid of apertures ap① and ap②, before being directed back along its path by M_2. The beam splitter (BS) and lens (L_1) ensured that this beam was focused onto the centre of the slightly curved entrance slits. The system was then aligned such that the beam was central on all the mirrors, gratings and focused centrally onto the exit slits. Thus there was no net magnification for the system.

The grating table could be rotated by stepper motor or manually by the attached micrometer. Initial calibration of the gratings was achieved using a SP50 Golay detector in conjunction with a 10.69 μm filter (see Appendix B) and a Globar infra-red radiation source. The He-Ne orders and the 10.69 μm filter mark gave the required calibration for the gratings (see plots in Fig. 3.20(a) & (b) and Table 3.4).

In order to obtain a spectrum, say, the laser profile, the spectrometer was brought to a He-Ne order just below 10.6 μm and then incremented by a calculated amount to 10.6 μm before scanning. Similarly for second harmonic spectrum but on different grating and He-Ne order just below 5.3 μm.

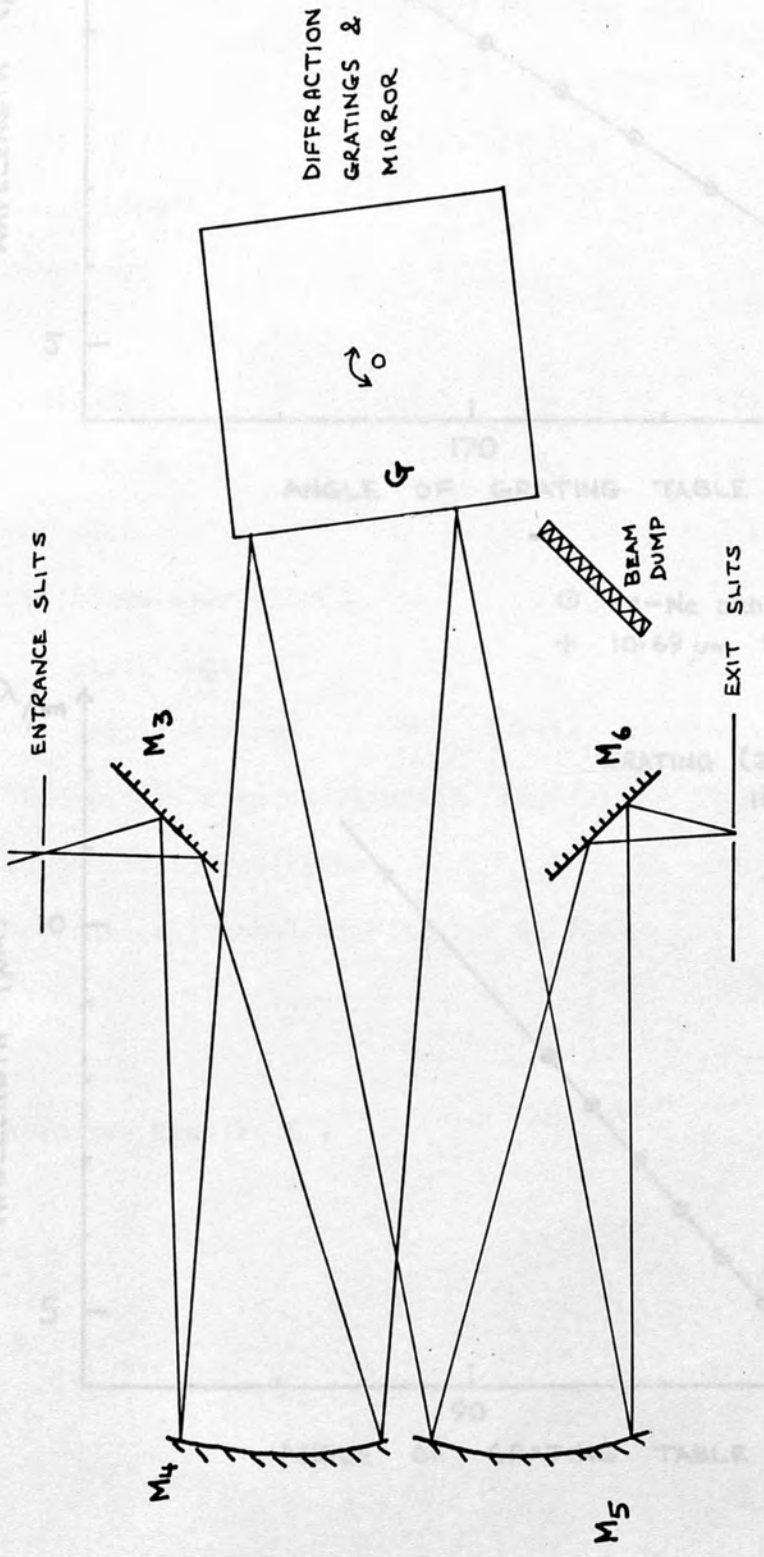

FIGURE 3.19 : Optical layout of spectrometer

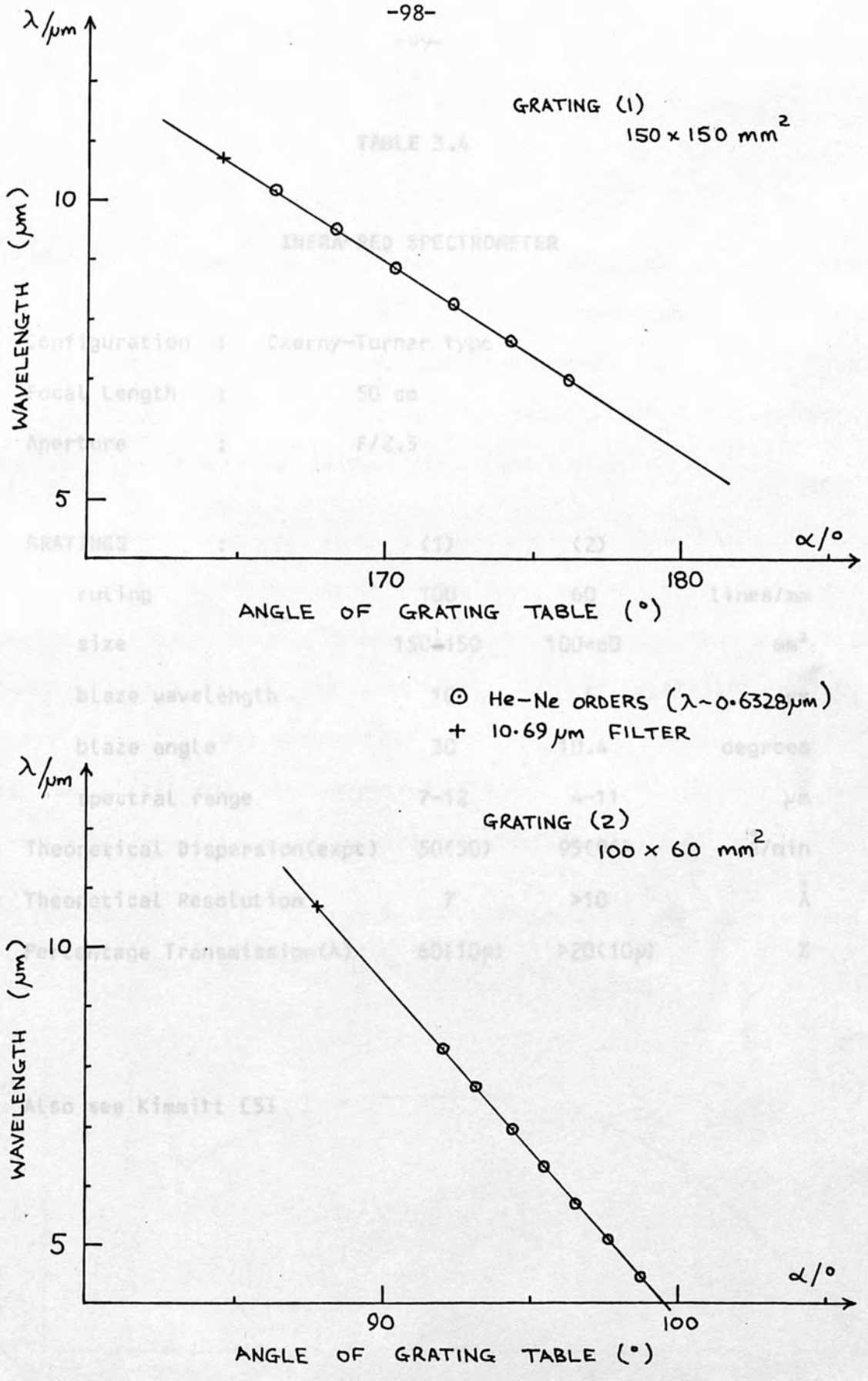

FIGURE 3.20 : Grating calibration plots.

TABLE 3.4

INFRA-RED SPECTROMETER

Configuration :	Czerny-Turner type		
Focal Length :	50 cm		
Aperture :	F/2.5		
GRATINGS :	(1)	(2)	
ruling	100	60	lines/mm
size	150*150	100*60	mm^2
blaze wavelength	10	6	μm
blaze angle	30	10.4	degrees
spectral range	7-12	4-11	μm
Theoretical Dispersion(expt)	50(50)	95(96)	Å/min
Theoretical Resolution	7	>10	Å
Percentage Transmission(λ)	60(10μ)	>20(10μ)	%

Also see Kimmitt [5].

3.3.3 DETECTORS

AU-GE DETECTOR :

The detector of prime importance in this study was the gold-doped germanium (Au-Ge) which was used for the spectral analysis of the scattered radiation. The detector was the Barnes A-200 series type fitted with an Irtran II (Calcium Fluoride) window. The spectral response of Au-Ge detector is shown in Figure 3.21.

The detector was mounted in a copper cylinder (see Fig. 3.22) to shield it from r.f. noise from the spark gaps. Due to the design of the detector and dewar vessel it was not possible to have the sensitive element directly behind the exit slits of the spectrometer. Thus instead a mirror, lens combination was employed to refocus the image from the slits onto the detecting element (Fig. 3.22). The bias circuitary schematic for the detector is shown in Fig. 3.23

The characteristics of the Au-Ge detector along with others used in this study have been outlined in Table 3.5.

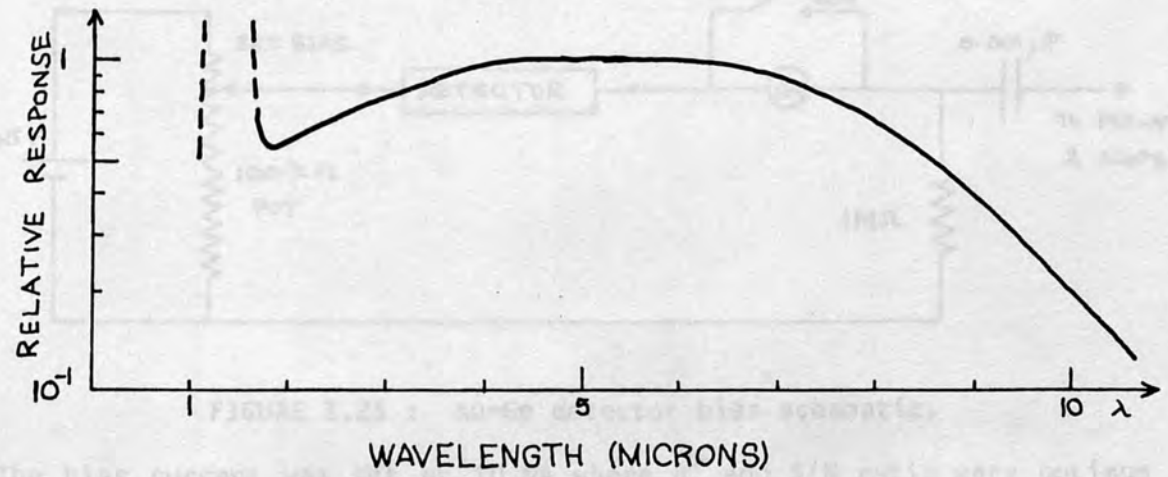

FIGURE 3.21 : Spectral response of Au-Ge detector.

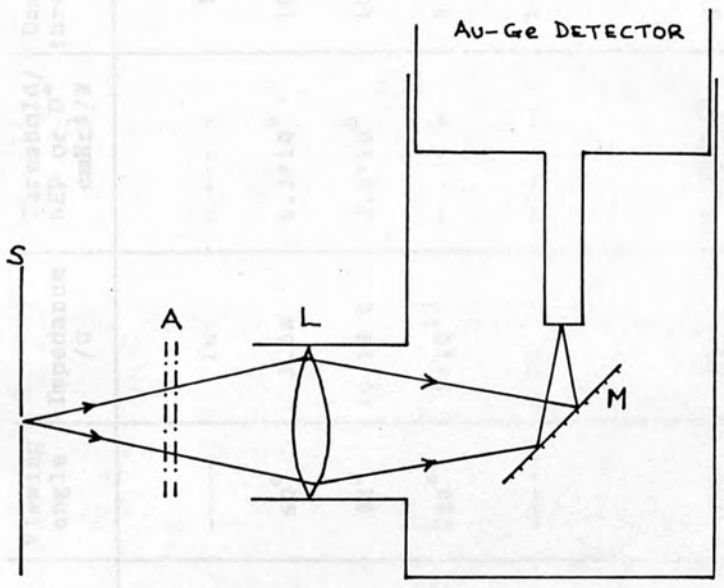

L – SALT (KCl) LENS (F2.5, f~5cm)

A – ATTENUATORS

S – SPECTROMETER SLITS

M – MIRROR

FIGURE 3.22 : Au-Ge detector mount and optics.

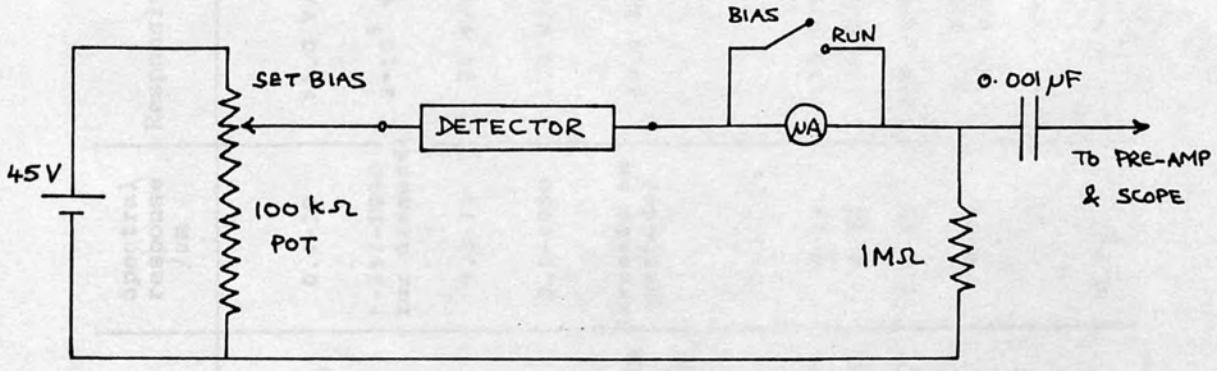

FIGURE 3.23 : Au-Ge detector bias schematic.

The bias current was set at 10 μA where D^* and S/N ratio were optimum for an infrared Globar source at 10^3 K modulated at a few kHz.

TYPE	Spectral response /μm	Responsivity	Response time.	Size	Temperature	Viewing angle	Impedance /Ω	Threshold/ NEP or D* $cmHz^{\frac{1}{2}}/W$	Damage threshold
THERMAL									
Calorimeter Gentec ED-500	0.4-30	>1.0 V/J	10 msec	4.8 cm (sq.)	ambient	-----	1M	- - - -	12 J
Golay	1-25(-1000 for diamond)	$2*10^5$ V/W	>30 msec	3 mm diam.	ambient	60°	3.5K	$6.3*10^9$	10^{-5}W
Thermopile TP 201	0.2-35	20 V/W	60 msec	2 mm (sq.)	ambient	95°	10-18 K	$2.0*10^8$	100mWcm^{-2}
Pyroelectric Eltec 420	0.1-1000	1.3 V/W	<1 nsec	2.5 mm (sq)	ambient	120°	$5*10^{12}$	- - - -	5 Wcm^{-2}
PHOTOMULTIPLIER	(depends on cathode)	<0.1 A/W	15 nsec	20 mm diam.	ambient	-----	50	- - - -	1 mJ
SEMICONDUCTOR									
GERMANIUM									
Photon-drag (a) Rofin 7411	4-22	.19 V/MW	<1 nsec	4 mm (sq.)	ambient	-----	50	NL thresh. 2.4 MW	8 MW
(b) Rofin 7415	4-22	.16 V/MW	600 psec 2 nsec(amp)	8 mm	ambient	-----	50	$4.5*10^{-3}$(NEP)	25 MW
Gold-doped	1.5-11	250 μV/W	<10 nsec	2 mm (sq.)	77°K	120°	1M bias 10μA	10^{10}	5 W
Lead-Tin Telluride	8-14	3.3 A/W 150 V/W	50 nsec	$3*10^{-3}$ cm^2	77°K	120°	>88	$2*10^{10}$	- - -
SILICON									
Pin-diode (biased 90 V)	0.2-1	- - - -	<5 nsec		ambient	-----	50	- - - -	- - -

TABLE 3.5 : DETECTORS

3.3.4 INTERACTION CHAMBER

TARGET CHAMBER :

A schematic of the interaction chamber is shown in Fig. 3.24. The internal diameter of the chamber is approximately 30 cm and has eight centrally spaced ports ('A' to 'H') of diameter 75 mm with one smaller port (diam. 50 mm) for rotary and diffusion pumps. The chamber could be evacuated down to $<10^{-3}$ torr in ~15 minutes, at which most experiments were performed. Often most ports were in use, e.g. 'A' for ruby input, 'G' for CO_2 input, 'H' for Thomson scattering, 'D' and 'E' for viewing and beam dumps, 'C' for alignment, 'F' for X-ray analysis leaving 'B' free for BNC connectors and viewing. Figure 3.25 shows a photograph of the target chamber.

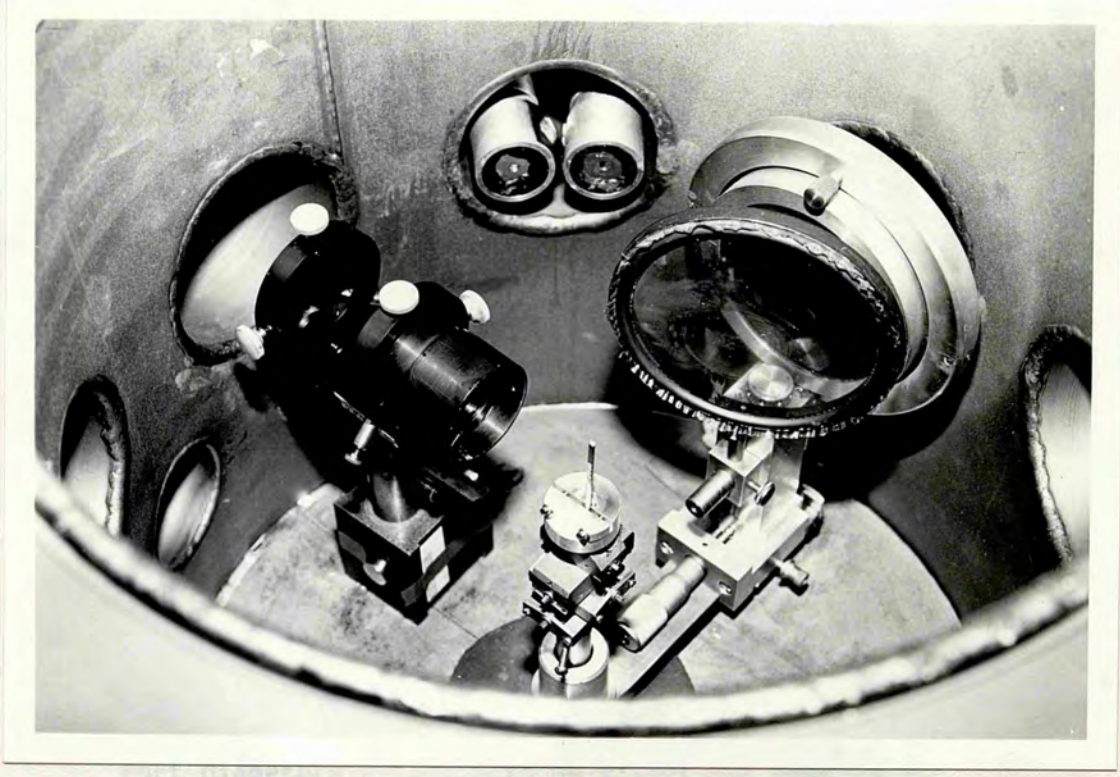

FIGURE 3.25 : Photograph of the target chamber.

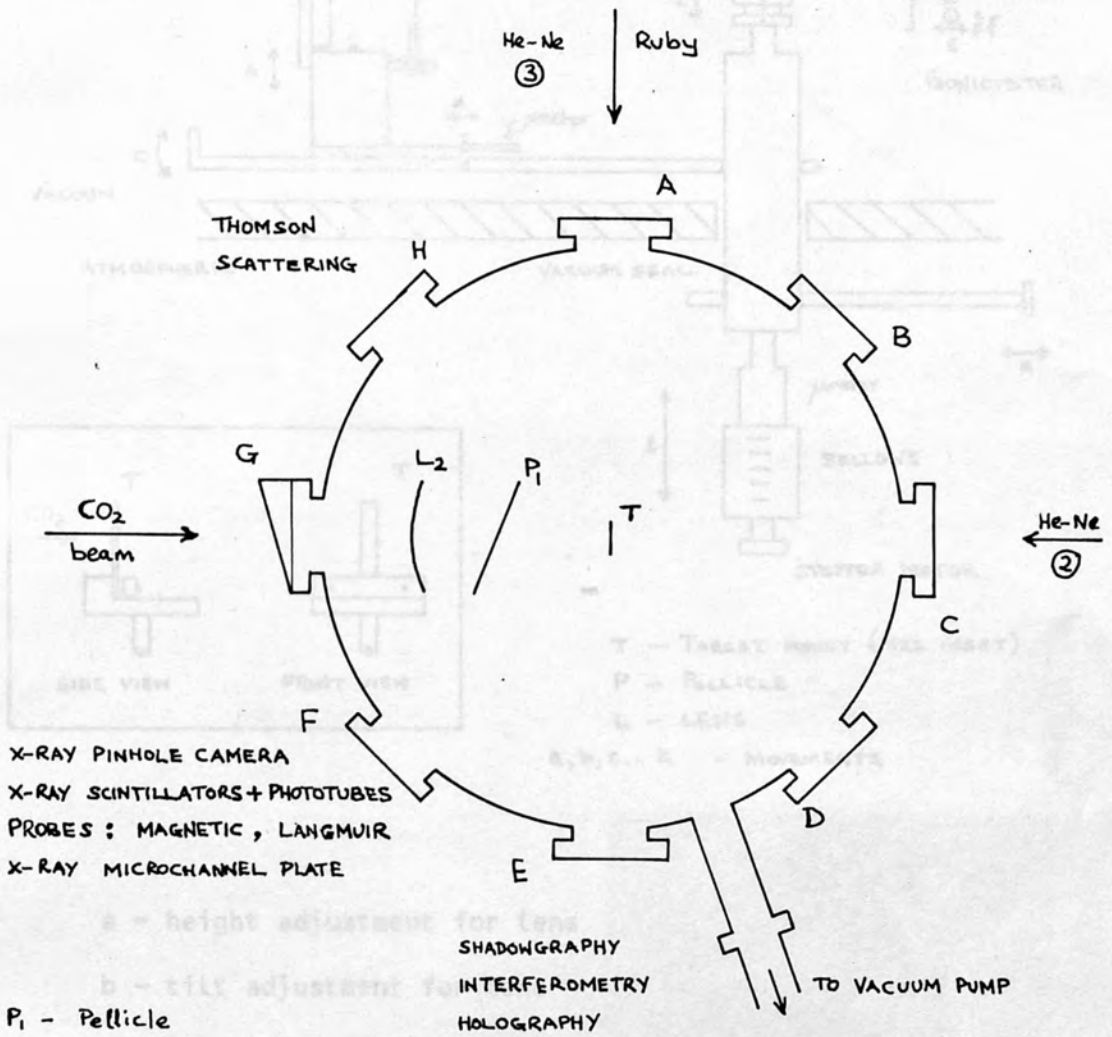

Internal diameter : 32 mm

External diameter : 42 mm

Port diameters : 75 mm except for pump(50 mm)

Number of ports : 8 +1 for vacuum pump.

FIGURE 3.24 : INTERACTION CHAMBER.

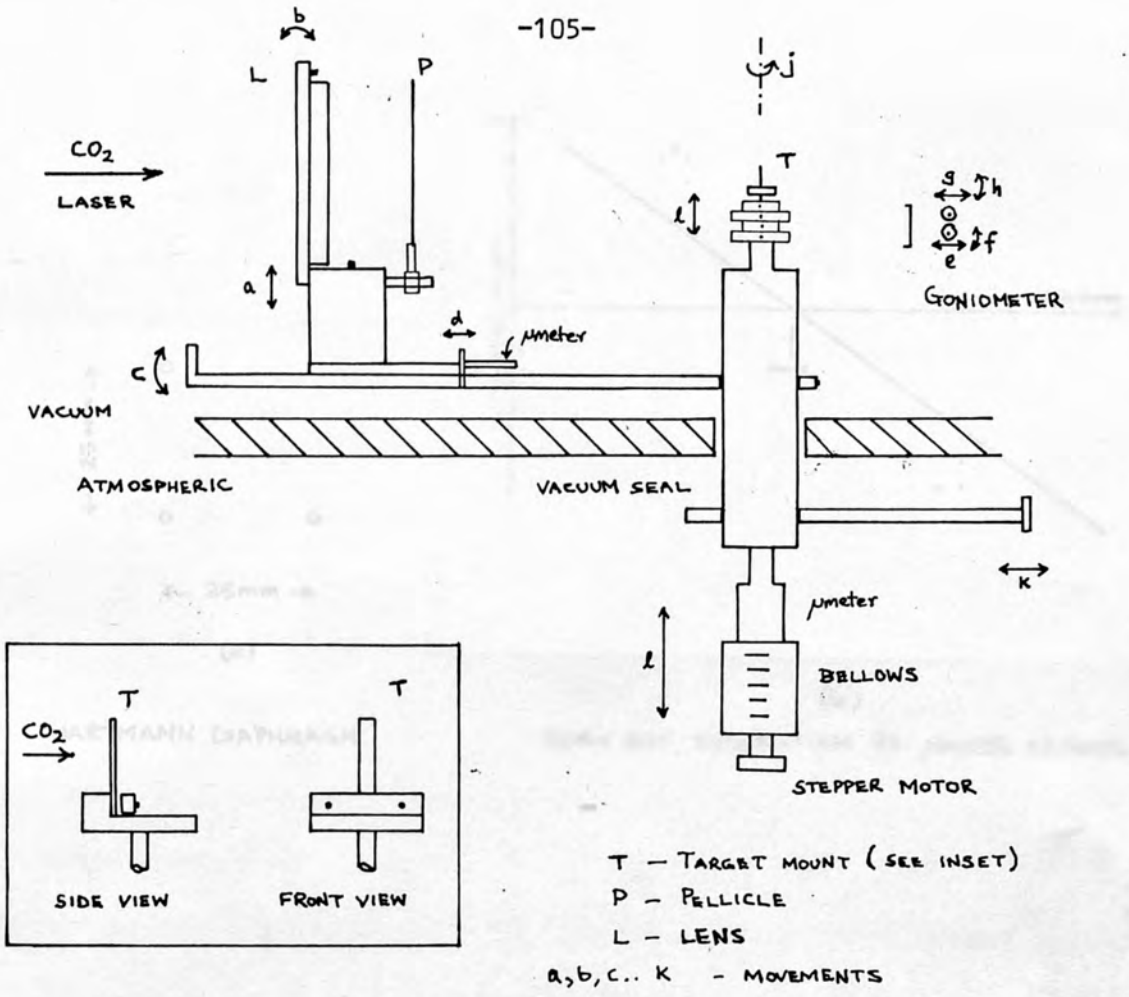

a - height adjustment for lens

b - tilt adjustment for lens

c - rotational adjustment for lens mount

d - translational adjustment for lens mount

e,f,g,h - goniometer adjustments along and perpendicular to CO_2 laser axis

j - rotational adjustment of target

k - translational adjustment along CO_2 laser axis of joint target/lens assembly

l - height adjustment of target

FIGURE 3.26 : Lens and target mount.

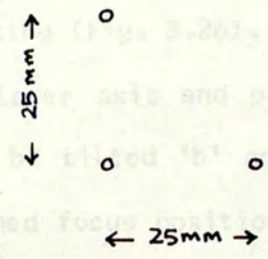

(a)

HARTMANN DIAPHRAGM

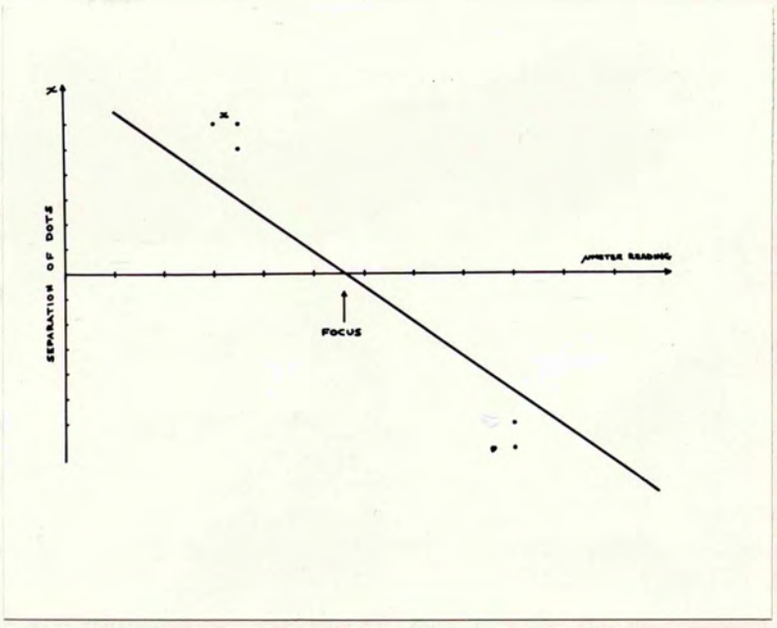

(b)

BURN DOT SEPARATION VS. μMETER READING

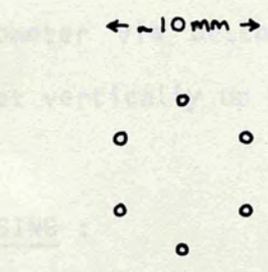

(c)

HEXAGONAL MASK

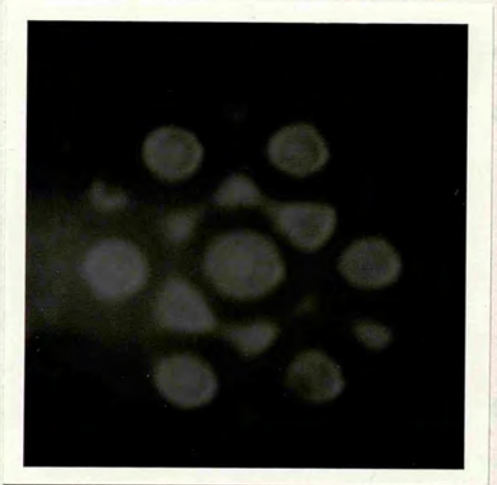

(d)

DIFFRACTION PATTERN OF MASK (c)

FIGURE 3.27 : Determination of focus of germanium meniscus lens

LENS AND TARGET MOUNTS :

The lens and target mounts were rigidly attached together though it was possible to make small adjustments on either. The lens mount had a coarse and a fine translational adjustment 'd' to enable accurate focusing (Fig. 3.26). The lens was mounted approximately central to the CO_2 laser axis and precisely using the fine adjustment 'a'. It could also be tilted 'b' and rotated 'c' around target axis ensuring a well defined focus position. In order to protect the lens from target debri a pellicle, P, was placed at an angle in between, using a protruded bar from the lens mount.

Once the lens was focused onto the target (see later) the connected target-lens assembly could be moved along laser axis 'k' without affecting the focus. A goniometer allowed for accurate target positioning on other axes (e,f,g,h), and the target holder (see inset) could be rotated about its axis (j). A stepper motor attached to a micrometer via bellows (Fig. 3.26) allowed remote movements of the target vertically up or down (l).

FOCUSING :

The lens focus was determined using a Hartmann diaphragm, consisting of three holes (~1 mm diam.) in an aluminium plate [Fig. 3.27(a)]. With the lens micrometer set in midrange and using the coarse adjustment an approximate lens focus position was obtained. The lens was then secured and micrometer moved to one extreme. A burn pattern on exposed Polaroid was then taken with the chamber at $p<10^{-2}$ torr. Another burn pattern was taken with the micrometer at the other extreme. By measuring the separation, x, of the burn dots for the corresponding micrometer values, it was possible to accurately

determine the focus from the plot of x versus micrometer reading [Fig. 3.27(b)]. The micrometer was then set to the determined value and the focus checked using a hexagonal mask [Fig. 3.27(c)] which gave a symmetrical diffraction pattern as shown in Fig. 3.27(d). The focus position was checked regularly, especially before any experimental run. Also it was ensured that the CO_2 laser focused onto the same spot as He-Ne laser ② in Fig. 3.18 by making fine adjustments to either the tilt, height or rotation of the lens. Figure 3.28 shows the quality of focus using a heavily attenuated CO_2 laser beam. The burn pattern being, once again, on exposed Polaroid film.

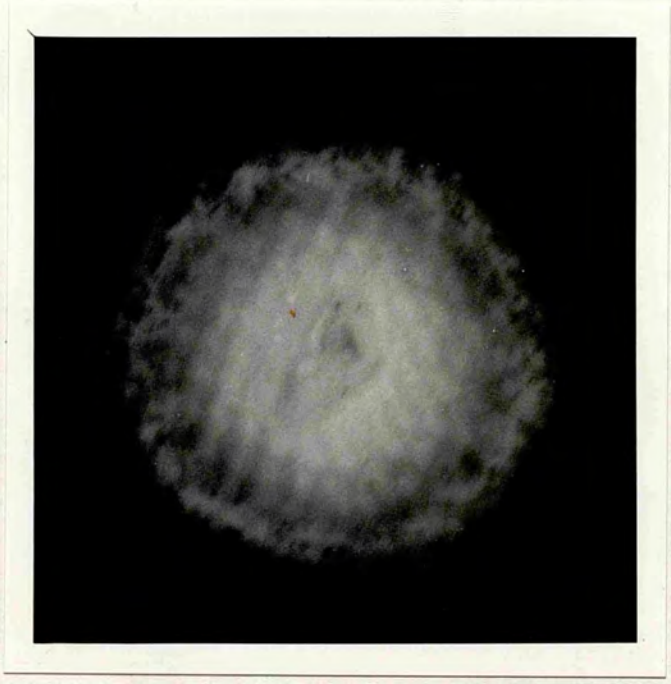

FIGURE 3.28 : Photograph of focus with heavily attenuated CO_2 beam.

3.3.5 OPTICAL DIAGNOSTICS

The optical arrangement used to probe the CO_2 generated plasmas is shown in Fig. 3.29. The synchronisation of the two laser systems was achieved using a coil pick-up signal, from the CO_2 laser discharge, which then triggered the ruby Pockell cell after an appropriate delay (see Fig. 3.24), as discussed earlier in §3.2.4. It was also possible to clip the ruby pulse further to obtain ruby pulses of shorter duration, using another Pockell cell, a pair of Glan-prisms and a laser triggered spark gap [9].

As indicated on the Figure, a similar set-up was used to obtain shadowgrams of the plasma. A narrow band ruby filter (λ_o=0.6943 μm, $\Delta\lambda$~10Å) was necessary to prevent 'fogging' of the photographic film due to plasma light. Also spatial filtering was necessary for a uniform beam profile.

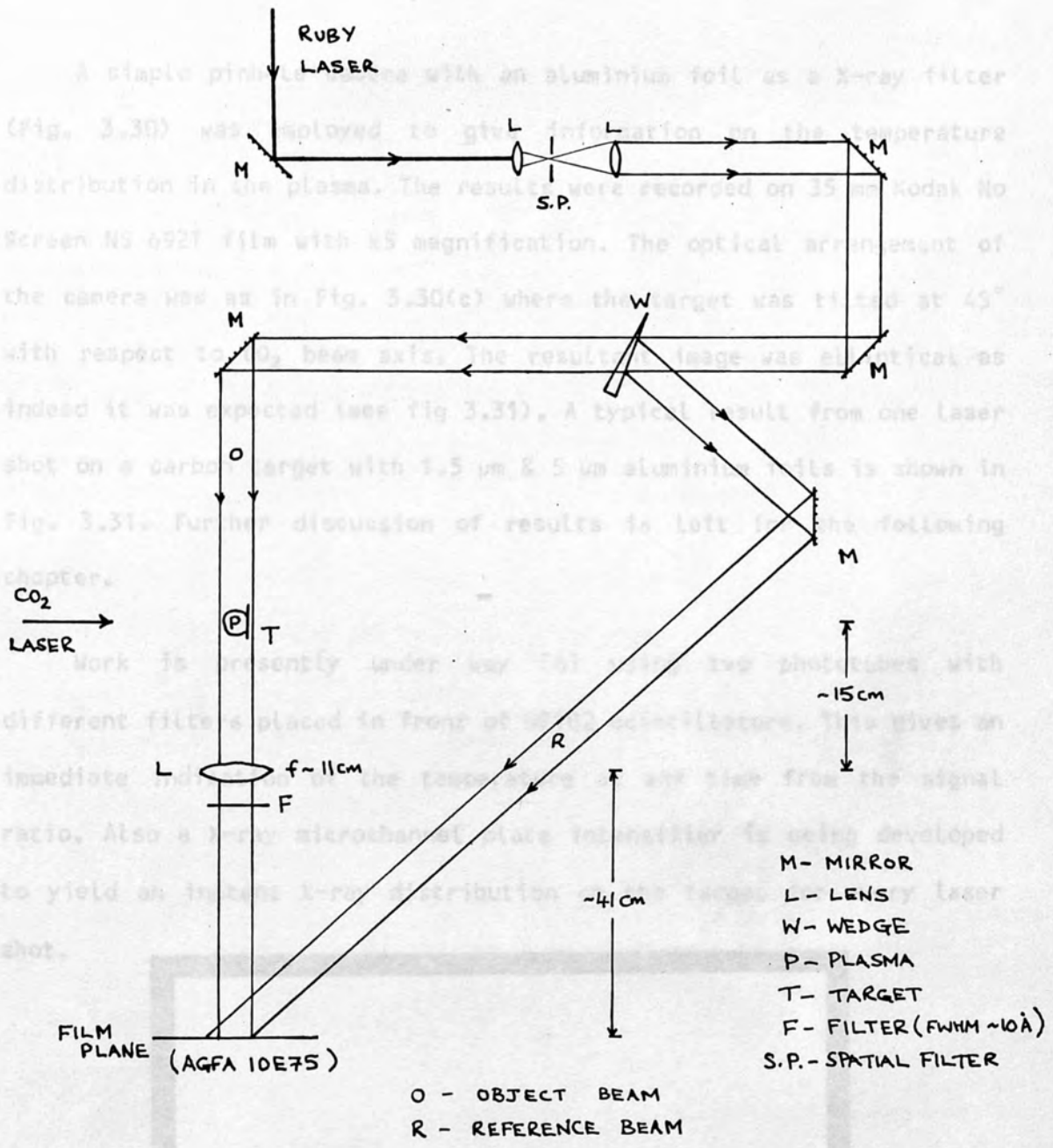

[For shadowgrams, as above but without reference beam.

Focused shadowgrams with lens L and unfocused shadowgrams without lens and with film plane ~25 cm from plasma.]

FIGURE 3.29 : Set-up for holographic interferometry.

3.3.6 X-RAY DIAGNOSTICS

A simple pinhole camera with an aluminium foil as a X-ray filter (Fig. 3.30) was employed to give information on the temperature distribution in the plasma. The results were recorded on 35 mm Kodak No Screen NS 692T film with x5 magnification. The optical arrangement of the camera was as in Fig. 3.30(c) where the target was tilted at 45° with respect to CO_2 beam axis. The resultant image was elliptical as indeed it was expected (see fig 3.31). A typical result from one laser shot on a carbon target with 1.5 μm & 5 μm aluminium foils is shown in Fig. 3.31. Further discussion of results is left for the following chapter.

Work is presently under way [6] using two phototubes with different filters placed in front of NE102 scintillators. This gives an immediate indication of the temperature at any time from the signal ratio. Also a X-ray microchannel plate intensifier is being developed to yield an instant X-ray distribution on the target for every laser shot.

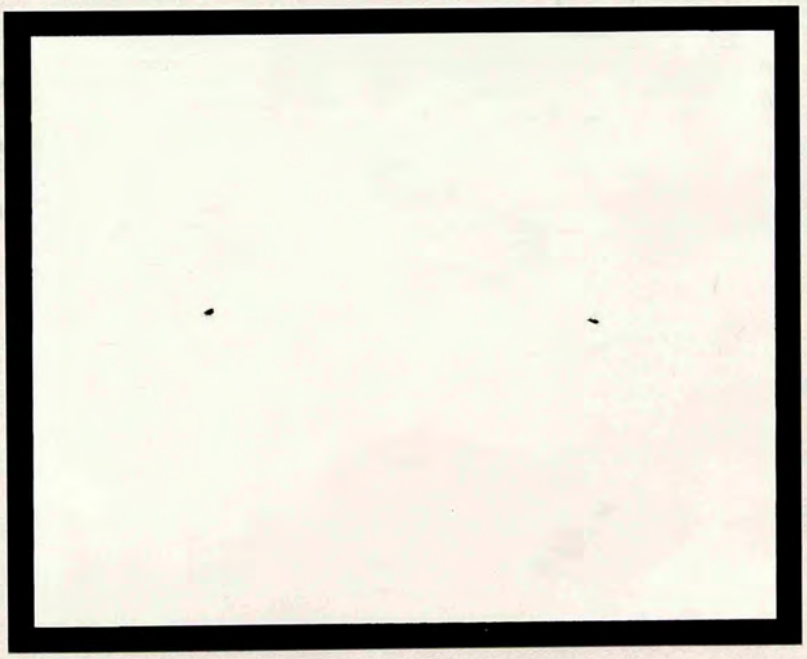

FIGURE 3.31 : Typical x-ray result.

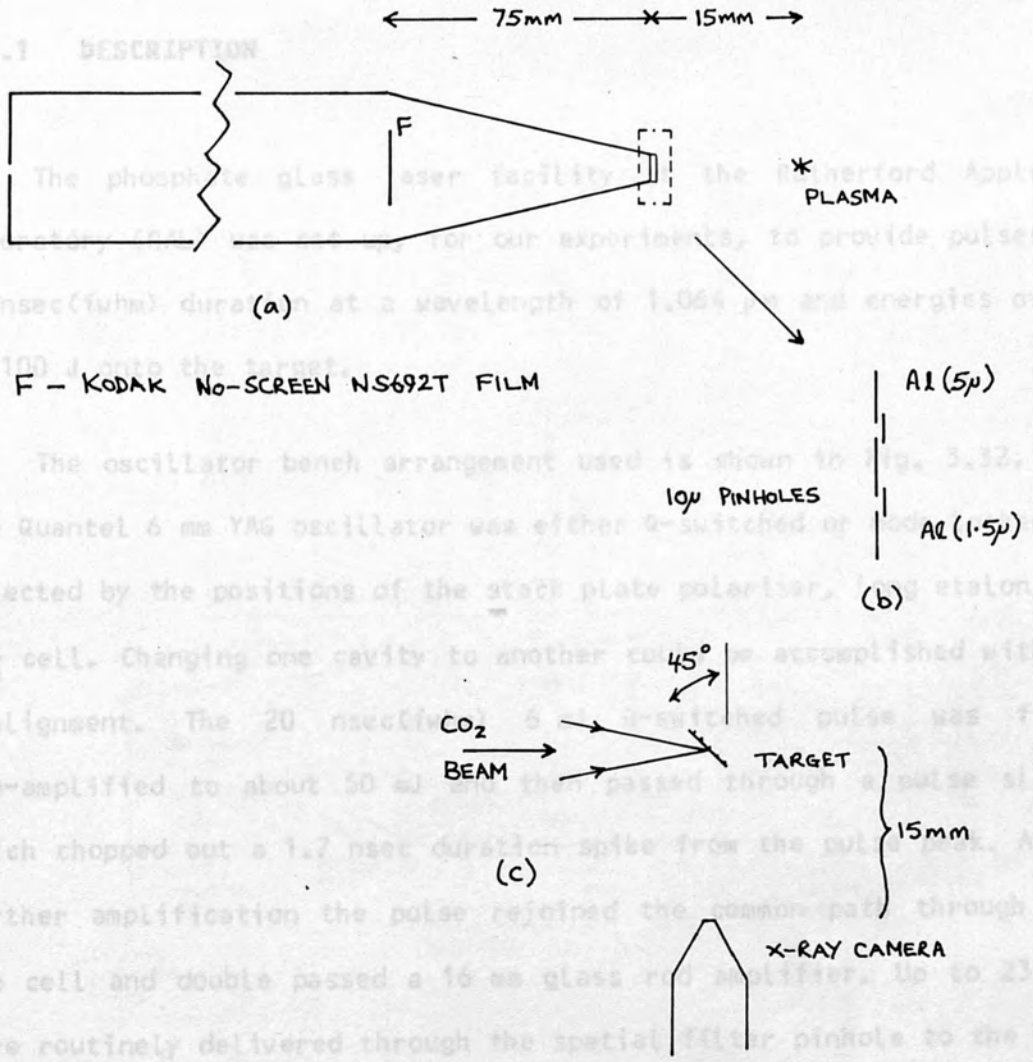

(a) Camera

(b) Pinholes

(c) Set-up

N.B: Not to scale

FIGURE 3.30 : X-ray pinhole camera.

3.4 NEODYMIUM-GLASS LASER

3.4.1 DESCRIPTION

The phosphate glass laser facility at the Rutherford Appleton Laboratory (RAL) was set up, for our experiments, to provide pulses of 1.7nsec(fwhm) duration at a wavelength of 1.064 μm and energies of up to 100 J onto the target.

The oscillator bench arrangement used is shown in Fig. 3.32. The one Quantel 6 mm YAG oscillator was either Q-switched or mode locked as selected by the positions of the stack plate polariser, long etalon and dye cell. Changing one cavity to another could be accomplished without realignment. The 20 nsec(fwhm) 6 mJ Q-switched pulse was first pre-amplified to about 50 mJ and then passed through a pulse slicer which chopped out a 1.7 nsec duration spike from the pulse peak. After further amplification the pulse rejoined the common path through the dye cell and double passed a 16 mm glass rod amplifier. Up to 230 mJ were routinely delivered through the spatial filter pinhole to the main amplifier chain (see Fig. 3.33). The prepulse, caused by the leakage of the remainder of the Q-switched pulse was very low, being 10^{-4} in power after the pulse slicer, 10^{-6} after the oscillator bench dye cell, and 10^{-7} after the amplifier chain dye cell.

The oscillator was passively Q-switched and constrained to a single longitudinal mode at 1.064 μm output by a resonant output reflector. A spatially and temporally smooth pulse was produced, with less than a 1% failure rate of modulated pulses.

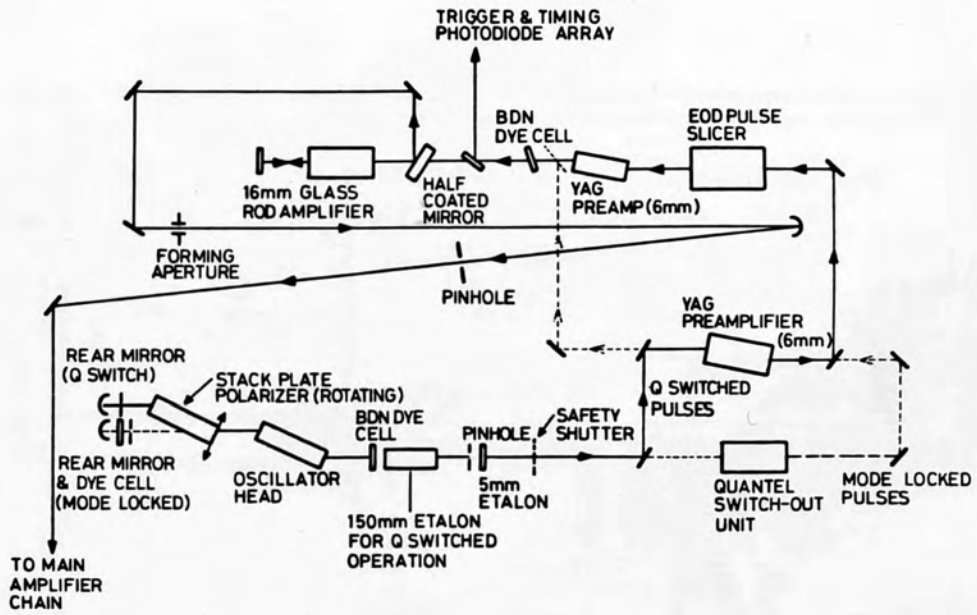

FIGURE 3.32 : Oscillator bench arrangement

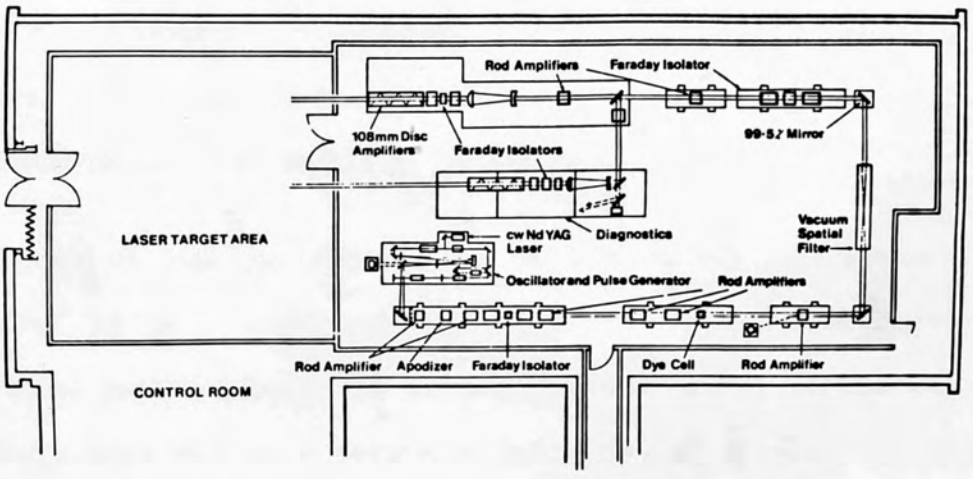

FIGURE 3.33 : Glass laser installation

The pulse selector consisted of a pair of Pockell cells, driven by a laser-triggered spark gap, between Glan-Taylor prisms.

The laser output could be frequency doubled to 0.53 μm by means of a KDP crystal with >50% efficiency.

3.4.2 TARGET AREA

The target area used in the experiments could accomodate either single beam interaction experiments or two beams for compression experiments. Here, however, it was fed with a single full-aperture beam from a double-passed disc amplifier in the laser room.

The layout of high power beams can be seen in the overall optical layout later in this chapter (Fig. 3.36). The arrangement used to generate local expanded beams for target alignment and focusing, and to compare these with the laser area's cw YAG alignment beam is indicated in Fig. 3.34. A single spatial filter was used for all beams. The main collimating lens, an F/5 air spaced doublet was designed by the laser division at RAL. Local and distant beams were combined on the 90% reflecting splitter (removed during laser shots) and compared on a telemicroscope TV3 having an angular definition of a few micro-radians. The overall stability of the mirror-tower system which brought the beam from the laser area, 30 meters away, to TAII was good (see sketch in Fig. 3.35).

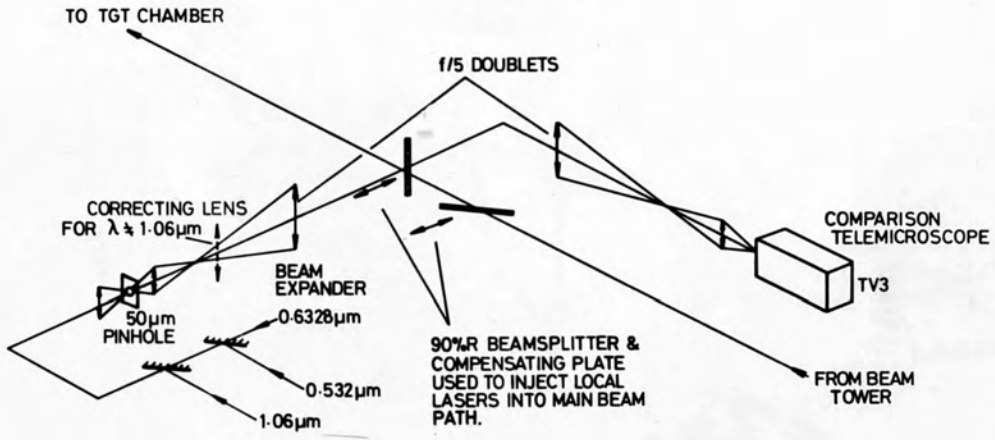

FIGURE 3.34 : Local lasers in TAII

The use of locally produced beams for most alignment and focusing operations allowed work to proceed in the target area while the main laser was being adjusted. The laser area beam was checked against the local beam before each shot and brought into colinearity by adjusting a pair of mirrors. However, if no realignment had been made elsewhere in the laser it was usually not necessary to make any corrections.

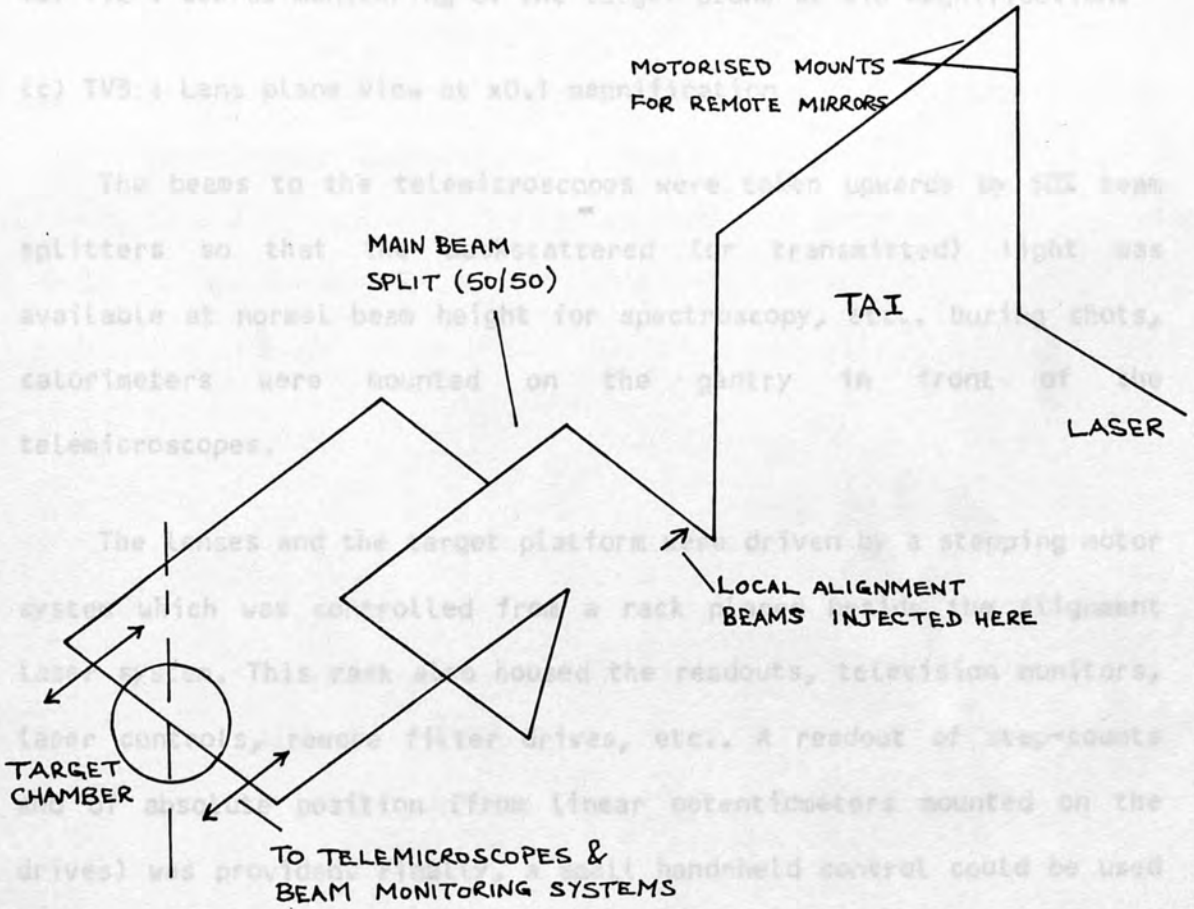

Figure 3.35 : Layout of high power beams in target area.

The target focusing and alignment telemicroscopes were mounted on a gantry above the target chamber as shown in Fig. 3.35(for two beams), making the floorspace available for experiments. The telemicroscope system operated in three modes:-

(a) TV1 : Fine monitoring of the target plane at a magnification of 400x.

(b) TV2 : Coarse monitoring of the target plane at x10 magnification.

(c) TV3 : Lens plane view at x0.1 magnification

The beams to the telemicroscopes were taken upwards by 50% beam splitters so that the backscattered (or transmitted) light was available at normal beam height for spectroscopy, etc.. During shots, calorimeters were mounted on the gantry in front of the telemicroscopes.

The lenses and the target platform were driven by a stepping motor system which was controlled from a rack placed beside the alignment laser system. This rack also housed the readouts, television monitors, laser controls, remote filter drives, etc.. A readout of step-counts and of absolute position (from linear potentiometers mounted on the drives) was provided. Finally, a small hand-held control could be used anywhere in the room to make remote lens or target adjustments in order to facilitate setting up of diagnostic apparatus. Ease and sensitivity of control, reproducibility of position and backlash were all good.

3.5 EXPERIMENTAL PROCEDURE (ND SYSTEM)

Experiments were performed to see $2w_o$ specularly scattered and backscattered from various targets. Use of a spectrometer was called for, a Monospek type 500, details of which are outlined in Table 3.6.

3.5.1 OPTICAL LAYOUT

Initial alignment and calibration was done for the Spex (Monospek 500) spectrometer using a He-Ne laser, various UV lamps such as Cd/Hg/Zn and Argon lamps. The latter gave many spectral lines over the entire range of interest.

TABLE 3.6

SPEX 500 SPECTROMETER

Focal Length :		500 mm
Aperture :		F/5
Grating : ruling		1200 lines/mm
size		10 cm * 10 cm
blaze		0.5 μm
Dispersion :	15.5 Å/mm	at λ -4700 Å
Resolution :	0.05 Å	at λ -5000 Å

The optical arrangement as a whole is shown in Figure 3.36 and the various optical components are listed in Table 3.7. The optical set-up relevant for our experiment is set out in greater detail in Figure 3.37 with distances indicated in cm.

The diagram in Fig. 3.36 shows the Holgate calorimeters monitoring the incident and backscattered energies, streak camera ⓐ monitoring the temporal profile of the incident beam, whilst streak camera ⓑ in conjunction with a Monospek spectrometer and optical multichannel analyser (OMA) record the incident and backscattered spectrum around the incident frequency. Details of the optical components are given in Table 3.7 with a key. As can be seen, different mirrors have been used along different paths depending on what is being analysed, e.g. for $2w_o$ interested in rejecting as much infrared as possible, thus use of green biased mirrors.

The table presents the reflectivities (R) or transmissivity (T) of the various components at particular wavelengths with indications for anti-reflection (AR) coated optics and their angular orientation (e.g. 45°) to the beam path.

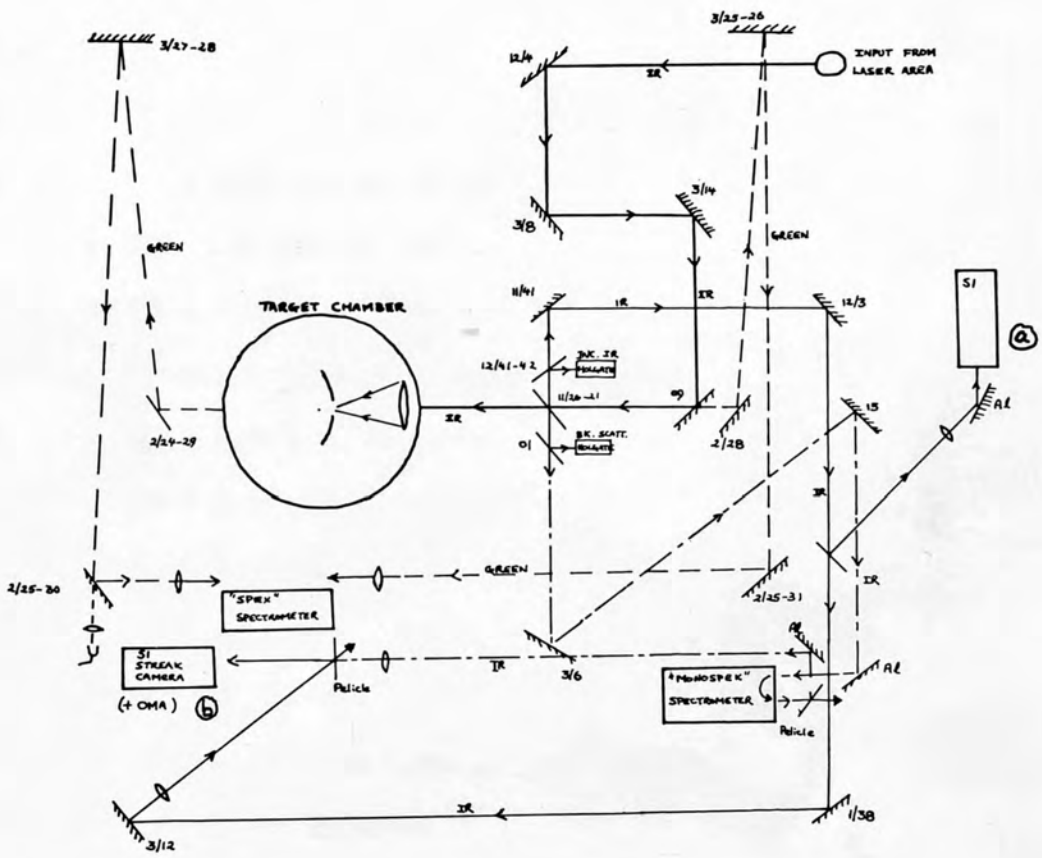

FIGURE 3.36 : Optical layout in TAII

TABLE 3.7

OPTICAL COMPONENTS

MIRRORS

01	:	50% R 1.06 μm @ 45°
1/38	:	HR @ 1.06 μm 45°-P
2/24-29	:	99% @ 0.53 μm, AR 45°-P
2/25-30	:	HR @ 0.53 μm, AR 45°-P
2/25-31	:	HR @ 0.53 μm, AR 45°-P
2/28	:	HR @ 0.53 μm, AR 45°-P
3/6	:	99% R @ 1.06 μm 25°-P
3/8	:	HR @ 1.06 μm 45°-P
3/12	:	HR 45 @ 1.06 μm (not AR coated)-P
3/14	:	HR @ 1.06 μm 45°-P
3/25-26	:	HR @ 0.53 μm 0° + AR
3/27-28	:	HR @ 0.53 μm 0° + AR
09	:	HR @ 1.06 μm 45°-P
11/41	:	96% R 45°-S
11/20-21	:	4% R @ 45°-S/AR 1.06 μm
12/3	:	1.06 μm HR 45°-P/AR
12/4	:	HR @ 1.06 μm 45°-P
12/41-42	:	50% AR 1.06 μm @ 45°
15	:	one side AR @ 0.6 μm, other R @ 0.71 μm & T @ 0.53 μm

The table presents the reflectivities,R (transmivities, T) of various components in Fig. 3.36 at particular wavelengths with indications for anti-relection (AR) coated optics and their orientation (e.g. 45°).

HR - Highly reflecting

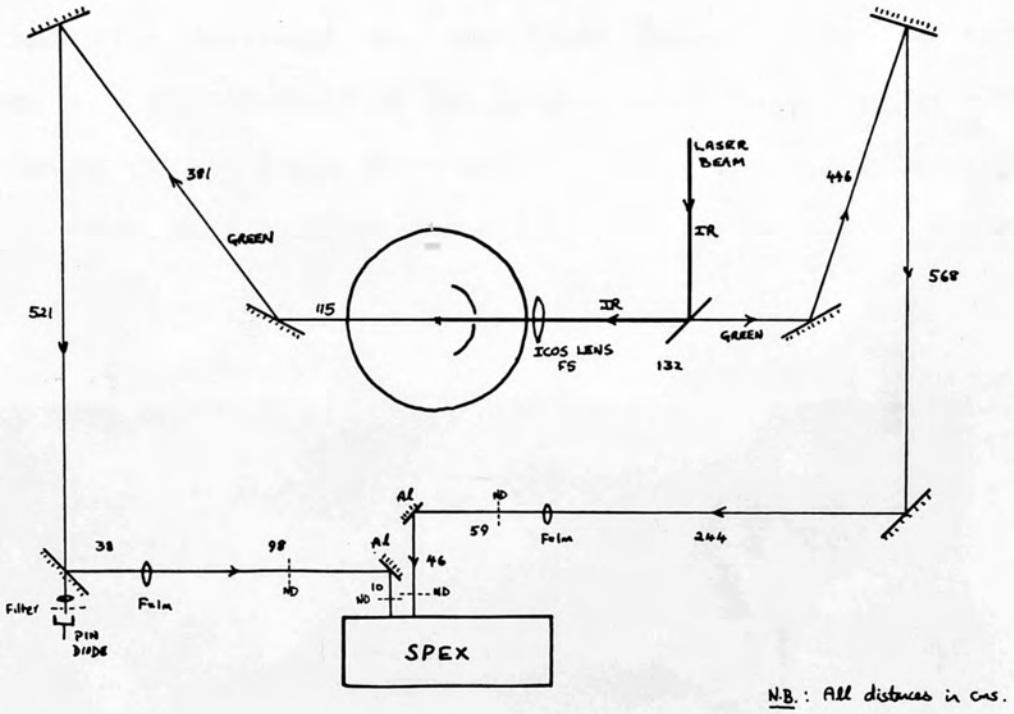

FIGURE 3.37 : Experimental set-up at RAL

Alignment of the various optical components was critical and had to be checked often. Initial alignment was made using the He-Ne laser. Basically the image of the paraboloid was focused onto the slits along with the light that passed back through the lens. In the latter case use of a pointer placed in front of the lens helped to achieve this. Here we used a parallel source of white light placed behind the target. The resulting focused image taken on Polaroid type 57 film, is shown in Figure 3.38. This shows that the top image is due to the lens (note the pointer used for focusing) and the lower image is due to the paraboloid. More than one-half of the paraboloid was imaged and it was verified to be the top half. Once again alignment was double checked using a YAG laser. Details of the paraboloid used are outlined in Table 3.8 and Fig. 3.39.

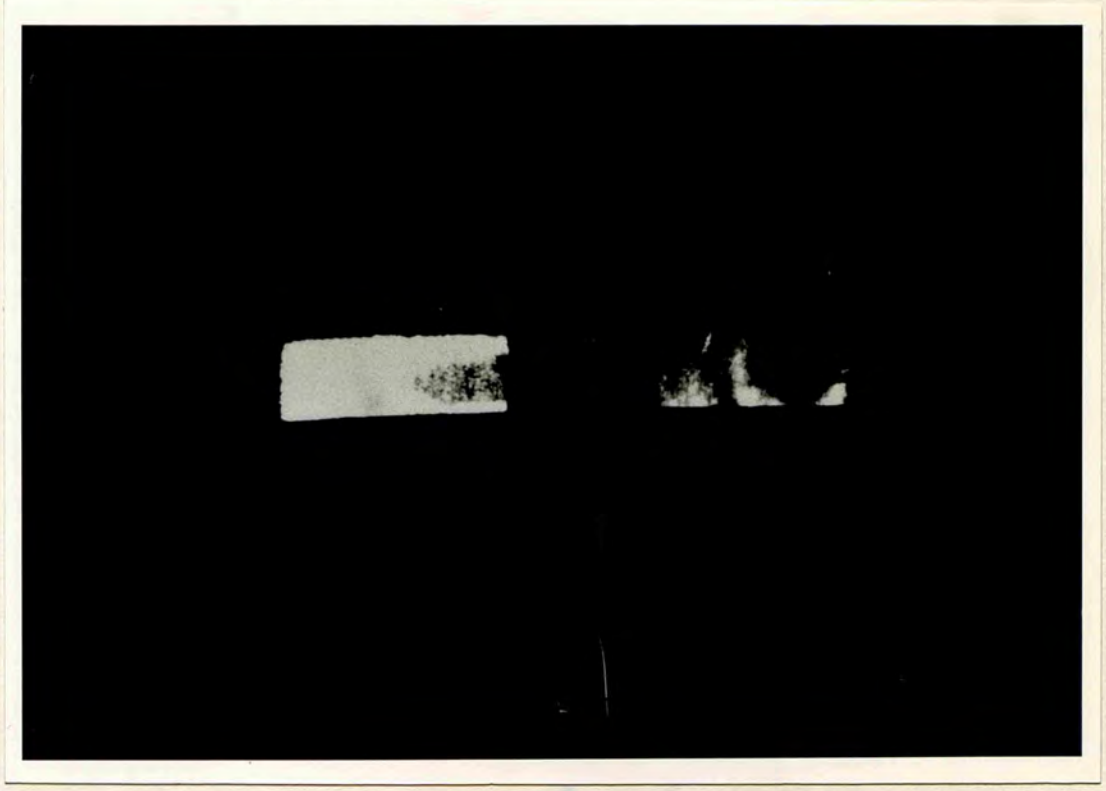

FIGURE 3.38 : Image of lens and paraboloid at back of Spex 500 spectrometer.

TABLE 3.8 : PARABOLOID

	II
Ref. No.	3P-152-64
F/mm	63.5
φ/mm	152
d/mm	23
h/mm	19
	f5(5.71°)
	62
Blur circle :	
quoted/mm	0.3
observed/mm	2
coating	$AlMgF_2$
Reflectivity :	
@ 1 μm	85% — 93%
@ 0.5 μm	76% — 90%

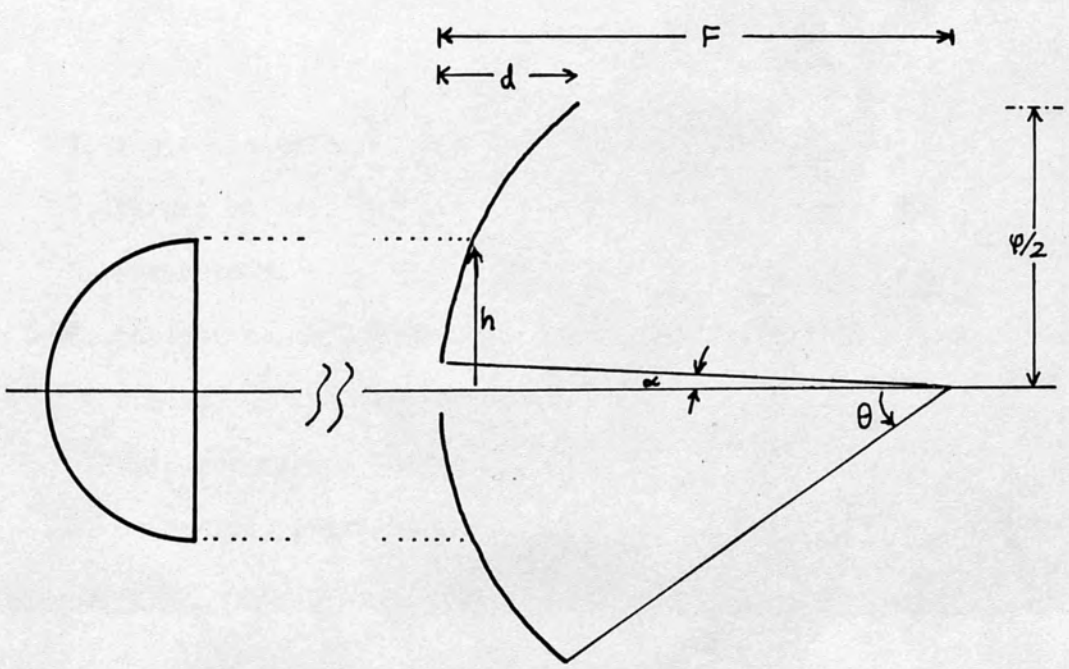

FIGURE 3.39 : Paraboloid parameters.

Before any target (**§3.5.2**) was irradiated by the main neodymium laser it was placed at the focus of the paraboloid and adjusted to be normal to the incoming beam using a He-Ne laser. The target was then placed at the focus of the F/5 laser lens, using a YAG laser, by moving the paraboloid-target assembly.

The laser radiation was typically focused to a spot-size of 100 μm and the specularly backscattered radiation, collected by the paraboloid, and backscatter collected by the lens were spectrally analysed. The spectrometer was set to look at the second harmonic radiation and consequently use of green mirrors was emphasised to reduce the effect from w_o to insignificance.

3.5.2 TARGETS

The set-up inside the target chamber is shown schematically in Fig. 3.40.

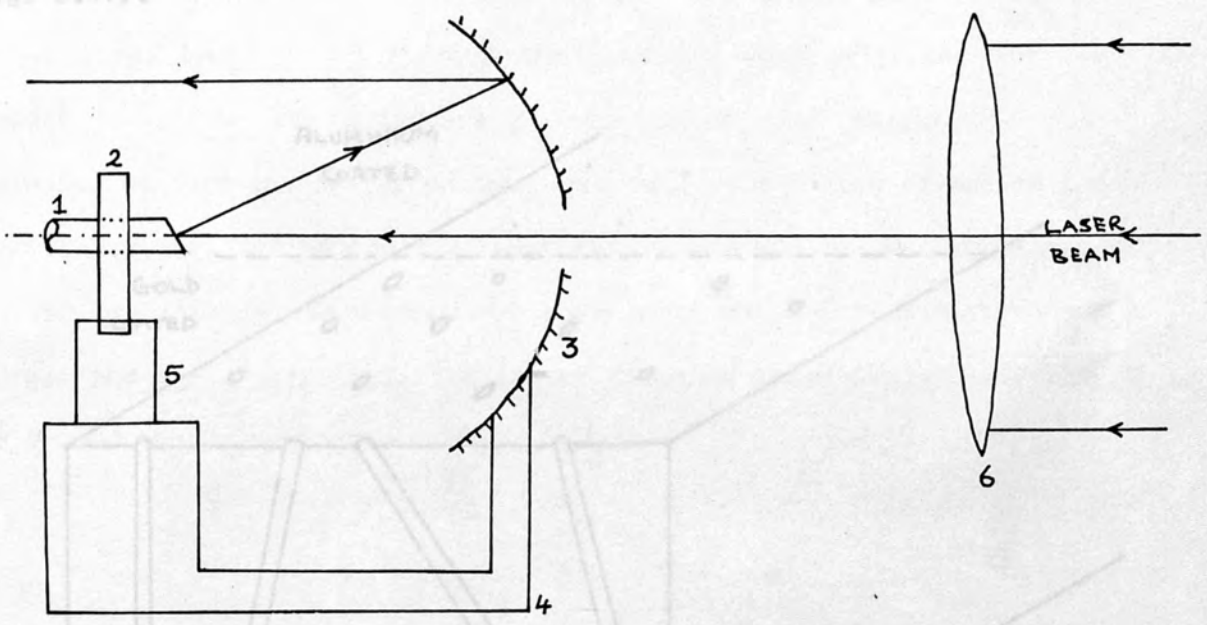

1. Angled targets.
2. Target holder.
3. Paraboloid.
4. Optical bench linking the mount, on which the paraboloid is placed, to the target holder.
5. Clip for target holder.
6. Laser focusing F/5 lens.

FIGURE 3.40 : Target set-up (exaggerated)

TARGET CONSTRUCTION :

Holes of diameter 1.5 mm were drilled into a solid metal block at various angles. These were then filled with stainless steel pins (the substrate). One of the metal block face was then grounded and polished flat before having gold and aluminium being evaporated onto it (see Fig. 3.41).

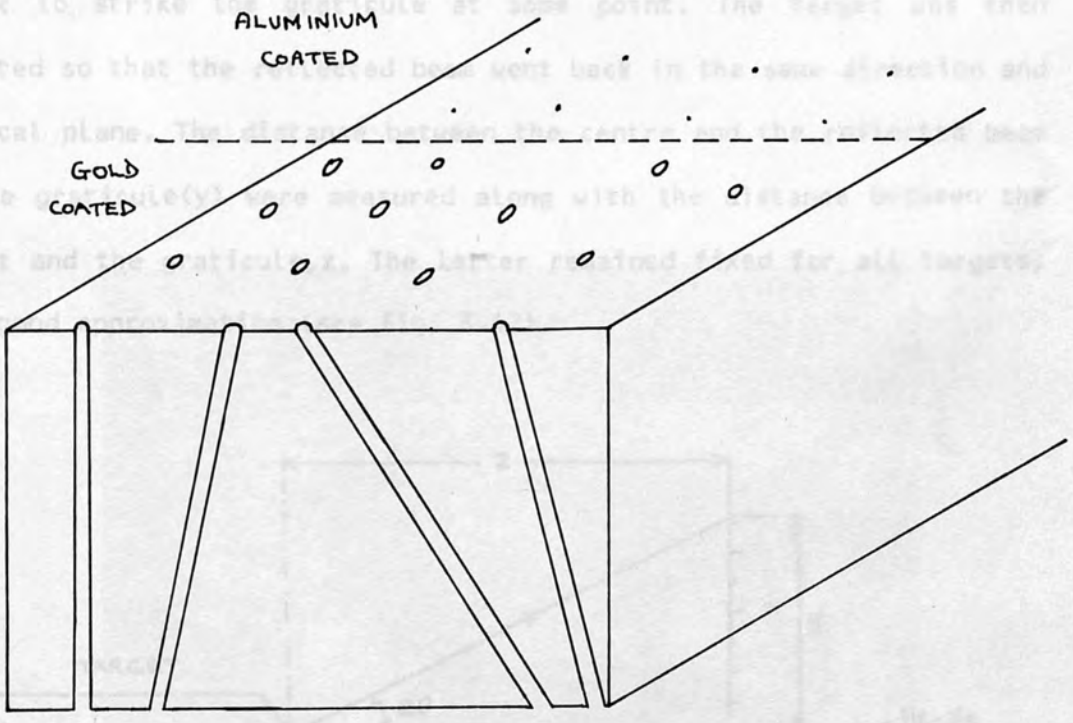

FIGURE 3.41 : Cross-section showing the metal block used for angled target construction.

The coated steel pins were then gently popped out. A listing of the targets is given in Table 3.9.

ANGLE OF TARGETS :

The angles of the various targets were calculated from the measurements made on the reflection of the He-Ne laser light from the targets when placed at the focus of the paraboloid. This was performed by using a graticule (basically a sheet of graph paper), with a small hole at its centre and placed directly in front of the paraboloid. The He-Ne laser beam passed through the hole and then reflected off the target to strike the graticule at some point. The target was then adjusted so that the reflected beam went back in the same direction and vertical plane. The distance between the centre and the reflected beam on the graticule(y) were measured along with the distance between the target and the graticule,z. The latter remained fixed for all targets, to a good approximation (see Fig. 3.42).

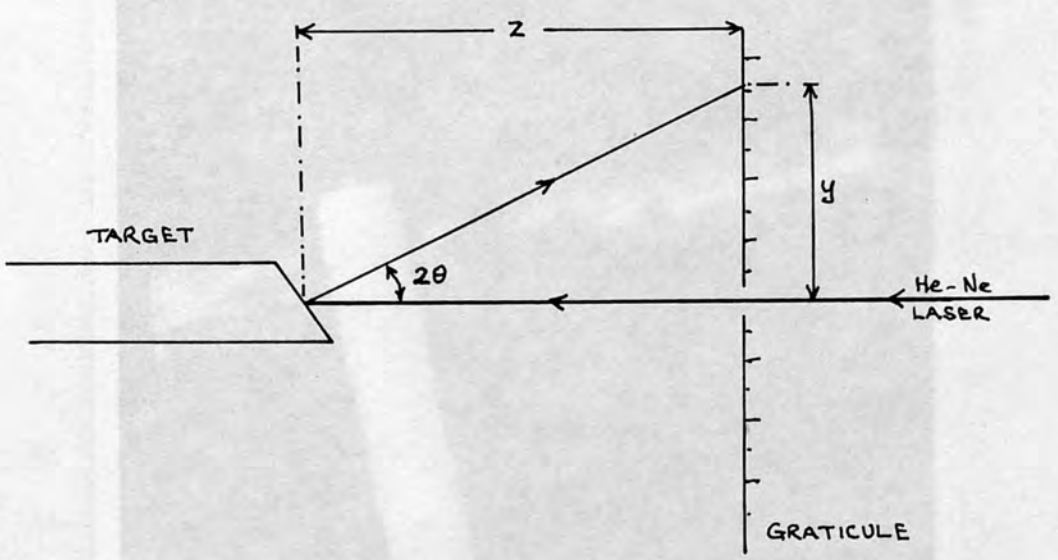

FIGURE 3.42 : Measurement of target angle.

From the Figure it follows that,

$$\tan 2\theta = y/z \qquad (3.1)$$

Thus we can determine the angle of target, θ . These measurements were

completed for all the targets at the beginning of the experiment. The targets were then labelled according to their distance y in mm, e.g. Al XXXIII .

The complete list of all the targets and the relevant measurements are presented here in Table 3.9. The Figure below shows a photograph of the target in its holder, the left end being angled and coated with either aluminium or gold. It is on this face that the laser radiation was focused.

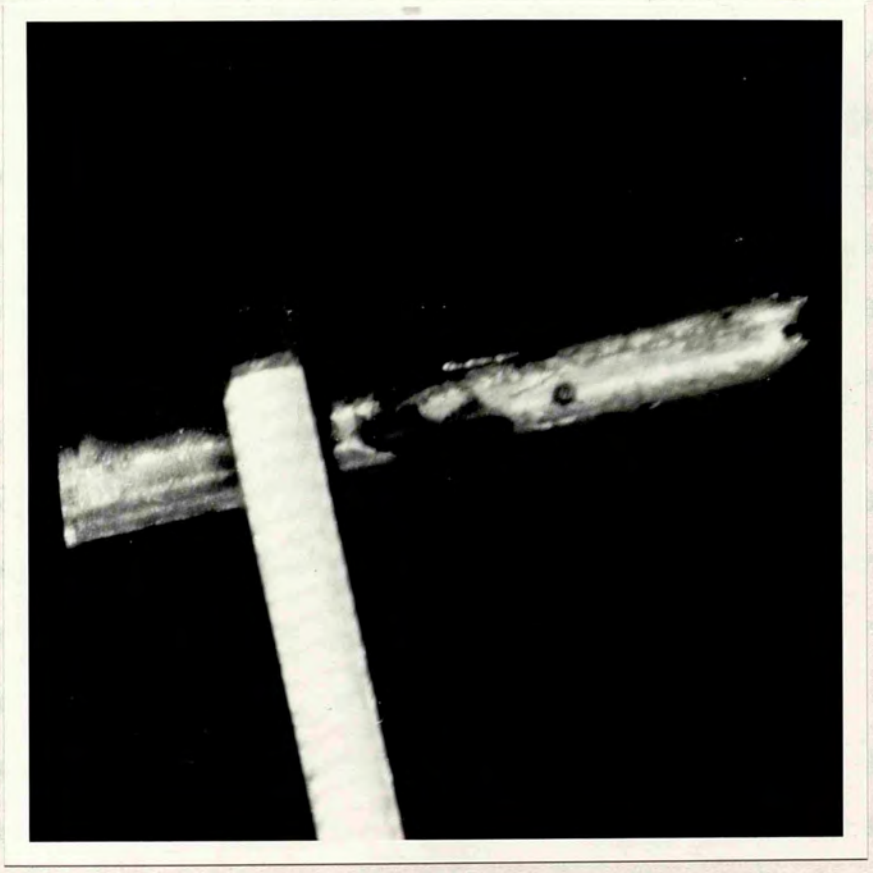

FIGURE 3.43 : Photograph of target in its holder.

TABLE 3.9 : TARGETS

TARGET	Y/mm	2θ/°	TARGET	Y/mm	2θ/°
Al I	2	2.9	Al XXVI	35	41.2
Al II	0	0	Al XXVII	35	41.2
Al III	15	20.5	Al XXVIII	51	51.9
Al IV	11	15.4	Al XXIX	40	45.0
Al V	12	16.7	Au XXXI	46	49.0
Al VI	13	18.0	Au XXXII	13	18.0
Al VII	19	25.4	Au XXXV	16	21.8
Al VIII	30	36.9	Au XXXVII	22	28.8
Al IX	0	0	Au XXXIX	33	39.5
Al X	0	0	Au XLI	24	31.0
Al XII	12	16.7	Au XLII	34	40.4
Al XIV	31	37.8	Au XLIII	28	35.0
Al XV	17	23.0	Au XLIV	32	38.7
Al XVII	20	26.6	Au XLVI	29	36.0
Al XVIII	10	14.0	Au XLVII	51	51.9
Al XIX	35	41.2	Au XLIX	45	48.4
Al XXI	24	31.0	Au LI	5	7.1
Al XXII	28	35.0	Au LII	5	7.1
Al XXIII	47	49.6	Au LIV	0	0
Al XXIV	47	49.6	Au LVII	45	48.4
Al XXV	33	39.5	Au LVIII	45	48.4

REFERENCES :

1. Abdel-Raouf,W.S. (1980) Ph.D. Thesis, Univ. of London

2. Born & Wolf (1970) "Optics" Pergamon Press (London) 4th Edition.

3. Fowles,G.R. (1975) "Introduction to Modern Optics" Holt,Rinchart & Winston Inc.(USA).

4. Hecht,E. & Zajac,A. (1974) "Optics" Addison-Wesley (USA)

5. Kimmitt,M.F. (1965) "A Far Infra-Red Spectrometer" RRE Technical Note 716

6. Marchington,P.M.(1983) Private Communication.

7. McMordie,J.A. Perkin,J.L. & Sentance,G.W. (1972) "Description & Operation of the N56 CO_2 Laser" U.K.A.E.A. AWRE Research Note No. 47/72.

8. O'Neill,F. (1976) "High Power Pulsed CO_2 Lasers" Rutherford Laboratory Report

9. Sudera,Y. (1983) Private Communication

CHAPTER FOUR

RESULTS & DISCUSSION

4.1 BACKSCATTER & SBS (CO_2 SYSTEM)

Reflectivity and Brillouin measurements at RHC were undertaken with a view to understanding the absorption properties of the plasma. This would then indicate the percentage of the incident energy reflected and also thereby give estimates of the plasma temperature in the underdense region. These would then prove to be useful for subsequent discussion on second harmonic and other diagnostics.

REFLECTIVITY :

Using apparatus described in the previous chapter (§3) carbon targets were irradiated by CO_2 radiation with the incident and reflected radiation being monitored by calorimeters(Gentec Model ED-500) and photon-drag detectors(Rofin type 7415). One calorimeter was placed in beam path 'd' to monitor the reflected energy, whilst the other, of similar type, was placed in beam 'e' for the incident energy(see Fig. 3.18). The temporal profile of the CO_2 laser was monitored by the photon-drag detector, in beam 'c', and this did not vary much, from shot to shot, to those shown earlier in Fig. 3.2.

After having corrected for the differences in calibration of the calorimeters, compensated for the absorption and reflection from the beam splitters and pellicles, values for the reflectivities were obtained. These have been plotted in figs. 4.1-4.2 for the case of planar carbon targets when irradiated at different incident intensities for several target angles. Each data point represents a mean of five or more results. Figures 4.1(a)&(b) indicate the backscattered intensity, I_B, to vary linearly with the incident intensity I_o as

$$I_B \propto 0.1 * I_o \qquad (4.1)$$

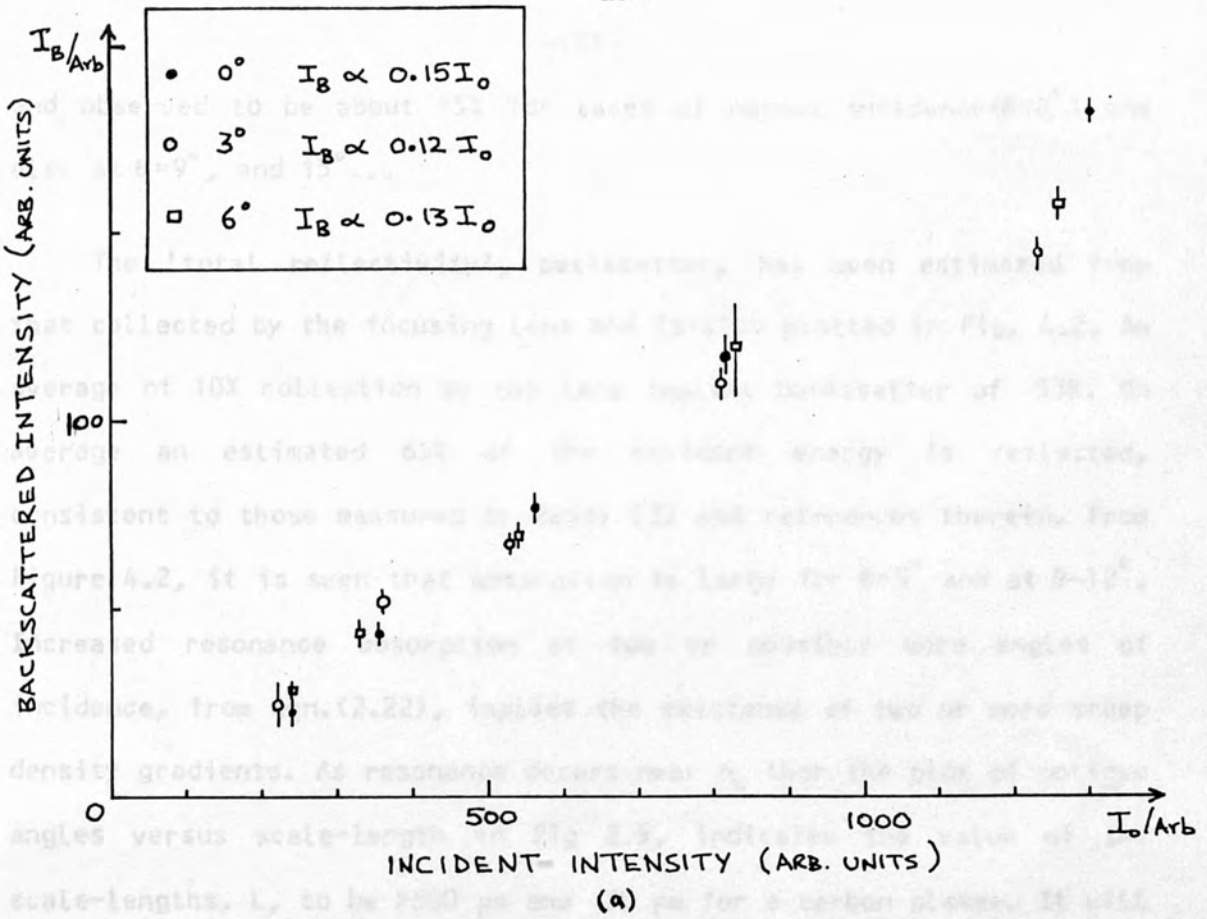

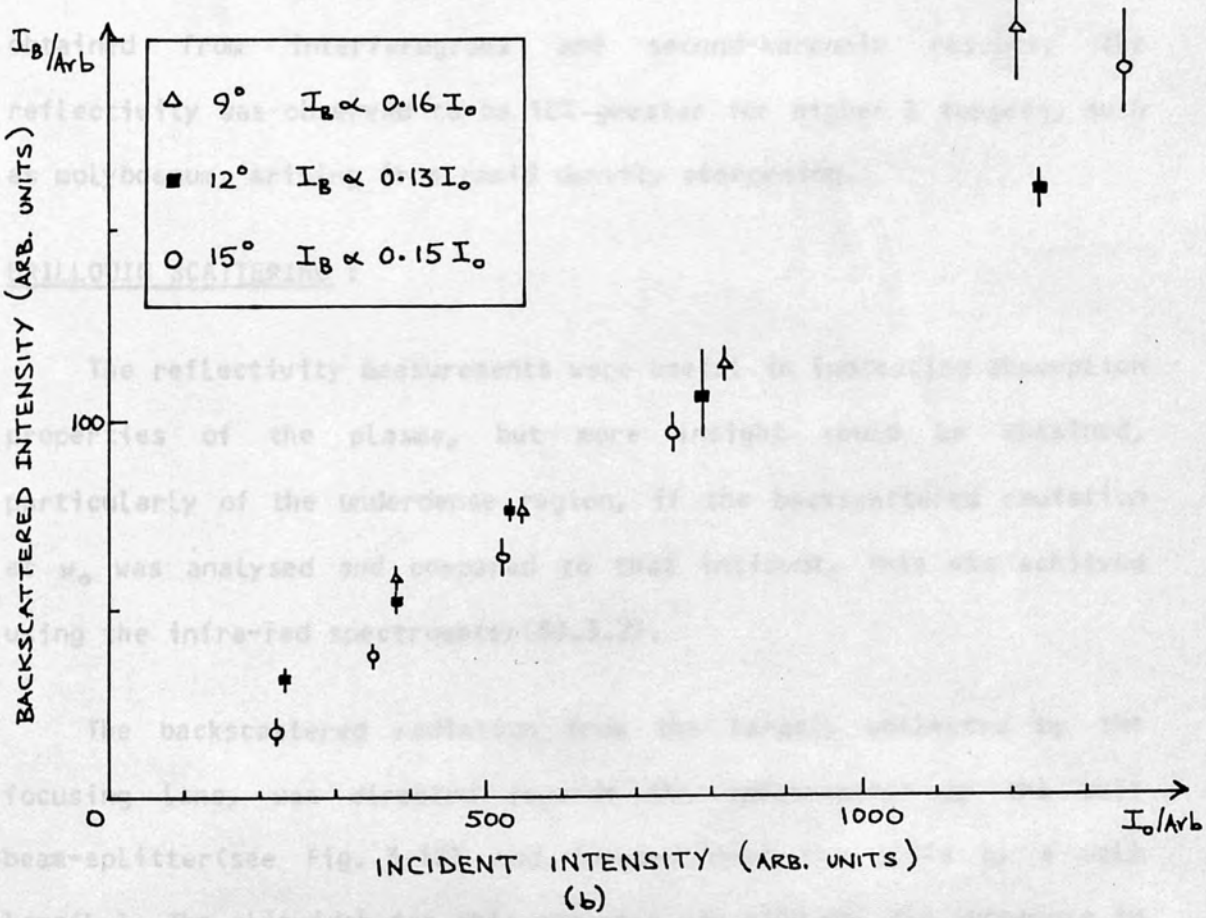

FIGURE 4.1 : Backscattered intensity vs. incident intensity

and observed to be about 15% for cases of normal incidence($\theta=0^\circ$) and also at $\theta=9^\circ$, and 15°...

The 'total reflectivity', backscatter, has been estimated from that collected by the focusing lens and is also plotted in Fig. 4.2. An average of 10% collection by the lens implies backscatter of 53%. On average an estimated 65% of the incident energy is reflected, consistent to those measured by Basov [2] and references therein. From Figure 4.2, it is seen that absorption is large for $\theta\sim3^\circ$ and at $\theta\sim12^\circ$. Increased resonance absorption at two or possibly more angles of incidence, from eqn.(2.22), implies the existence of two or more steep density gradients. As resonance occurs near n_c then the plot of optimum angles versus scale-length in Fig 2.5, indicates the value of the scale-lengths, L, to be >500 μm and 70 μm for a carbon plasma. It will be shown later (**§4.3.1**) that these results are consistent with those obtained from interferograms and second-harmonic results. The reflectivity was observed to be 10% greater for higher Z targets, such as molybdenum, arising from rapid density steepening.

BRILLOUIN SCATTERING :

The reflectivity measurements were useful in indicating absorption properties of the plasma, but more insight could be obtained, particularly of the underdense region, if the backscattered radiation at w_o was analysed and compared to that incident. This was achieved using the infra-red spectrometer(**§3.3.2**).

The backscattered radiation from the target, collected by the focusing lens, was directed towards the spectrometer by the salt beam-splitter(see Fig. 3.18) and focused onto the slits by a salt lens(L_1). The slitwidth for this analysis was ~100 μm. The procedure in

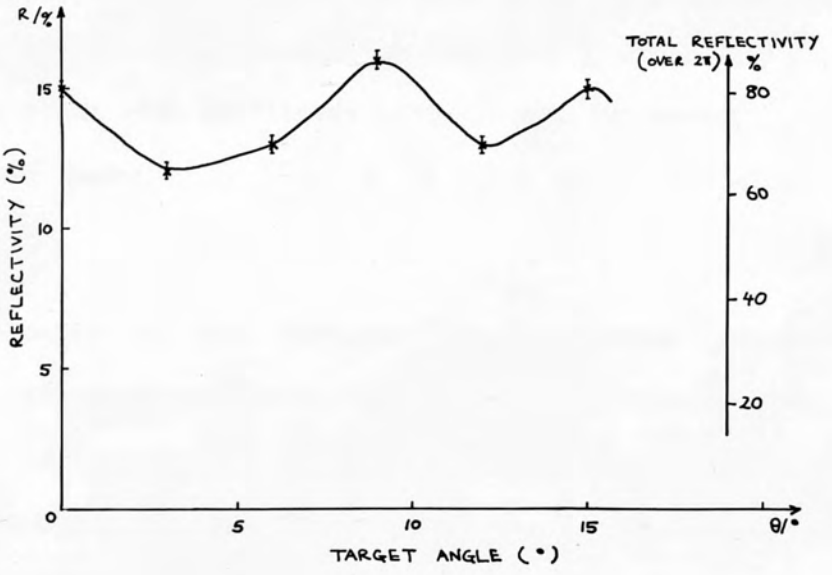

FIGURE 4.2 : Reflectivity vs. target angle

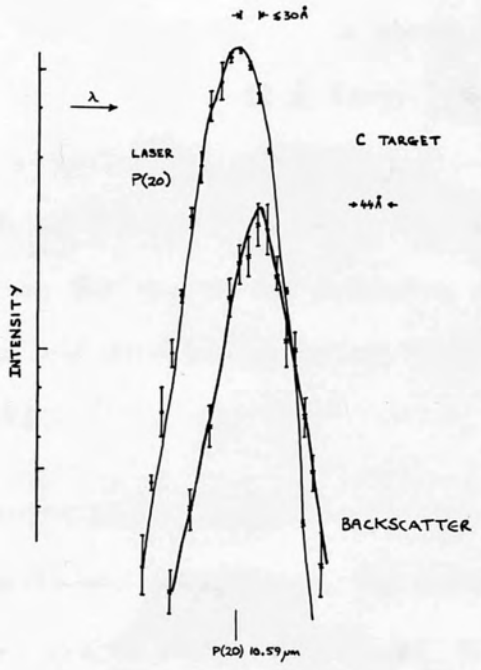

FIGURE 4.3 : Incident & backscattered spectrum

§3.3.2 for taking spectra around w_o was then followed, i.e. after having aligned the system with He-Ne beam and approximated for 10.6 μm region. The Brillouin spectrum was then built up from many(>70) shots. A laser spectrum was also taken by inserting a mirror(M_2) in CO_2 laser beam path, along with sufficient attenuators. The incident spectrum was taken either immediately prior or directly after taking the Brillouin spectrum.

An example of the incident laser spectrum compared with a backscattered spectrum, from a carbon target, is shown in Fig. 4.3. The wavelength indicates that the CO_2 laser is mainly lasing on the P(20) line, with p-polarisation(§3.2.6), and the backscatter shows a small contributory effect due to a weak P(18) line!

Brillouin results indicate the backscattered spectra to be displaced in wavelength, with respect to incident radiation, by 30 Å to the red arising as a result of loss of incident photon's energy into an ion-acoustic wave. The line-width of the spectra does not show much variation though the spectrum is 10 Å larger which is due to the combination of forward reflection off the critical surface and the Brillouin scatter [23]. If this was the case, then one expects to see a shoulder in the spectrum, but due to the averaging over many shots this effect has been masked and only an asymmetry, towards the red, in the spectrum was observed(Fig. 4.3).

All the above results above used a grating laser cavity. However, when a mirror laser cavity was substituted, the laser line had a larger fwhm of 90 Å with sizeable side lines from adjacent vibrational transition modes. The Brillouin spectrum was typically shifted by 30 Å to the red from w_o, for the case of a planar carbon target.

However, the ablation velocity was shown to be 10^6 cm/s by shadowgrams [23] which would produce a blue shift of approximately 5 Å. The ion-acoustic wave which modulates the electron density to cause the Brillouin shift is travelling through this plasma. Since the plasma is travelling towards the laser there is a blue shift of 5 Å and hence the Brillouin red shift is 35 Å.

Estimates for the plasma temperature were made using the matching conditions(2.34-5) and the dispersion relations(2.36-8). The incident frequency w_o, ion-acoustic frequency w_s and ion-acoustic velocity c_s to the electron density n_e,

$$w_s/w_t \simeq 2c_s[1 - n_e/n_c]^{1/2}/c \qquad (4.2)$$

where the approximations $w_t \sim w_p$, $k_t \sim k_i$, $w_t = w_s + w_p$ and $c_s << c$ have been used. In (4.2) c represents the speed of light, n_e and n_c the electron and critical densities respectively. As the wavelength shift $\delta\lambda$ is related through

$$\delta\lambda/\lambda = w_s/w_t \qquad (4.3)$$

implies

$$\delta\lambda \sim 5 * T_e^{1/2}[1 - n_e/n_c]^{1/2} \quad \text{Å} \qquad (4.4)$$

for a carbon(Z=6,A=12) target, where the plasma temperature, T_e, is in electron-volts.

Since SBS occurs in the underdense region($n_e < n_c$), it is expected that the resulting spectrum reflects the broad nature of the ion wave spectrum. However, the most important interaction region is near the critical surface, so for the above shifts of 25-30 Å plasma temperatures of 150-350 eV at $n_e = 0.9n_c$ are deduced. The significance of these results are dealt in the final section of this chapter(§4.5).

4.2 SECOND HARMONIC (CO_2 SYSTEM)

Nonlinear interactions of the electromagnetic waves with a plasma, mentioned earlier in Chapter Two, can lead to anomalous absorption of the laser radiation and consequent deformation of the spectrum of the

radiation reflected from the plasma. Therefore, an analysis of the spectra around the second harmonic would indicate the processes taking place within the plasma, particularily in regions with densities close to the critical. This section presents the 2w spectral results, for 10.6 μ radiation, with an aim to identify the processes involved with further discussion following in the final section **§4.5.**

A modified gold-doped germanium detector(**§3.3.3**) biased at 10 μA and pre-amplifiers(giving a net gain of 50x) in conjunction with the infra-red spectrometer(**§3.3.2**) were used to obtain the second harmonic, 2w, results. Procedure similar to that for Brillouin backscatter(**§4.1**) was followed, with the exception that the spectrometer slitwidth was 200 μm and spectral measurements were taken around the second harmonic(5.3 μm). This large slitwidth was necessary due to weak 2w signal levels and represented an instrumental width of ~60 Å.

Typical oscillograms (on Tektronix 7834 storage oscilloscope) from the Au-Ge detector are shown in Figures 4.4(a-d). These oscillograms showed much variation, though often a second structure was observed. It seemed to be arbitrary whether the first or second peak dominated. All the oscillograms had a fwhm less than that of the laser pulse, but were not always constant, as in some instances the 2w traces had a fwhm <20 nsec. Oscillogram (d) shows the superimposition of the incident and 2w signal(inverted) and indicates that the 2w signal coincides to within 10 nsec of the peak of the incident laser pulse. Careful examination, particularly of oscillogram (c) taken at full bandwidth, shows structure at 10 nsec intervals of the CO_2 laser pulse to be reflected in the temporal variation of 2w. This implies the second harmonic intensity to be essentially in phase with the incident intensity. The two peaks corresponding to enhanced 2w intensity at

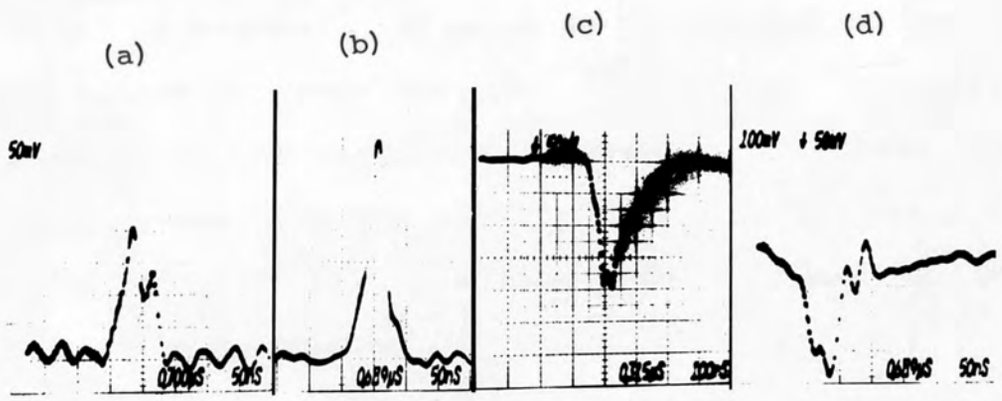

FIGURE 4.4 : Oscillograms of 2W signal

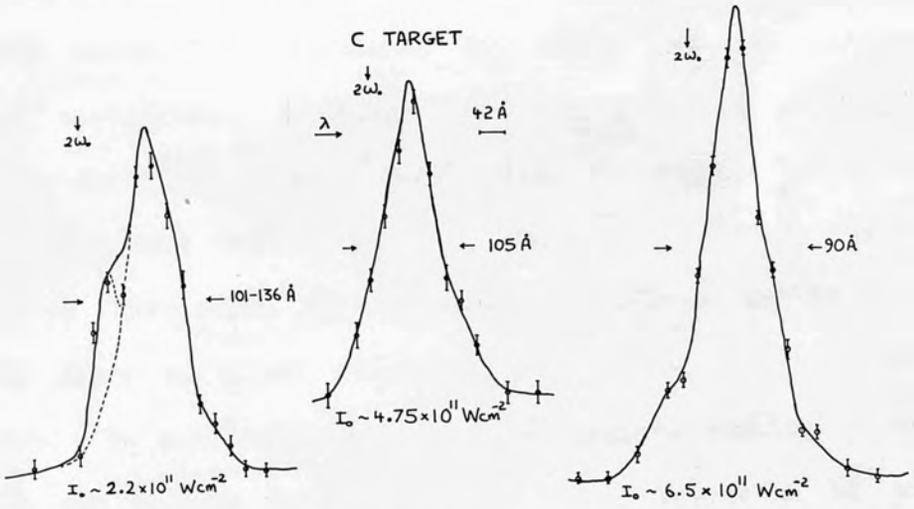

FIGURE 4.5 : 2W spectra (carbon target)

different times (Fig. 4.4), gives an asymmetric second harmonic spectrum as a result of slightly displaced spectra. This was also indicative of presence of two or more scale-lengths within the plasma.

Second harmonic spectra were taken from carbon and molybdenum targets at various irradiances and target angles. A typical 2w spectrum being built up from over sixty shots. Several 2w spectra from a carbon plasma are shown in Figures 4.5(a-c) for different irradiances. The spectra show a weak asymmetry with any fine spectral structure, observed for the neodymium system(§4.4), masked because of the averaging nature of the results.

From the collected spectral data, the intensity, displacement and broadening of the second harmonic were determined. The displacement($\delta\lambda$) of 2w line from its true value and its broadening($\Delta\lambda$) have been plotted against irradiance, I_o, in Figures 4.6 & 4.7 respectively. Once again regression fits have been made and correlation coefficients given. The second harmonic shows a clear decrease in displacement, from 120 Å to ~50 Å, with increasing irradiance, I_o, which is reflected in the correlation coefficient, r=0.7(Δr= 0.1). Extrapolation of this data implies zero shift for $I_o \sim 6*10^{12}$ W/cm^2; i.e. the Doppler shift of the critical surface will then be equal to the second harmonic red shift. Alternatively, the onset of increased turbulence at these high irradiances leads to a net effect of a zero red shift in the 2w spectrum. This is confirmed in the interferometric results of Sudera [23] for carbon targets for irradiances in the region of 10^{12} W/cm^2. This displacement is discussed further in §4.5 in relation to prevalent theories, particularly those by Cairns and Silin(Chap. 2, refs. 37 & 146 respectively). However, the broadening(fwhm) of 2w shows a definite increase, from 60 Å to 100 Å, with irradiance(Fig. 4.7) as a result

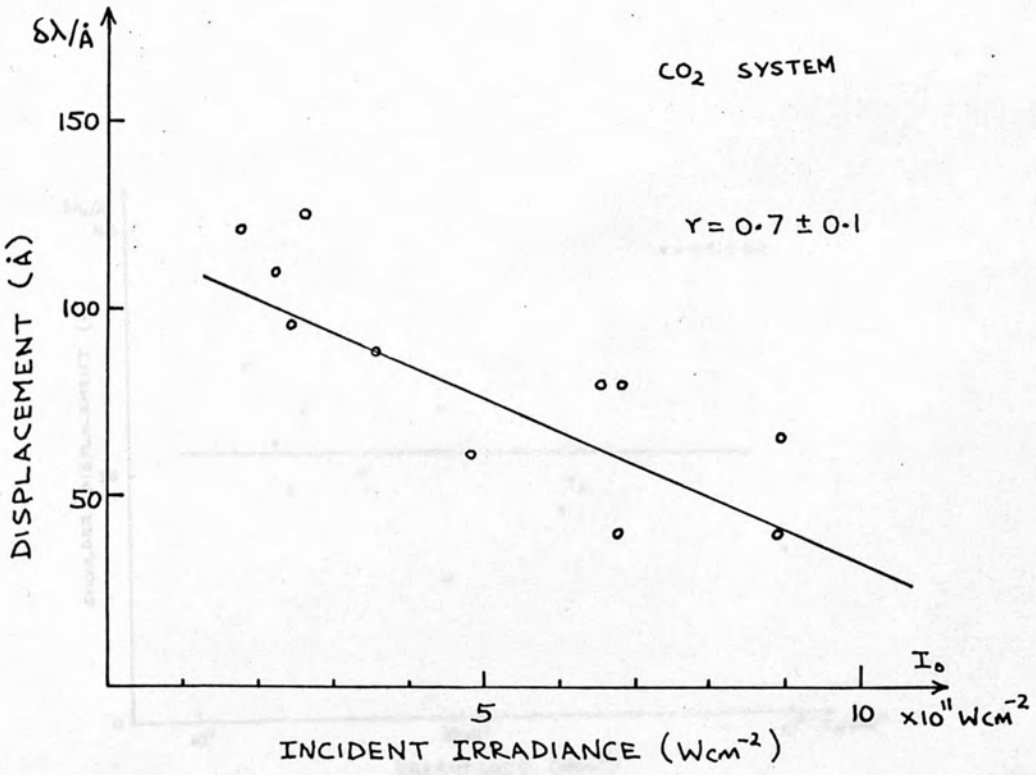

FIGURE 4.6 : 2W shift vs. irradiance

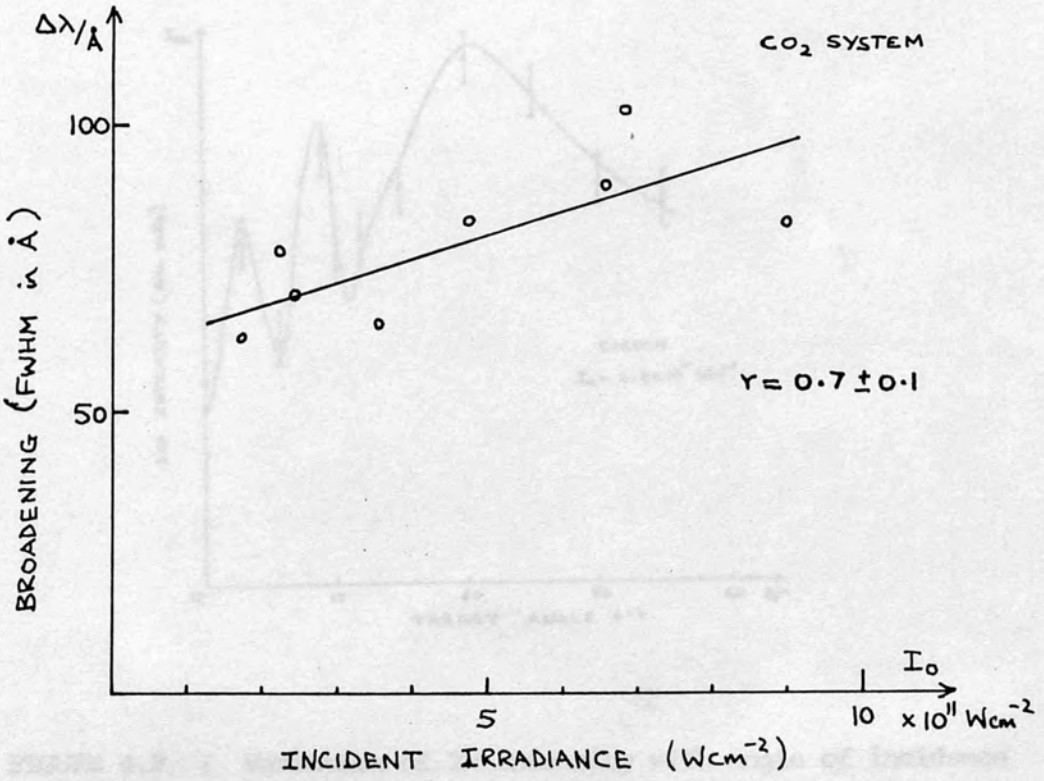

FIGURE 4.7 : 2W broadening vs. irradiance

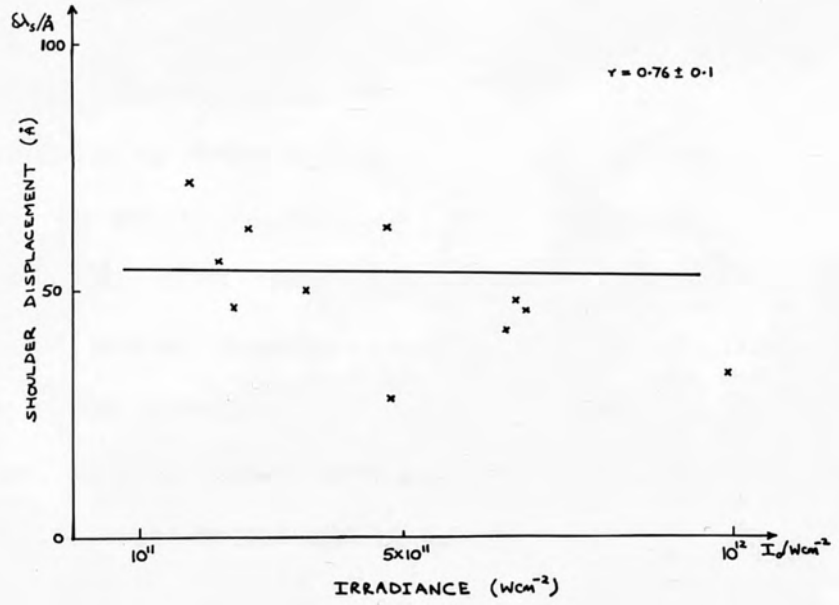

FIGURE 4.8 : Shoulder displacement vs. irradiance

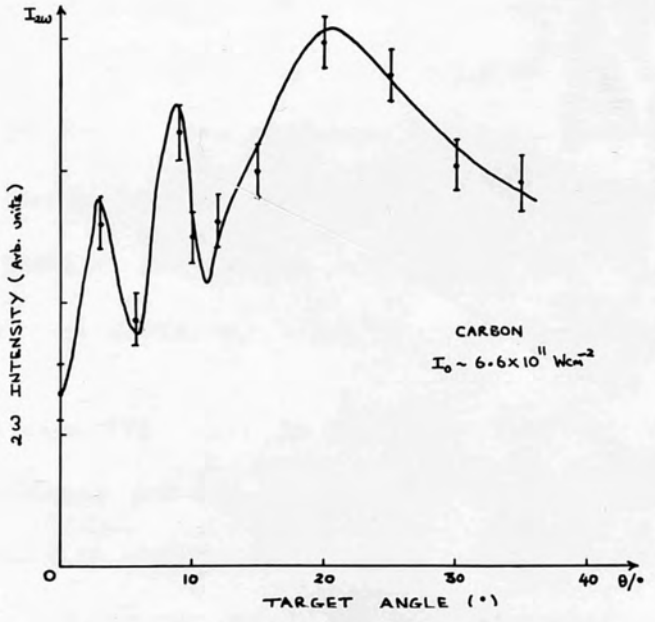

FIGURE 4.9 : Variation of 2W intensity with angle of incidence

of motion of the critical surface (maximum contribution of 10 Å) and variations of density scale-lengths at n_c. The broadening was of the order of the incident radiation.

On the few spectra that did show a shoulder, its displacement versus irradiance is shown in Figure 4.8. This shoulder was genuine and was not due to another close lasing line since the displacement was well under 100 Å. It is thought to arise as a consequence of two or more dominant second harmonic spectra slightly displaced from each other, due to the plasma having several different scale-lengths during its lifetime. This has been confirmed in the intensity variation of 2w with target angle(see below) and by optical probing(**§4.3.1**).

An experimental run using angled carbon targets was also made. Spectral data were taken around the 2w peak, after having already determined 2w's approximate position from an initial coarse scan, for incident irradiance within a tolerance of under 10%. This procedure was carried out for each target angle, θ. The results thus described the variation of the 2w intensity($I_{2\omega}$) with angle of incidence(θ). At first a broad range of angles were covered(0°-40°) to give some insight into areas of importance. From these it was then decided to concentrate for $0^\circ < \theta < 15^\circ$ in smaller steps,(Fig. 4.9). Note that $I_{2\omega}$ represents an average over several shots.

From this plot(Fig. 4.9) it was seen that $I_{2\omega}$ was enhanced for near normal incidence and for $\theta = 20^\circ$. This consequently implies strong absorption at similar angles. If the main absorption mechanism is taken to be resonance absorption, and using optimum angles of 3°, 9° and 20° in equation (2.21) gives plasma scale-lengths of >400 μm, 150 μm and <20 μm. The implication of these results is the existence of three different density scale-lengths within the plasma. Other workers [7]

have observed this and also been theoretically shown to be possible [11,14,21]. Sudera [23] has also reported, using optical diagnostics, existence of several scale-lengths and seen them to vary in time on similar plasmas (the next section, **§4.3.1,** discusses some of these results in greater detail).

The scaling of $I_{2\omega}$ with incident intensity I_o was investigated for two different target materials, viz. carbon(Z=6) and molybdenum(Z=42). For planar carbon targets the intensity was measured at the peak of the 2w spectrum and is plotted in Fig. 4.10(a). This indicates the scaling parameter for $I_{2\omega}$ to be 2.4(i.e. $I_{2\omega} \propto I_o^{2.4 \pm 0.1}$). A similar result was obtained for $I_{2\omega}$ readings taken at a spectrometer setting of exactly $2w_o$(i.e. 5.3μ). The latter method was employed in the case of molybdenum targets[Fig. 4.10(b)], which also showed a similar variation, thus, indicating the scaling parameter to be independent of atomic number A; cf. Basov [2], Eidmann & Sigel [3].

The increase in the exponent from 2.0 [c.f. eqn. (2.72)] to 2.4 is attributed to the density gradient steepening as resonance absorption is enhanced. Evidence for this is also shown in the reflectivity results (**§4.1** & Fig. 4.2) and optical diagnostics (**§4.3.1** & Fig. 4.14).

Finally, the maximum conversion of incident radiation to second harmonic, for a carbon target, was 10^{-6} at $I_o \sim 10^{12}$ W/cm^2. For molybdenum the conversion was $>10^{-5}$, an order of magnitude greater, for similar irradiances. These are well within the observations mentioned in **§2.5.4,** which were mainly with neodymium systems of shorter pulse(nsec) duration. This implies that higher Z targets absorb the radiation much more efficiently, due to profile steepening and rippled critical surface [23], even though a greater proportion is reflected.

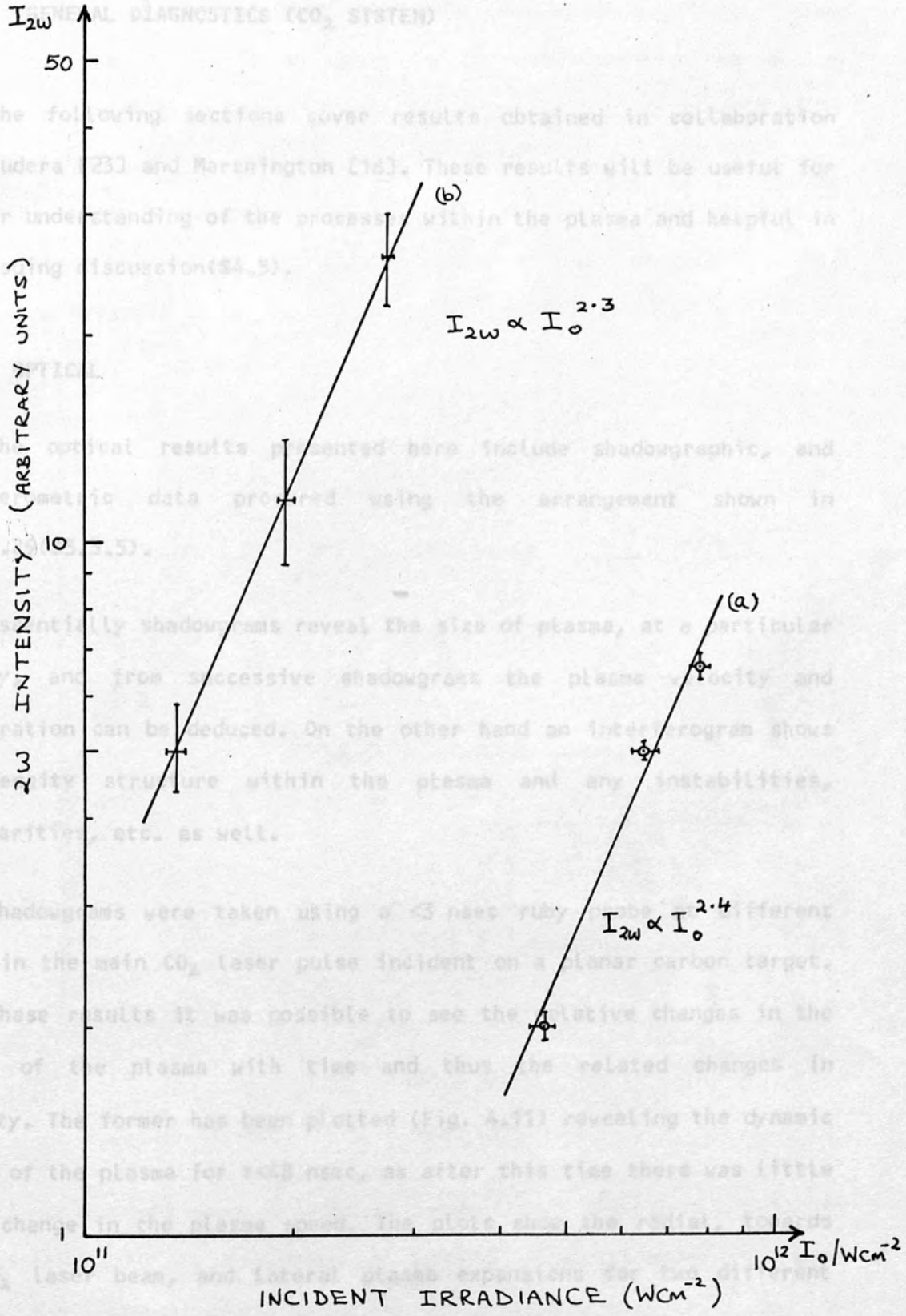

FIGURE 4.10 : $I_{2\omega}$ vs. I_o for (a) Carbon & (b) Molybdenum.

4.3 GENERAL DIAGNOSTICS (CO_2 SYSTEM)

The following sections cover results obtained in collaboration with Sudera [23] and Marchington [16]. These results will be useful for further understanding of the processes within the plasma and helpful in the ensuing discussion(§4.5).

4.3.1 OPTICAL

The optical results presented here include shadowgraphic, and interferometric data procured using the arrangement shown in fig. 3.29(§3.3.5).

Essentially shadowgrams reveal the size of plasma, at a particular density, and from successive shadowgrams the plasma velocity and acceleration can be deduced. On the other hand an interferogram shows the density structure within the plasma and any instabilities, peculiarities, etc. as well.

Shadowgrams were taken using a <3 nsec ruby probe at different times in the main CO_2 laser pulse incident on a planar carbon target. From these results it was possible to see the relative changes in the extent of the plasma with time and thus the related changes in velocity. The former has been plotted (Fig. 4.11) revealing the dynamic nature of the plasma for t<48 nsec, as after this time there was little or no change in the plasma speed. The plots show the radial, towards the CO_2 laser beam, and lateral plasma expansions for two different irradiances.

The plasma expansion is seen to be asymmetrical, being a factor x1.5 greater along the target's surface with respect to expansion

towards the CO_2 beam. This resulting flattened spherical image indicates the radiation pressure to be considerable. The plasma velocity, essentially the gradient, increases with irradiance(as might be expected) and measured to be $2*10^7$ cm/sec for t<2 nsec, $0.19*10^7$ cm/sec for 2 nsec< t <4 nsec and $\sim 10^6$ cm/sec after t=30 nsec; i.e. after t=30 nsec the plasma expansion was constant for the remaining duration of the CO_2 laser pulse.

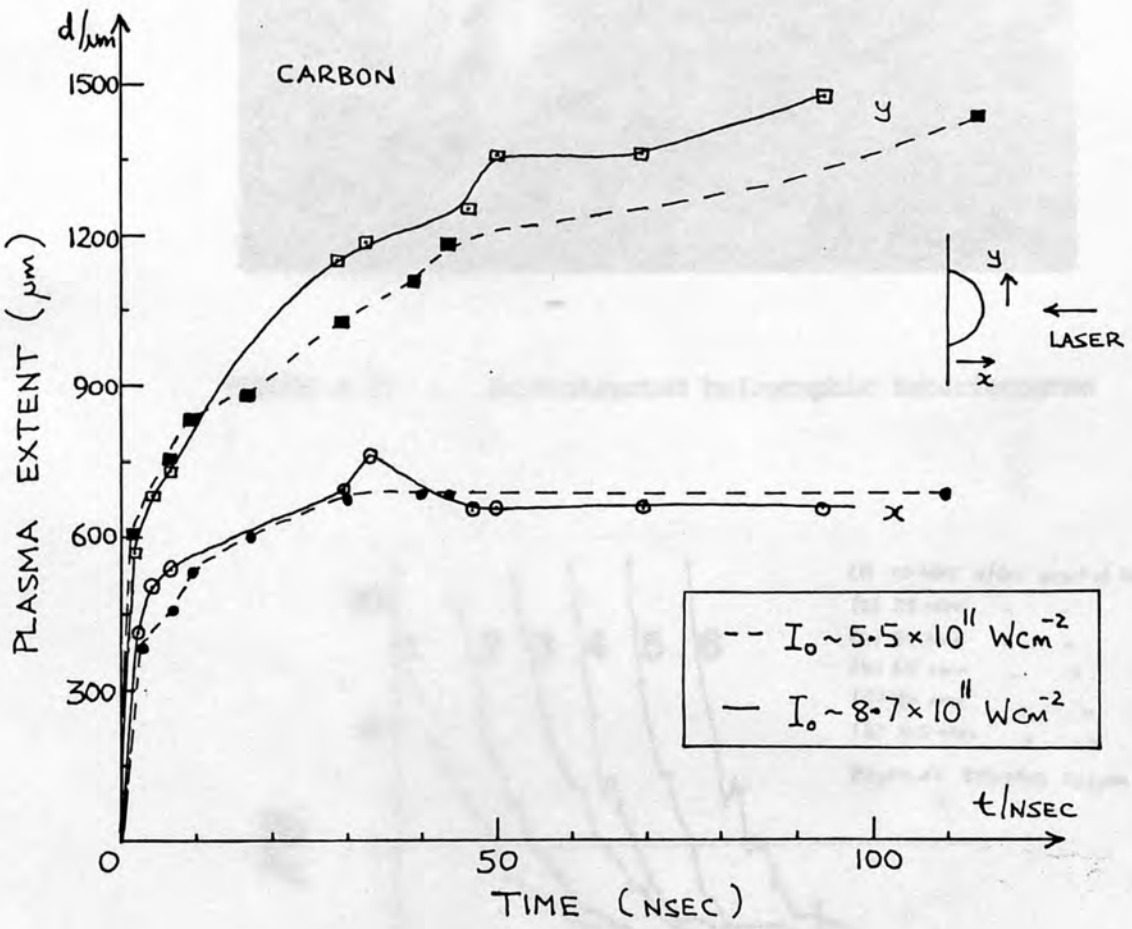

FIGURE 4.11 : Plasma expansion

A white light reconstructed hologram from a planar carbon target irradiated, with CO_2 radiation, at $I_o \sim 6*10^{11}$ W/cm^2 is shown in Figure 4.12. The reconstruction being possible with white light as the original holographic interferogram, recorded on Agfa 10E75 film, was of the focused type. The interferogram was recorded 80 nsec after beginning of CO_2 laser pulse with a 2 nsec fwhm ruby probe. Applying

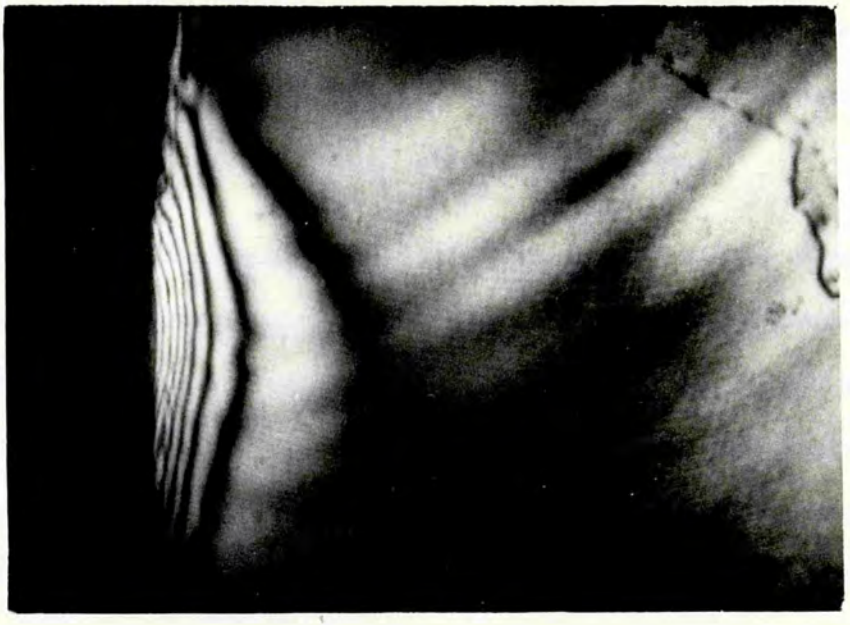

FIGURE 4.12 : Reconstructed holographic interferogram

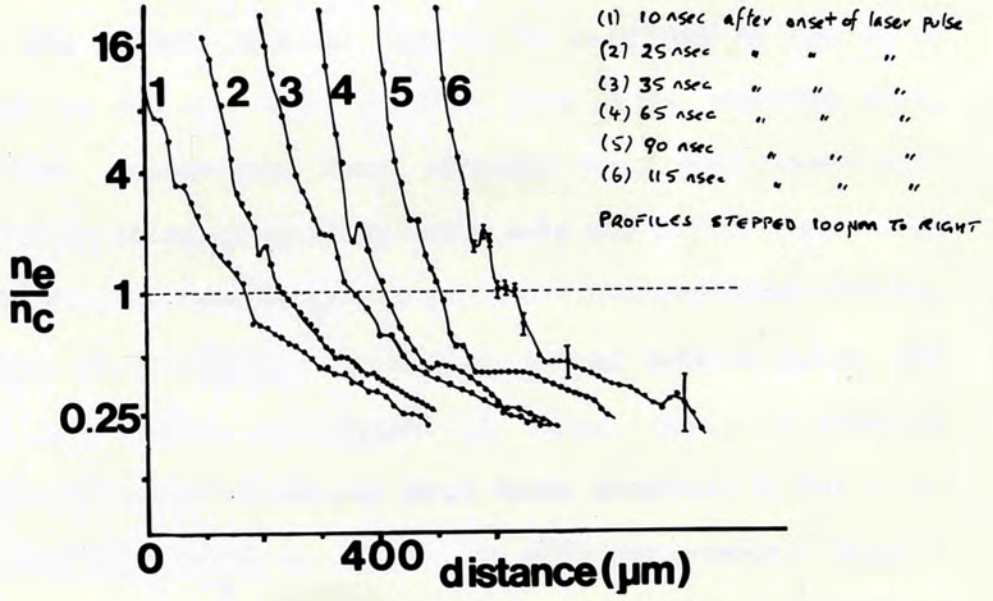

FIGURE 4.13 : Electron density profiles

the Nestor-Olsen [22] technique for Abel inversion, to the interferometric data, gives an electron plasma density profile structure like those shown in Figure 4.13 for various moments after the onset of the laser pulse. These values have a 20% error arising from refraction and limitations on fringe shift measurements.

From the density measurements at various times, it was found that the critical surface region was accelerated, in less than 20 nsec, to a velocity of $5*10^6$ cm/sec. With such anti-parallel accelerations and exponential density gradients, Baker [1] shows that Rayleigh-Taylor instabilities can develop. Fringes in Figure 4.11 showing ripples is evidence of such an instability. Other shadowgrams and interferograms have also shown presence of other instabilities; viz. 'jetting' [23] and thermal instabilities, particularly in high Z targets.

Development of profile steepening was seen to occur over the first 50 nsec in which time the irradiance has reached its peak value. The plateau near the quarter critical surface is predicted by Lee et al [14] but that at 0.5 n_c, also apparent from x-ray emmision data, requires further explanation. X-ray emission data [16] shows much periodic variation in emission along laser axis and radial directions, indicating the fluctuations to extend well into the underdense plasma. Another feature of the density profile is a bump between 1.6 n_c and 2.2 n_c with a density modulation of about 30%: A feature characteristic of the refraction and shock front predicted by Max et al [17]. Simulations by Virmont et al [24] on radially symmetric plasmas finds such a bump near the critical surface, attributing its width to the position of n_c and as the square of the ratio of radiation pressure to thermal pressure. For a temperature of 200 eV and an absorption coefficient of 0.4, the calculated width of 25 μm agrees closely to the

observed values of 30 to 40 μm.

From the plots one can obtain the plasma scale-length,

$$L = (1/n_e . dn_e/dx)^{-1} \quad . \qquad (4.5)$$

From successive interferograms, at different stages of plasma development, the scale-length at the critical surface, L_c, for CO_2 radiation was calculated. These have been plotted in Fig. 4.14 showing the scale-length variation in the dynamic moments of the plasma.

The scale length, L_c, varies from 30 μm to 120 μm over this dynamic period. Recall that resonance absorption occurs in this region and existence of more than one scale length (20 μm & 150 μm) was apparent from the angular variation of the second harmonic intensity (Fig. 4.9).

Further work on the scale length variation with irradiance [23] gives lower values than those predicted by a self consistent model [19], which omitted the ponderomotive force whilst the capacitor model of Estabrook et al [6], which includes the ponderomotive effect, implies the observed results to be high.

To summarise, the holographic interferometric double-exposed results, at 10 nsec intervals, have shown the plasma to be essentially steady-state for low Z (e.g. Carbon) targets. However, for high Z (e.g. Copper) targets a steady-state model is no longer applicable, as pronounced changes were observed within the 10 nsec intervals. Implications of these results are that a variable dependent on Z in a non-linear way is required. At high Z, there is more likelihood of transfer of instabilities due to shock waves as opposed to low Z where hardly any shocks exist. This also implies fewer instabilities and the plasma can then be easily modelled. The critical density still exists

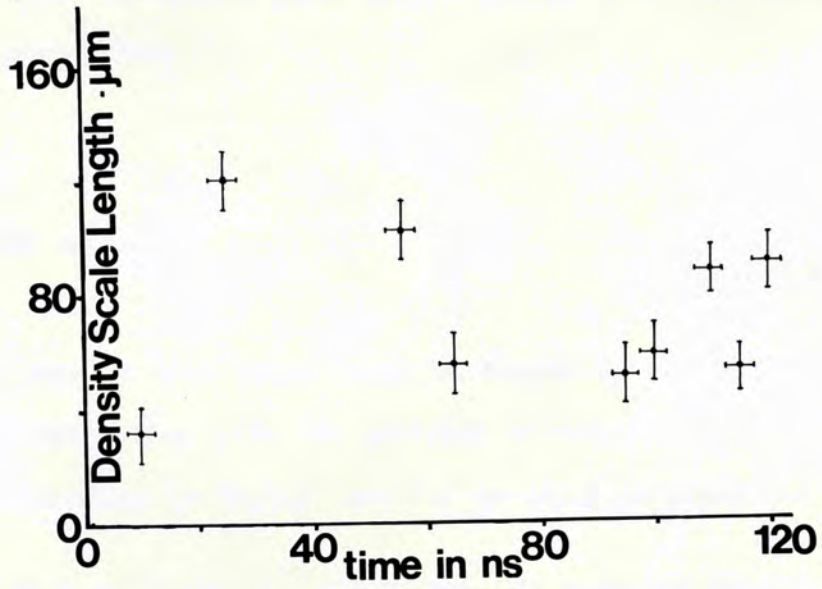

FIGURE 4.14 : Temporal variation of plasma scale-length (at n_c)

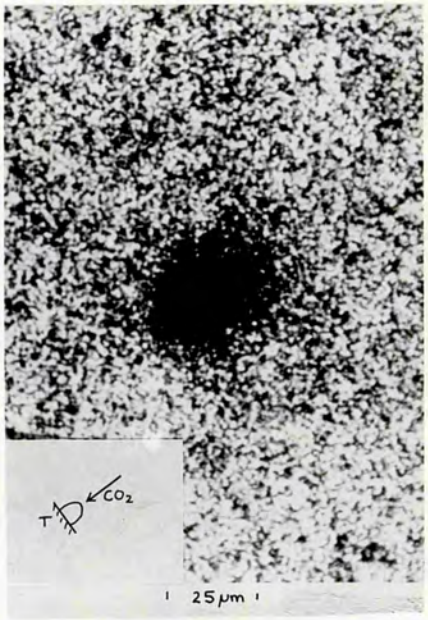

FIGURE 4.15 : X-ray photograph from a pinhole camera

for low Z targets but its gradient was seen, from the ablation fronts, to be not as steep as for high Z targets. The plasma velocity and thus the temperature increased with atomic number A of the target due to increased absorption.

4.3.2 X-RAY IMAGES

X-ray results like those shown in Figure 4.15 were obtained using a thin aluminium disk with two pinholes of diameter 10 μm, with the set-up as described in **§3.3.6,** and 1.5 μm and 5 μm aluminium foils.

Note that the image is ellipsoidal, as expected from illuminating a target. Figure 4.16 shows the microdensitometer traces of the x-ray image along axis indicated in the inset. Both traces imply the x-ray emitting region to be <35 μm in diameter. The intensity ratio of the two scans was approximately two with the corresponding 1/e cut-offs at 700 eV and 1.5 keV for 1.5 μm and 5 μm foils respectively.

Figure 4.17 shows the amount of target debris deposited from a carbon target, onto the foil, after a single laser shot(the outer faint circular pattern is due to the effect of vacuum).

From the x-ray attenuation coefficients for the foils used here it

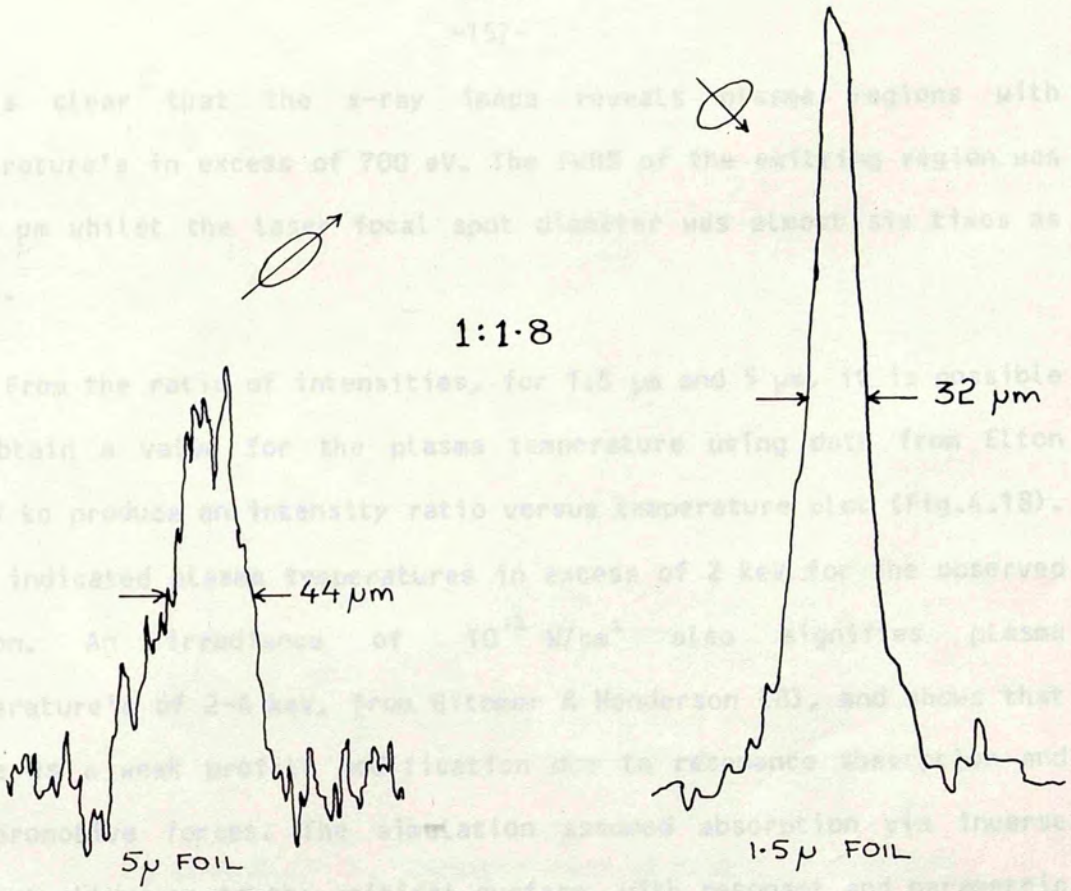

FIGURE 4.16 : X-ray distribution on target

FIGURE 4.17 : Foil damage

it is clear that the x-ray image reveals plasma regions with temperature's in excess of 700 eV. The FWHM of the emitting region was 32 ± 5 μm whilst the laser focal spot diameter was almost six times as great.

From the ratio of intensities, for 1.5 μm and 5 μm, it is possible to obtain a value for the plasma temperature using data from Elton [4,5] to produce an intensity ratio versus temperature plot (Fig.4.18). This indicated plasma temperatures in excess of 2 keV for the observed region. An irradiance of 10^{12} W/cm^2 also signifies plasma temperature's of 2-4 keV, from Gitomer & Henderson [8], and shows that there is a weak profile modification due to resonance absorption and ponderomotive forces. The simulation assumed absorption via inverse bremsstrahlung up to the critical surface, with resonant and parametric processes taking over near the critical to provide the major contribution.

Further work is presently being carried out [16] using phototubes and x-ray multichannel plate intensifying systems to obtain spatial and temporal behaviour of the plasma temperature.

4.3.3 TARGET DAMAGE

Typical damage to carbon and molybdenum targets when irradiated by CO_2 laser radiation at $I>10^{11}$ W/cm^2 are shown in Figures 4.19 & 4.20. For carbon it can be seen that the laser radiation penetrates deep (550 μm) into the target, creating a sharp cone of diameter 180 μm. A deeper impression in carbon results due to its weak structure whilst molybdenum illustrates a highly symmetrical damage pattern. The outer part of the focus show the coronal and after effect spread from the

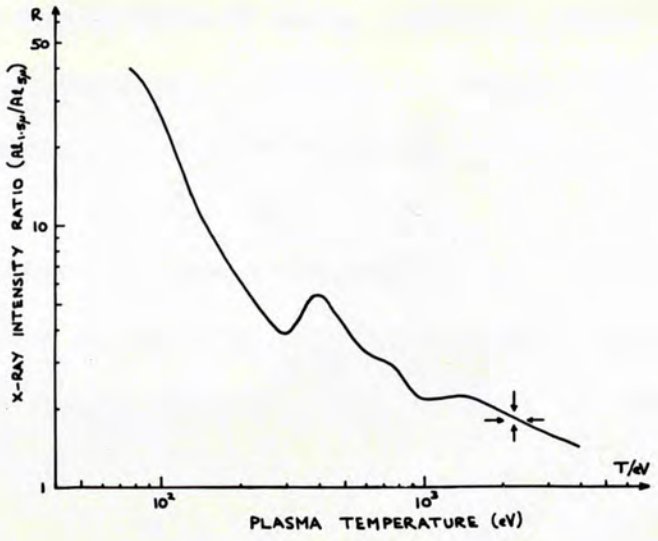

FIGURE 4.18 : Determination of plasma temperature

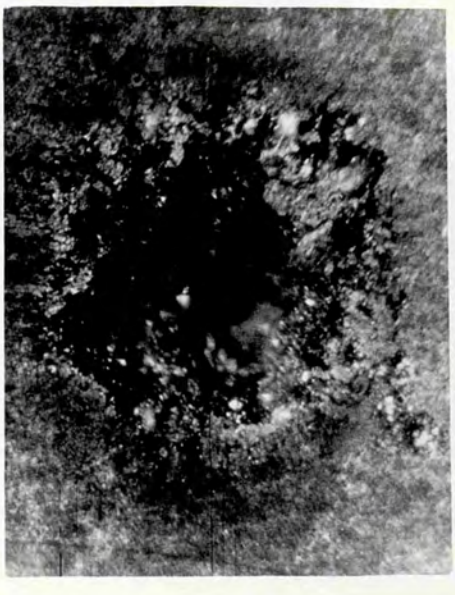

FIGURE 4.19 : Target damage for carbon

FIGURE 4.20 : Target damage for Molybdenum

created hot plasma.

In the case of carbon the crater amounted to about $5*10^{-6}$ cm^3 in volume. Invoking conservation of energy and using simple arguments one can equate the electromagnetic energy to the amount of material ablated at some average speed, as in equation (4.6).

$$1/2\rho V v^2 \sim E \qquad (4.6)$$

where ρ is the density of target material, V is the volume ablated at an average velocity v and E is the incident electromagnetic energy. Taking E = 15 J gives an ablation speed of about 10^6 cm/sec which is comparable to the plasma velocity.

4.4 SECOND HARMONIC (ND SYSTEM)

Continuing from **§4.2**, the analysis of the second harmonic for the neodymium case are now presented.

The scattered radiation from the targets was collected over a solid angle of $2\pi/3$ & 6° by the paraboloid(Table 3.4) and the laser focusing Icos lens respectively. The collected radiation was then directed and focused onto the slits, normally open to 100 μm, of the Spex 500 spectrometer(Table 3.6). The experimental arrangement has been shown in Figure 3.37 and indicates a reduction of 9.8x & 13.2x for the paraboloid & lens images respectively from eqn.(4.7)

$$M = v/u \ , \qquad (4.7)$$

where u and v are the object and image distances respectively.

The intensity of the scattered radiation was also measured, for the two cases, using silicon PIN diodes with narrow band filters at 532 nm. However, these results were not conclusive.

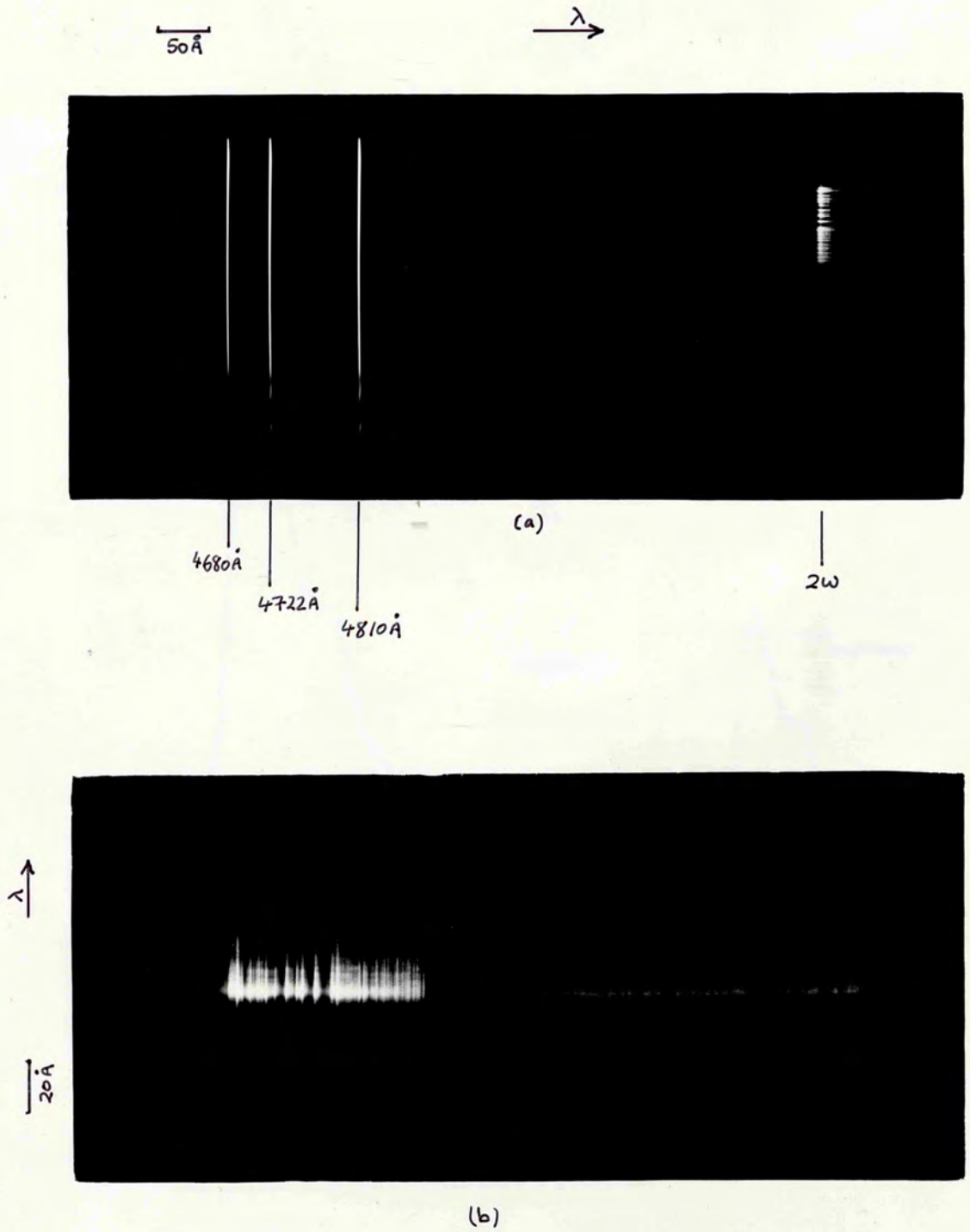

FIGURE 4.21 : Typical 2W result (AU target)

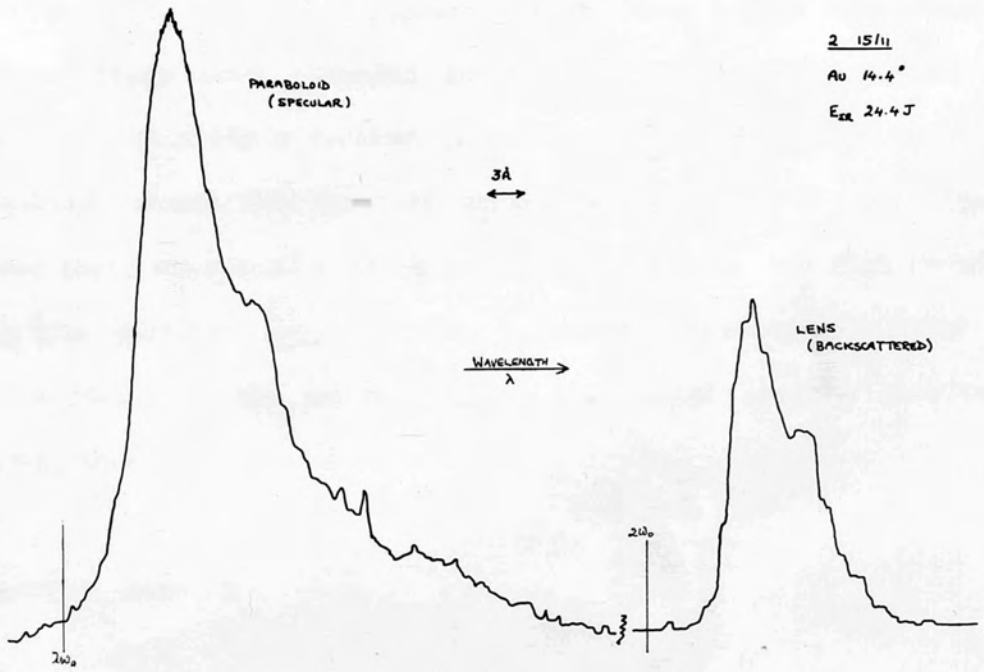

FIGURE 4.22 : 2W spectrum

The laser radiation from the Nd-glass laser of wavelength λ=1.0525 μm having a line-width of 0.1 Å, pulse duration of 1.7 nsec and energies of up to 100 J were focused, by an Icos F5 lens, to a typical diameter of 100 μm onto the target's (see **§3.5.2**) surface. The first laser shot, was taken with insufficient neutral density(ND) filters, resulted in an arc spectrum due to plasma formation at the slits of the spectrometer. This spectrum completely saturated any second harmonic spectrum. Subsequent spectra were obtained with sufficient ND filters. An example of the recorded spectra is shown in Fig. 4.21(a) along with the calibration lines from a zinc low pressure lamp. These lines were recorded immediately after a laser shot by exposing the film plate a further two minutes to a Zn UV lamp in situ. Figure 4.21(b) shows the spectral structure magnified 7x and Figure 4.22 shows the corresponding microdensitometer traces. The high density areas in the specular image in Fig. 4.21 are attributed to areas of high reflectivity in the paraboloid, as the radial pattern structure was reproducible.

4.4.1 GENERAL REMARKS

(i) SCANNING POSITIONS :

Since the targets were angled, the radiation at the specular angle was expected to give the true representation of the 2w spectrum. Thus the scanning positions on the paraboloid image had to be determined, which was done as follows:-

For any particular target angled at θ, the point P gives the true representation of the spectra. The position corresponding to this on the paraboloid image is where the microdensitometer trace was taken to give the 2w specular spectrum. In order to calculate the scanning

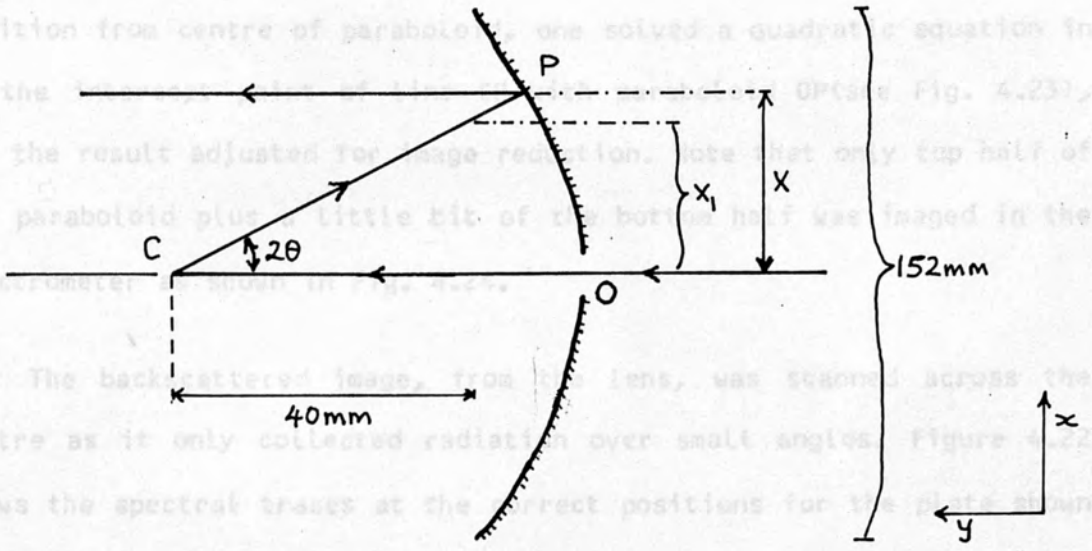

FIGURE 4.23 : Specular position on paraboloid

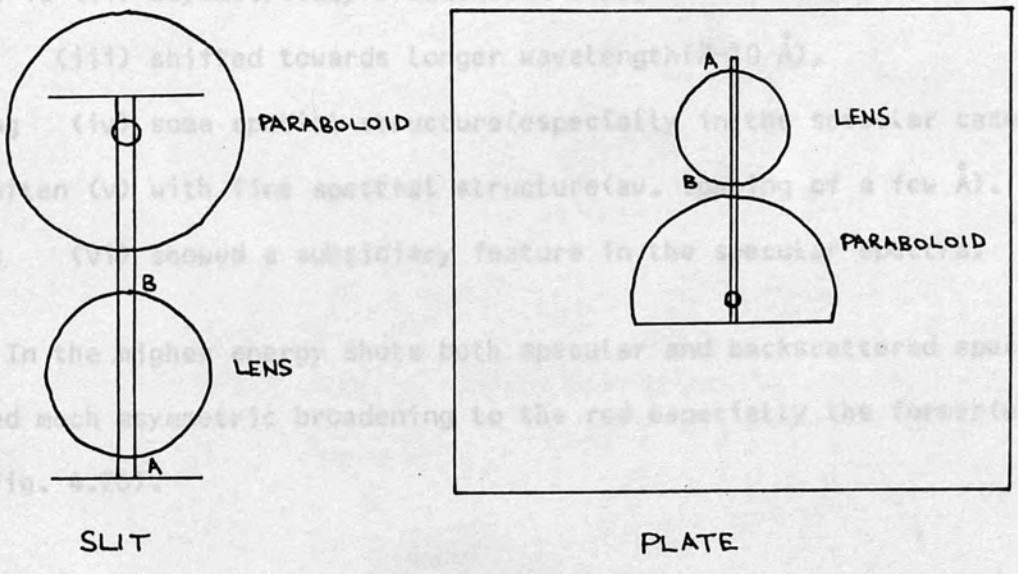

FIGURE 4.24 : Image on slit & film plate

position from centre of paraboloid, one solved a quadratic equation in X, the intercept point of line CP with paraboloid OP(see Fig. 4.23), and the result adjusted for image reduction. Note that only top half of the paraboloid plus a little bit of the bottom half was imaged in the spectrometer as shown in Fig. 4.24.

The backscattered image, from the lens, was scanned across the centre as it only collected radiation over small angles. Figure 4.22 shows the spectral traces at the correct positions for the plate shown in Fig. 4.21.

(ii) SPECTRAL RESULTS :

Typical spectral traces for gold and aluminium coated targets are shown in Figures 4.22 & 4.25. To summarise, the general observed spectral features were:-

(i) a resonance line near $2w_o$

which is (ii) asymmetricaly broadened(4-6 Å),

(iii) shifted towards longer wavelength(8-10 Å),

having (iv) some spatial structure(especially in the specular case),

and often (v) with fine spectral structure(av. spacing of a few Å).

A few (vi) showed a subsidiary feature in the specular spectra.

In the higher energy shots both specular and backscattered spectra showed much asymmetric broadening to the red especially the former(e.g. see Fig. 4.26).

(iii) TARGET DAMAGE :

Typical damage to a target(§3.5.2, Fig. 3.43) is shown in Figures 4.27. One can clearly see the area of laser energy deposition and the

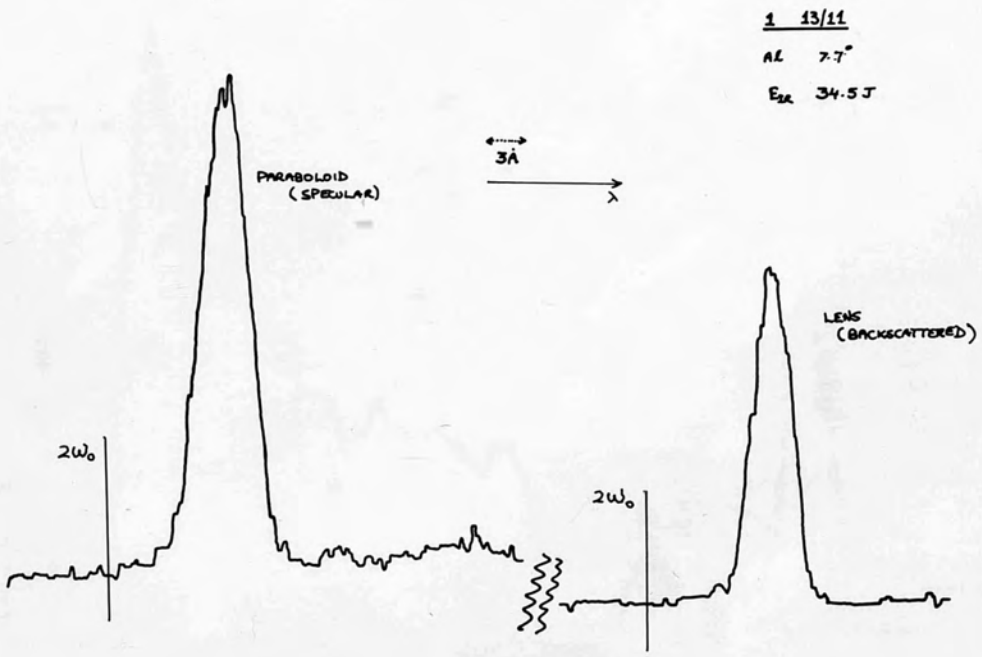

FIGURE 4.25 : 2W spectral trace (Al target)

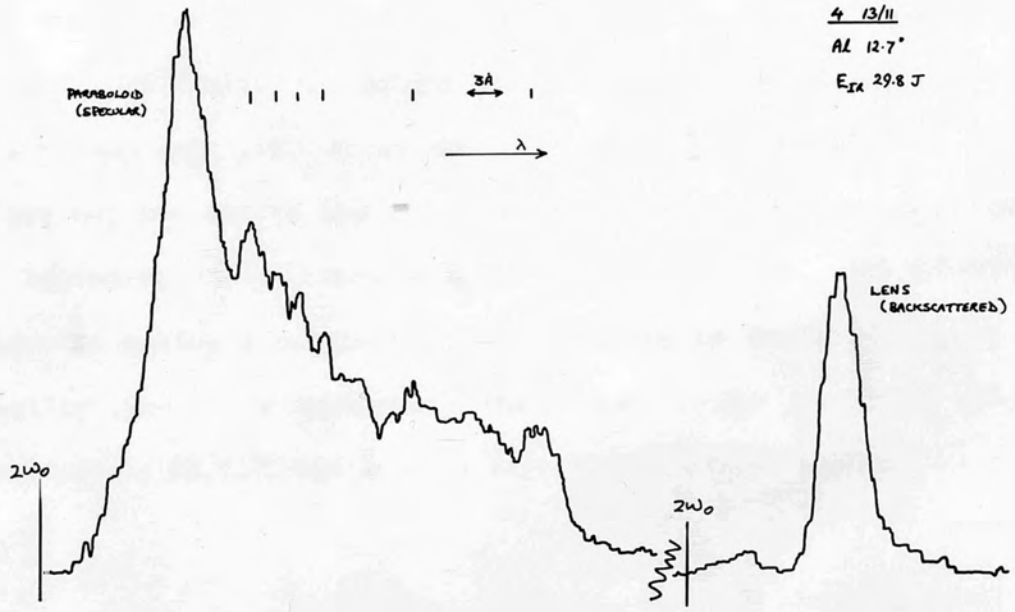

FIGURE 4.26 : Asymmetric broadening

subsequent crater left behind plus the effect of this energy concentration on the surrounding area of the crater. The size of the crater was approximately 100 μm * 400 μm, as the diameter of the target was known. The crater did not seem to possess circular symmetry but was rectangular. This may have been due to improper focusing or preference of expansion in the lateral direction.

(iv) QUALITY OF PARABOLOID :

The quality of the paraboloid, at the end of the experiment, is shown in Figure 4.28. As before one can see the damage to the parabola's coating; i.e. areas of high and low reflectivity. This damage was not all due to the scattered radiation as some was inherent at the beginning, which then progressively got worse. The spinning technique for making a paraboloid needs much to be desired to give a good quality paraboloic reflector. The target holder assembly, which was discussed in §3.5.2, can also be seen in the above figures.

4.4.2 QUANTITATIVE ANALYSIS

The results presented here consider the variation of the shift of the generated second harmonic from the true second harmonic with respect to:-

(a) the incident irradiance

and (b) target angle.

Also the dependence of the broadening of the second harmonic with respect to:-

(a) the incident irradiance

and (b) target angle are examined.

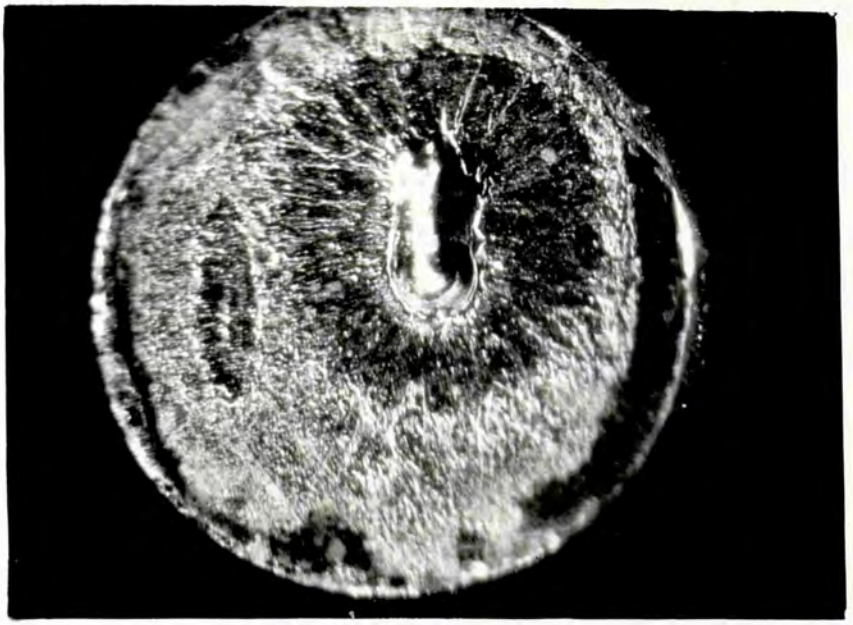

FIGURE 4.27 : Target damage

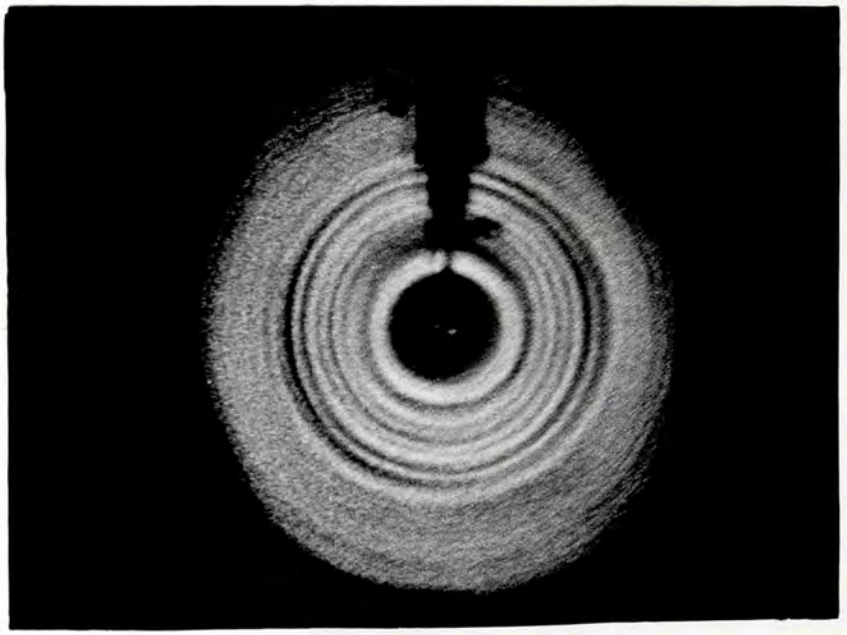

FIGURE 4.28 : Quality of paraboloid

The specular and backscattered spectral results from both aluminium and gold targets are discussed. On some of the 2w spectra, a subsidiary feature was observed at $2w+\delta w$ and remarked upon briefly due to insufficient data, which could only lead to vague conclusions.

In the specular case it was possible to plot a dispersion curve (Figure 4.36). This was achieved by making several microdensitometer traces across the specular spectra at different places, corresponding to different angles, θ, thus different wave-vectors, k, and the shift in the second harmonic was related to a frequency, w, through

$$w = 4w_o\delta\lambda/\lambda_o \qquad (4.8)$$

and wave-vector, $$k = k_o\cos\theta \qquad (4.9)$$

where λ_o, k_o and w_o are the incident radiation's wavelength, wave-vector and angular frequency respectively.

We shall now examine and discuss the results from aluminium and gold targets before making any comparisons. A least squares fit of the results is made wherever possible.

(i) ALUMINIUM TARGETS :

(a) Red Shift

The results for the red shift of the generated second harmonic from its true value are presented in Figs. 4.29(a)&(b) showing its variation with incident intensity and target angle. The backscattered spectra indicate the displacement to be weakly dependent on irradiance[Fig. 4.29(a)] and hardly on the target angle[Fig.4.29(b)]. However, for the specular spectra the reverse was true, i.e. the displacement was independent of irradiance and only weakly dependent on target angle.

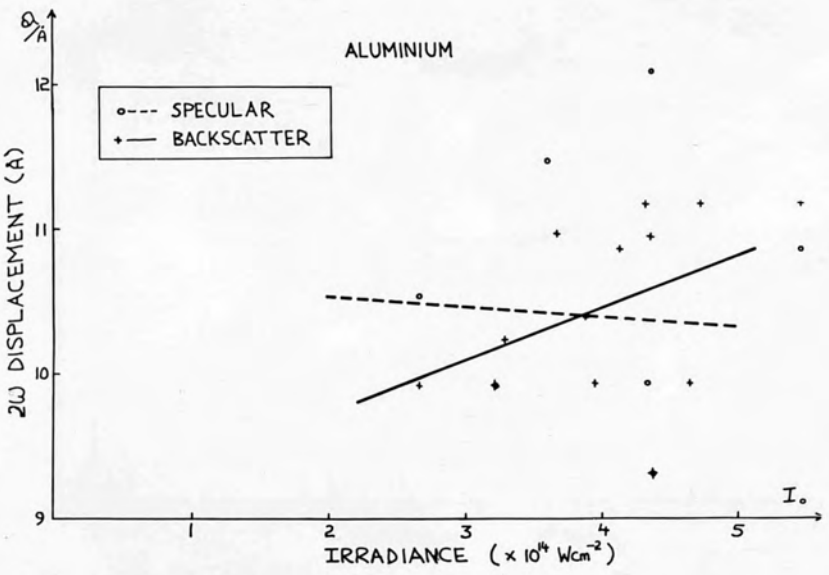

(a)

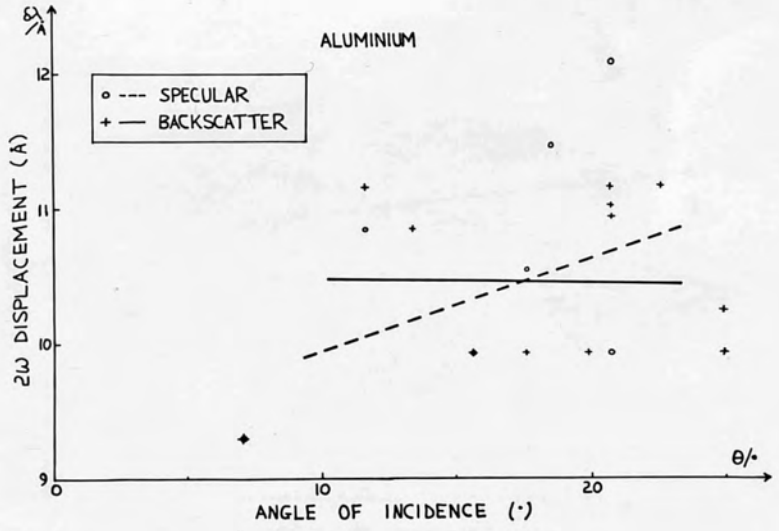

(b)

FIGURE 4.29 : 2W shift wrt (a) irradiance & (b) angle (Al)

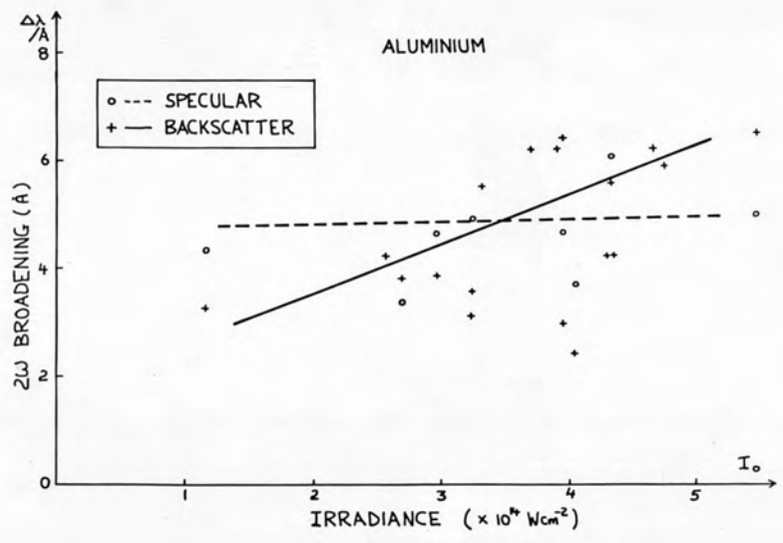

(a)

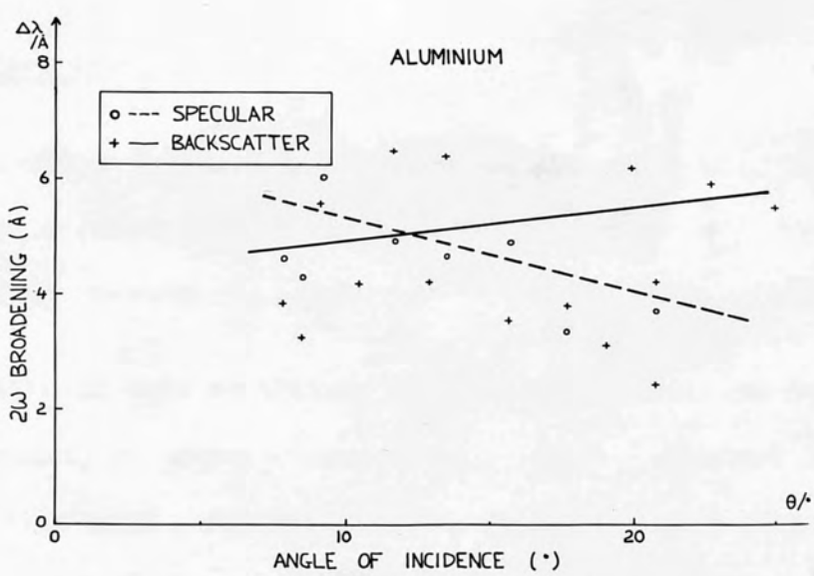

(b)

FIGURE 4.30 : 2W broadening wrt (a) irradiance & (b) angle (Al)

The 2w red shift varied between 9-11 Å which compared well with other experimental works, e.g. Eidmann & Sigel [3]. Using equation(2.70) in §2.5.3, a shift of 10 Å gives a plasma temperature of a few keV where the incident flux is $\sim 10^{14}$ W/cm^2. This compares well with results from Gitomer & Henderson [8] for the irradiance quoted above.

(b) Broadening

The broadening, full width at half maximum(fwhm), of the 2w spectra were measured and plotted versus irradiance and target angle in Figures 4.30(a)&(b) respectively. Again there is little variation of the broadening for either backscatter or specular scatter, with irradiance and target angle. The broadening was in the region of 4-8 Å, for the main feature only, and is of the order of magnitude to those of other researchers, e.g. Eidmann & Sigel [3].

(c) Subsidiary Feature

A subsidiary feature in addition to the main one, was clearly observed, on a number of shots. This was present only in the specular spectra and one example is presented in Figure 4.31.

The shift of this subsidiary feature with respect to the 2w line was measured, where possible, and plotted against irradiance(Fig. 4.32). The data points, indicating the target angles, seem to imply a linear variation with irradiance. Most of the data points lying close to the regression fit in Fig. 4.32 had angles of the same order, though one point corresponding to 7.7° was fairly remote. This implies that a different variation may be expected for diversely different angled targets.

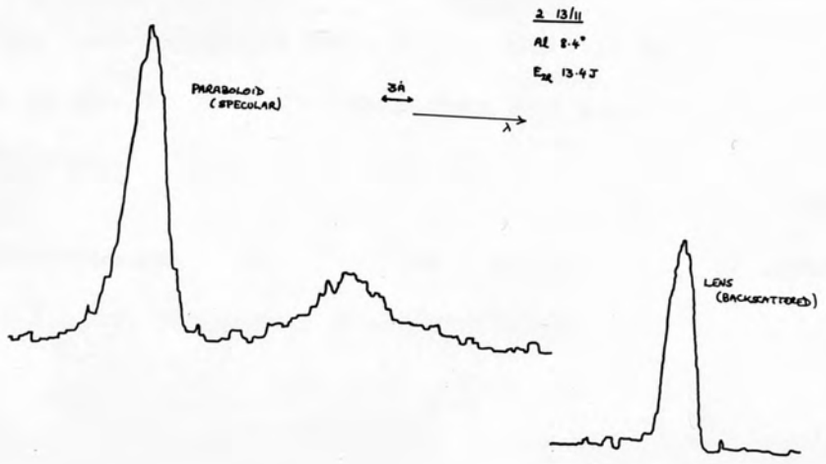

FIGURE 4.31 : Examples of subsidiary feature (Al)

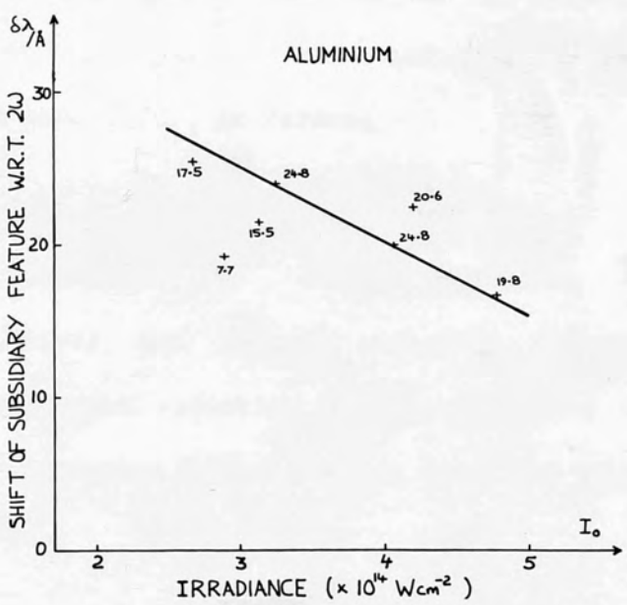

FIGURE 4.32 : Shift variation of subsidiary feature (Al)

(d) Fine Structure

Much fine structure was observed in a number of spectra. Once again it was mostly present in the specular spectra. An example shown earlier in Fig. 4.26 indicated the average spacing, which was mainly to the red side of 2w, to be a few angstroms and gave an asymmetrically broadened spectrum.

A possible explanation of this fine structure has been provided by Cairns (Chap. 2, ref. 37) and is discussed later.

(ii) GOLD TARGETS :

(a) Red Shift

Once again, as with aluminium, both specular and backscatter results for the red shift of 2w shows little variation with irradiance[Fig. 4.33(a)] and target angle[Fig. 4.33(b)]. Here the displacement was in the region of 8-10 Å and gave a plasma temperature of a few keV, from eqn.(2.70), as before.

(b) Broadening

A slow decrease in the broadening with both irradiance[Fig. 4.34(a)] and target angle[Fig. 4.34(b)] for both specular and backscattered radiation was observed. The broadening for both cases was in the region of 4-6 Å which is of the same order as for aluminium.

(c) Fine Structure

Fine structure was observed on a number of results mostly on the backscattered spectra. An example of this is shown in Figure 4.35. The

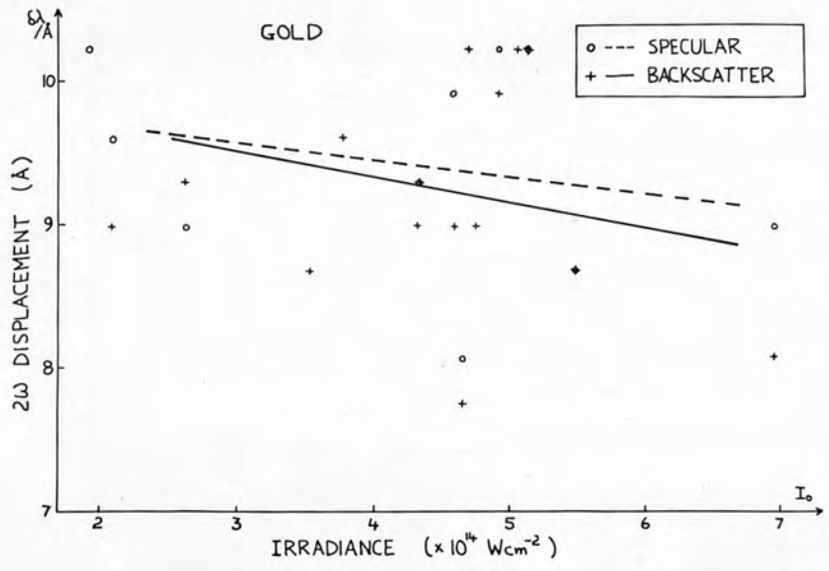

(a)

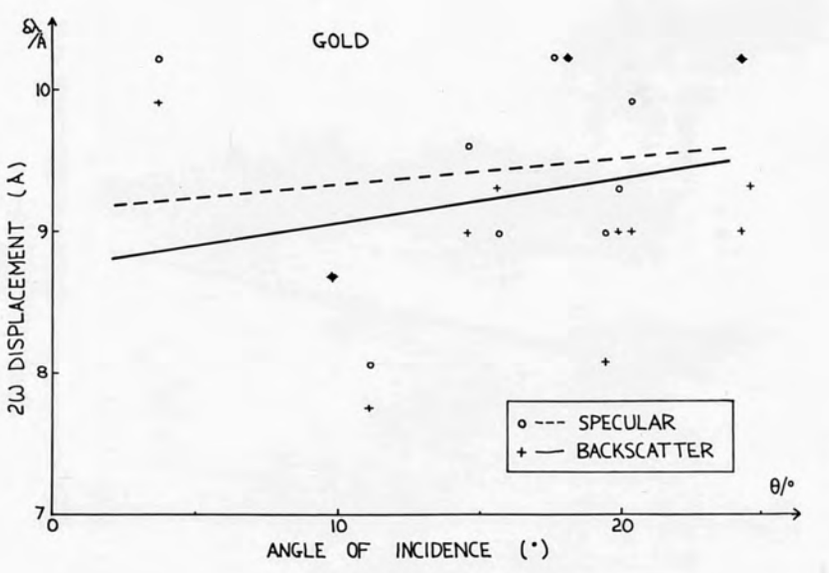

(b)

FIGURE 4.33 : 2W shift wrt (a) irradiance & (b) angle (AU)

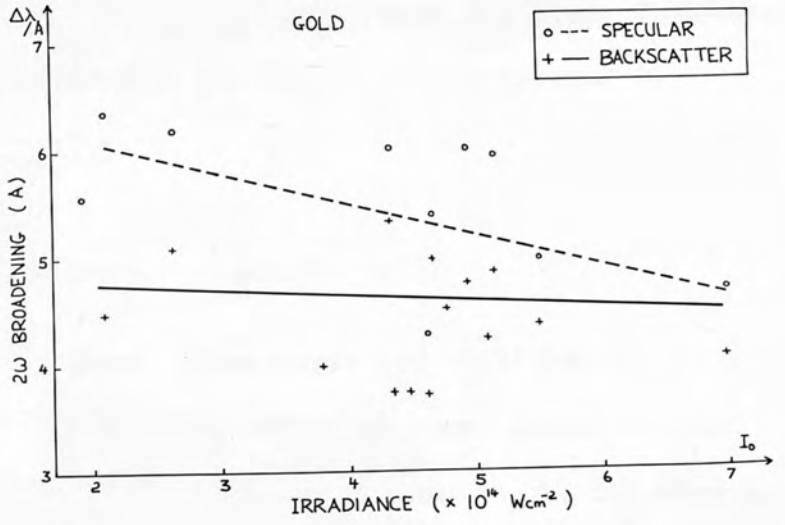

(a)

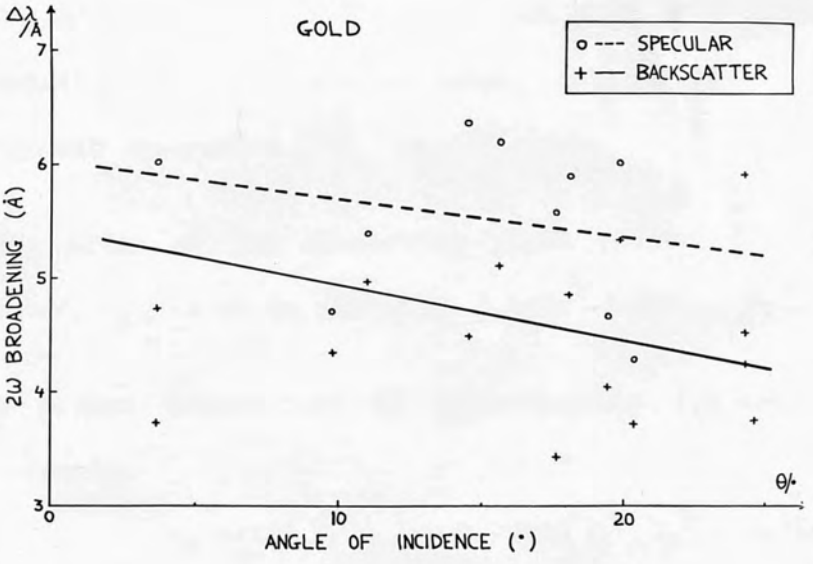

(b)

FIGURE 4.34 : 2W broadening wrt (a) irradiance & (b) angle (AU)

majority of the structure was on the long wavelength side of 2w giving rise to the asymmetric broadening consistent with Cairns theory. The average spacing of the fine structure, from Fig. 4.35, was approximately an angstrom. Summing over all these structures gives the appropriate broadening for 2w. This is examined in the next section (§4.4.3).

(d) Angular Dependence of the Red Shift

For a typical result(shot 11 15/11 Au 9.7°, $I \sim 10^{14}$ W/cm^2), spectrometer scans were taken on the specular image at several positions corresponding to different angles, θ. The displacement of the spectral peak from 2w was related to a frequency, w, through eqn.(4.8) and to a wave-vector, k, through eqn.(4.9). A dispersion curve(w vs. k), from the accumulated results, was then plotted(Fig. 4.36). It was seen that the regression fit had a good correlation coefficient(r=0.8). Three important conclusions could be drawn from the plot:-

(a) The displacement of 2w decreases with increasing angular position on the specular image, arising primarily due to reduced absorption.

(b) The slope of the dispersion curve indicates the ion wave speed, c_s, to be in excess of $3.4*10^8$ cm/sec.

(c) A plasma temperature of approximately 1.5 keV, from the relation,

$$c_s = (ZK_B T_e / m_e) = 9.79*10^5 Z^{1/2} T_e^{1/2} \quad \text{cm/sec} \quad (4.10)$$

where Z is the atomic charge, K_B is Boltzmann constant, m_e is the electron mass and T_e is the plasma temperature in eV.

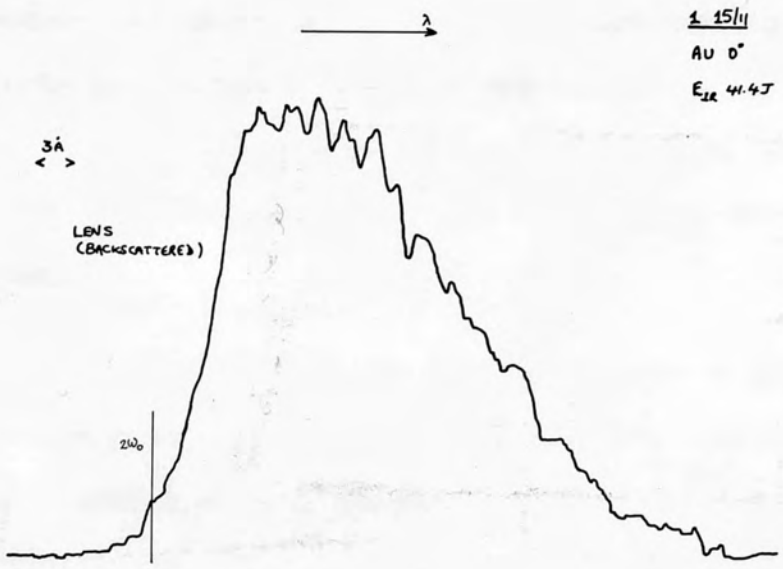

FIGURE 4.35 : Fine structure (AU)

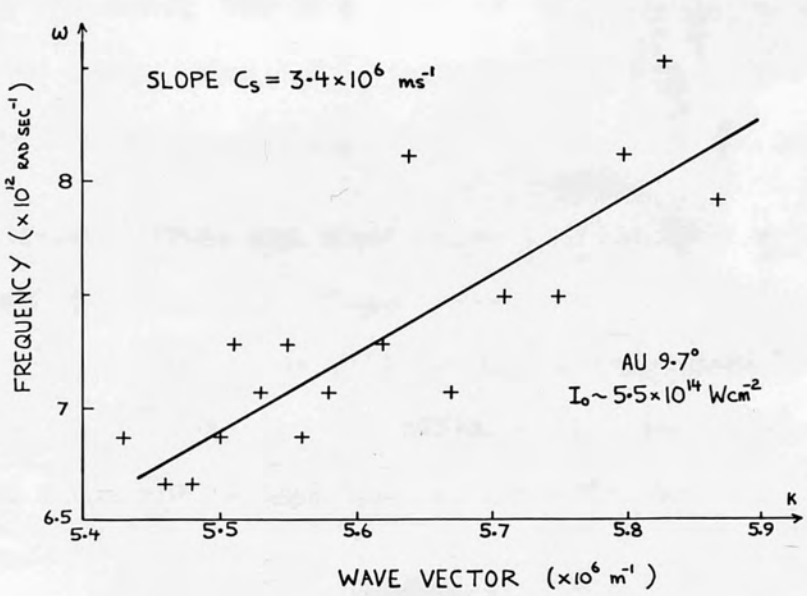

FIGURE 4.36 : Dispersion (w-k) curve

4.4.3 COMPARISONS

The spectral red shift of 2w for both aluminium(A=27,Z=13) and gold(A=197,Z=79) targets was of similar magnitude(9-10 Å), though for gold targets it was an angstrom or so smaller. The slow variation of this shift with irradiance and angle suggests it to be independent of target material, Z.

A smaller shift, observed in the backscattered spectra, was attributed to a blue Doppler shift of $\sim$1 Å resulting from the critical dense surface expanding at $\sim 10^6$ cm/sec.

The relation of the shifts with theories will be discussed later(4.5), though the temperature results of a few keV agree well with those predicted by Gitomer & Henderson(Fig. 2.11) for the irradiances used here.

The 2w broadening was also seen to be insensitive to target, irradiance and angle, being $\sim$5 Å. These results corresponded well with those of other experimenters, e.g. Eidmann & Sigel [3] and Jackel [12].

A subsidiary feature was observed on a number of 2w results from aluminium and gold targets, though fewer in the latter case. For aluminium it was seen that the shift of this feature from 2w decreased linearly with increasing irradiance(Fig. 4.32), for similar angles. However, for gold such a plot was not possible due to insufficient observations.

Fine structure was seen from aluminium and gold targets mostly in the specular and backscattered spectra respectively. The spacing of successive bands was on average one angstrom. A possible explanation of this fine structure has been provided by Cairns (Chap. 2, ref. 37),

where this reflects the coupling with multiple ion-sound waves. From this the ion acoustic frequency was inferred to be $\leqslant 10^{12}$ Hz. Using an approximation, of 0.53 μm(§2.3), for the ion-acoustic wavelength, this revealed a sound speed of $\leqslant 10^{7}$ cm/sec.

4.5 FURTHER DISCUSSION

In this section we shall draw upon results, from both Nd and CO_2 laser produced plasmas, for discussion with the related theories, which were presented earlier in Chapter Two. References to more recent and other relevant papers will be made where necessary.

The SBS results (from 10.6μm radiation only) indicated plasma temperatures of 150-350 eV in the underdense region. This temperature value is smaller, as expected, than that near the critical surface deduced from x-ray data (>2 keV), second harmonic data (~2 keV) and also to the theoretical value of 2-4 keV from Gitomer & Henderson [8], for the irradiances used. The plasma here is essentially subsonic and the spectrum consists of Doppler shifted, backward scattered components. The breadth of this line is interpreted as being due to ion-Landau damping.

Our observations have shown only red shifted spectra whilst some other workers (e.g. Grek [10]) have also seen blue components and fine structure. This is a likely result of blue Doppler shifts from the supersonic plasma being considerable for short duration pulses and smaller wavelengths. No fine structure in CO_2 laser produced plasma could be observed due to the averaging nature of the results. The

temporal variation, seen in the backscatter signals followed closely to that of the mode-locked nature of the CO_2 pulse.

SBS can be enhanced if the ion-sound speed is close to that of the plasma expansion, with reflection directly from the critical surface leading to further amplification of the instability. However, measurements reveals the critical surface front to be slow in comparison to the calculated ion-sound speed, though in the initial stages, $t < 5$nsec, they are likely to be comparable.

In order to explain the experimental results one should also take into account the plasma inhomogeneities and the effect of scattering on the background plasma. Kruer [13] suggests that the turbulence of the ion-sound wave may increase the ion temperature, so increasing Landau-damping of this wave and thus tending to quench the instability. Also, recent calculations by Manheimer & Colombant [15] and Gorbunov [9] show that a steep gradient in the plasma is effective in reducing the level of backscatter (c.f. optical results, Fig. 4.13).

The backscatter is strong due to the relatively long (~50 nsec) pulse giving large density scale-lengths. Our results indicate in excess of 50% (<65%) reflection losses. For shorter pulses (weak scale-lengths), lower backscatter levels are expected, as in Nd systems [2]. Reduction of these losses is a definite pre-requisite for inertial compression.

The fraction of incident light, that was backscattered, measured as a function of the incident irradiance (Fig. 4.1) is expected to saturate at higher irradiance [2]. This is as a result of ion trapping and wave breaking because with $T_e \simeq T_i$ the large-amplitude ion wave will have a phase velocity very close to the ion thermal speed. Mitchel et

al [18] suggests that plasma regions of strong ion acoustic density fluctuations, produced by Brillouin scatter, can also be areas of frequency upconversion, viz. 2w, 3w, etc..

The variation of $I_{2\omega}$ with angle of incidence was investigated on carbon targets (Fig. 4.9) irradiated with CO_2 radiation. As 2w occurs at the critical surface one expects it to reveal the nature of resonance absorption for the incident p-polarised laser radiation. Using the theory in §2.2.2, plasma density scale-lengths of 20 μm, 150 μm and greater are inferred. These were shown [23] to exist at different stages of plasma development.

Rippling of the critical surface can arise due to a turbulence above n_c(observed by Sudera [23]) and by intensity variations in the focal plane. This can then lead to increased absorption and better conversion to 2w due to the close relationship of resonance absorption and harmonic generation (§2.2.2 & §2.5). The resonance process is linear so the second harmonic intensity is expected to be proportional to I_0^2. However, observations show the exponent to be 2.3 and 2.4 for molybdenum and carbon respectively (Fig. 4.10). This is due to the density scale-length varying and with it the angle for optimum resonance absorption. This may be evidence of a contribution to 2w by the parametric processes such as the ion acoustic decay instability. Note that the reflectivity was lower for carbon then for molybdenum targets, which implies the gradient scale-lengths to be shorter for the latter and thus resonance far more pronounced than inverse bremsstrahlung as an effective absorption mechanism (§2.2).

The second harmonic spectra from a neodymium laser produced plasma on aluminium and gold targets were analysed. The observed spectra had much fine structure with spacings of 1-2 Å (Fig. 4.26), were

asymmetrically (>5 Å) broadened and the peak was shifted by 10 Å. This was consistent with Cairns explanation as arising from the interaction of a resonantly excited large amplitude electron plasma wave with an ion sound wave to produce discrete side-bands with the observed spacing. The spacing of the side-bands, average interval of an angstrom, gives rise to the broadened and shifted spectrum. The spacing also gives an indication of the ion-acoustic frequency and thus the temperature (2.64) which are lower then expected due to several factors, such as plasma motion, profile steepening due to ponderomotive forces, parametric effects, etc. being ignored.

Due to the averaging nature of results for 2w, in the case of CO_2 laser produced plasmas, any fine structure, even if present, would not be observed. The temporal behaviour of 2w, seen in CO_2 plasma, also reflected the mode-locked nature of the incident laser radiation. Within this temporal variation two or more distinct peaks were often observed (Fig. 4.4). This is likely to be a result of changes in the scale-length as the intervals are close to those seen in the optical data (Fig. 4.14), which again proves that several scale-lengths are probable within the plasma's lifetime. The shift and broadening were both in the region of 75 Å. However, here the conversion to $I_{2\omega}$ was estimated to be 10^{-5} and 10^{-6} for molybdenum and carbon targets respectively. This was comparable to those measured by other workers, e.g. Eidmann & Sigel [3]. A lower conversion efficiency results for carbon targets as it has long scale-lengths implying poor resonance absorption.

Figures 4.37 & 4.38 show theoretical plots for the plasma scale-length versus the second harmonic displacement for various plasma temperatures at both Nd and CO_2 laser wavelengths. The graphs indicate

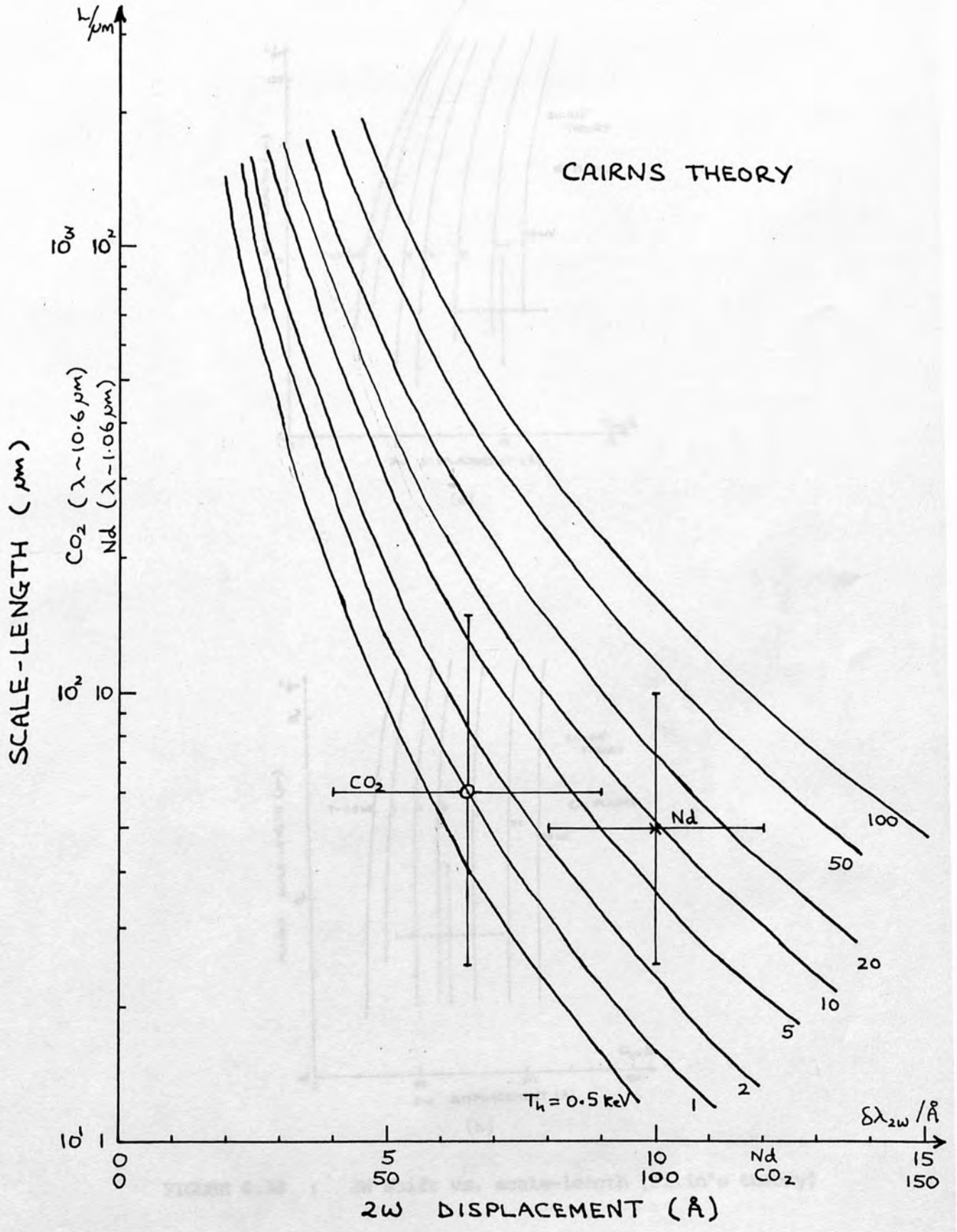

FIGURE 4.37 : 2W shift vs. scale-length (Cairns theory)

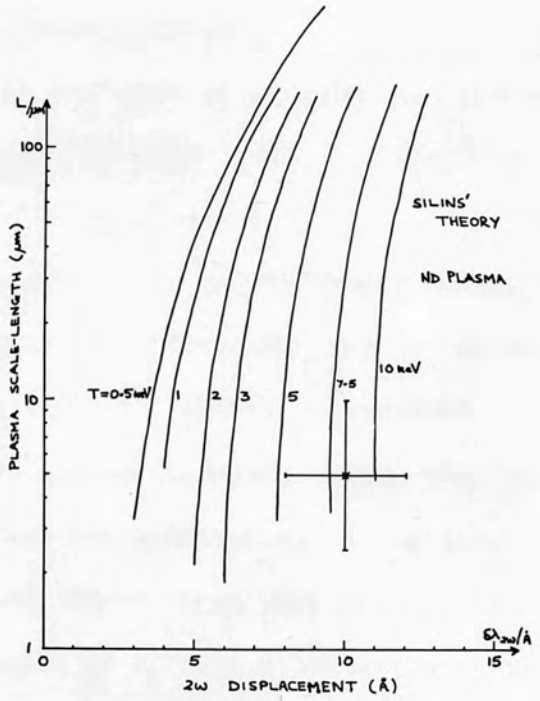

(a)

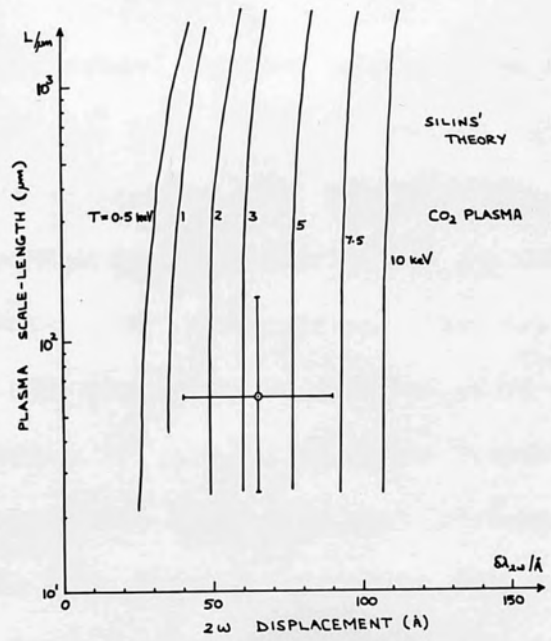

(b)

FIGURE 4.38 : 2W shift vs. scale-length (Silin's theory)

the experimental regions covered in this study. The former figure is taken from Cairns theory (**$2.5.2**) whilst the latter is from Silin's theory (**$2.5.3**). In the case of a neodymium system, such as RAL, the scale-length was given by [20]

$$L = (I_0/3.0*10^{13})^{0.16} \qquad (4.11)$$

where I_0 is the irradiance in W/cm^2. Thus a plasma density scale-length of a few microns was inferred for the irradiances used in the Nd system. In Silin's case the plasma temperature is basically dependent on the shift of the second harmonic rather than the scale-length; c.f. Cairns theory implies the temperature to be strongly dependent on both the scale-length and shift. From just knowing the shift of 2w one can obtain a good estimate of T_h from Silin whilst with Cairns one requires the scale-length to a far greater accuracy. However, both theories give estimates of plasma temperature in the region of 8 keV & 2 keV for Nd and CO_2 laser generated plasmas respectively, again confirming earlier results.

Finally, if the second harmonic displacement is plotted against the scaling parameter $I\lambda^2$ (Fig. 4.39), it shows a definite correlation, indicating the shift to decrease with $I\lambda^2$, i.e. the displacement of the second harmonic spectrum approaches twice the incident frequency, with increasing irradiance. The above result has yet to be explained quantitatively, though the following factors ought to be noted; i.e. with higher irradiances the spectra do become broader and consequently the structure gets confused, leading to less pronounced spectral peaks. Extrapolation of the data implies zero shift for the second harmonic at $I\lambda^2$ of $6*10^{14}$ $Wcm^{-2}\mu m^2$. What happens at this value? Well, it is obvious that ion saturation occurs and that other non-linear processes become dominant [11]. The hot-electron temperature plot on the same figure (also Fig. 2.11) implies T_h of 1-3 keV for CO_2 generated plasma

and 3.5-5 keV for Nd produced plasma as indicated before. However, if the second harmonic radiation shift is assessed with the laser intensity it is seen that Cairns theory reflects more closely the measured experimental results for both Nd and CO_2 laser produced plasmas (Figure 4.40). But Silins' results show insensitivity to the type of radiation and once again reveal clearly its temperature dependence, indicating Cairns description of events to be more representative.

Any discrepancies that exist between theory and experiment are due to instabilities and effects ignored in order to simplify the calculations. Undoubtedly, any good candidate theory would have to include not only other effects, but also consider effects that compete with each other and interaction-interaction processes. Only then can one be in a position to determine the necessary parameters for efficient absorption in plasmas — the goal to nuclear fusion.

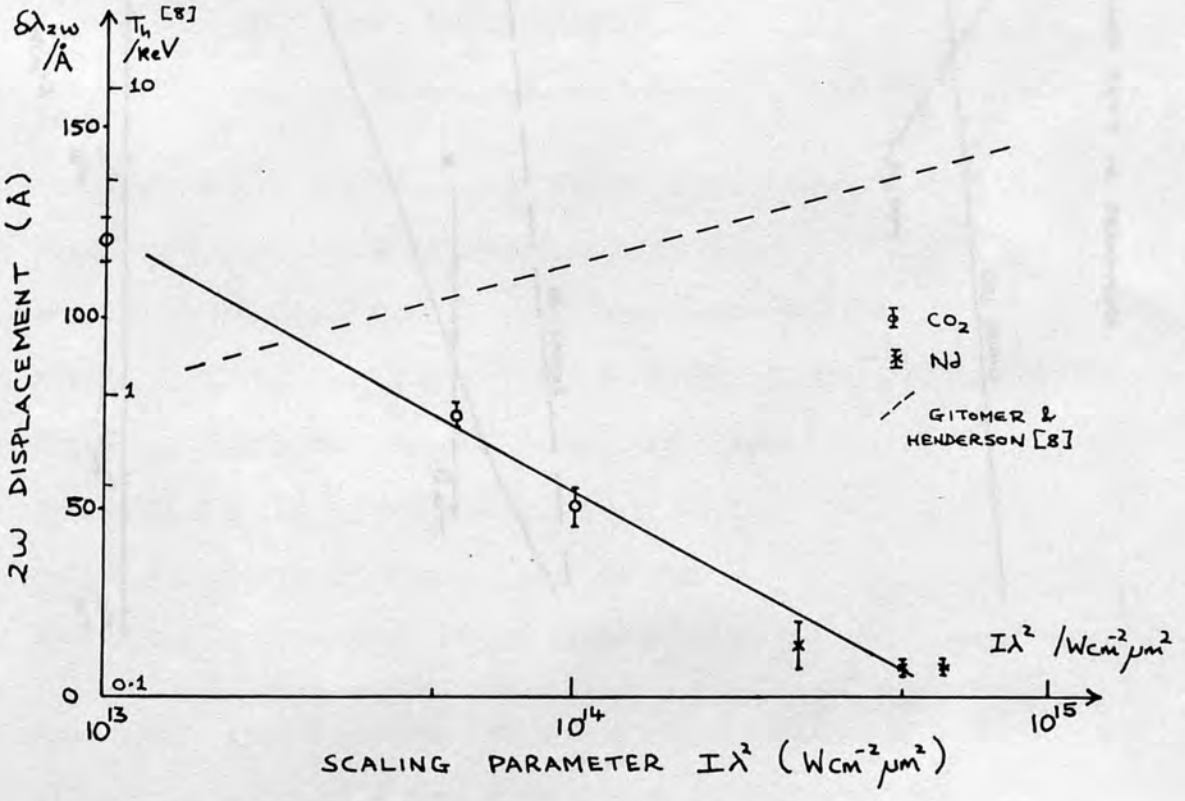

FIGURE 4.39 : 2W shift vs. scaling parameter $I\lambda^2$

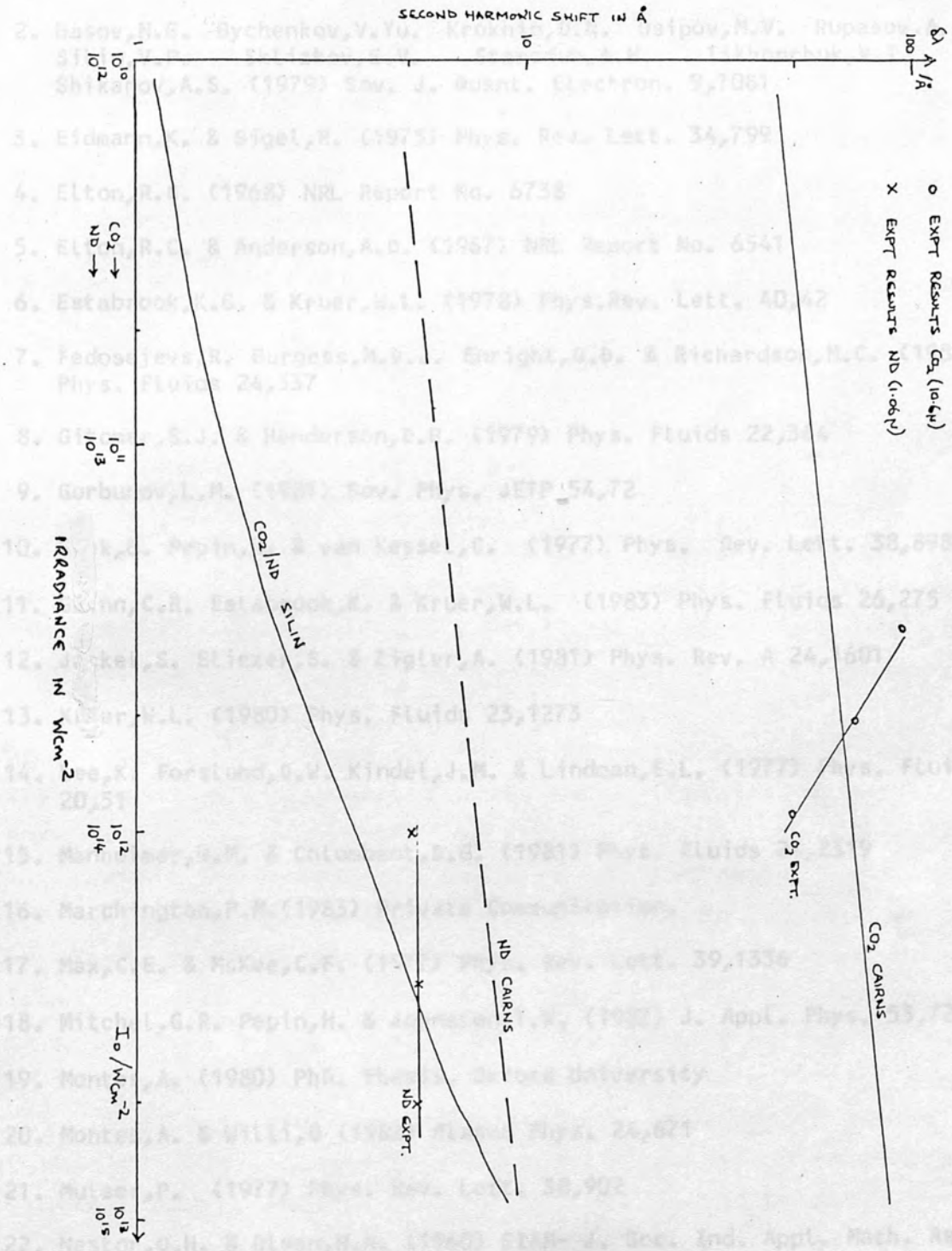

FIGURE 4.40 : SECOND HARMONIC SHIFT VS. IRRADIANCE.

REFERENCES :

1. Baker,L. (1983) Phys. Fluids **26**,391

2. Basov,N.G. Bychenkov,V.Yu. Krokhin,O.N. Osipov,M.V. Rupasov,A.A. Silin,V.P. Sklizkov,G.V. Starodub,A.N. Tikhonchuk,V.T. & Shikanov,A.S. (1979) Sov. J. Quant. Electron. **9**,1081

3. Eidmann,K. & Sigel,R. (1975) Phys. Rev. Lett. **34**,799

4. Elton,R.C. (1968) NRL Report No. 6738

5. Elton,R.C. & Anderson,A.D. (1967) NRL Report No. 6541

6. Estabrook,K.G. & Kruer,W.L. (1978) Phys.Rev. Lett. **40**,42

7. Fedosejevs,R. Burgess,M.D.J. Enright,G.D. & Richardson,M.C. (1981) Phys. Fluids **24**,537

8. Gitomer,S.J. & Henderson,D.B. (1979) Phys. Fluids **22**,364

9. Gorbunov,L.M. (1981) Sov. Phys. JETP **54**,72

10. Grek,B. Pepin,H. & van Kessel,C. (1977) Phys. Rev. Lett. **38**,898

11. Gwinn,C.R. Estabrook,K. & Kruer,W.L. (1983) Phys. Fluids **26**,275

12. Jackel,S. Eliezer,S. & Zigler,A. (1981) Phys. Rev. A **24**,1601

13. Kruer,W.L. (1980) Phys. Fluids **23**,1273

14. Lee,K. Forslund,D.W. Kindel,J.M. & Lindman,E.L. (1977) Phys. Fluids **20**,51

15. Manheimer,W.M. & Colombant,D.G. (1981) Phys. Fluids **24**,2319

16. Marchington,P.M.(1983) Private Communication.

17. Max,C.E. & McKee,C.F. (1977) Phys. Rev. Lett. **39**,1336

18. Mitchel,G.R. Pepin,H. & Johnston,T.W. (1982) J. Appl. Phys. **53**,7274

19. Montes,A. (1980) PhD. Thesis, Oxford University

20. Montes,A. & Willi,O (1982) Plasma Phys. **24**,671

21. Mulser,P. (1977) Phys. Rev. Lett. **38**,902

22. Nestor,O.H. & Olsen,H.N. (1960) SIAM- J. Soc. Ind. Appl. Math. Rev. **2-3**,200

23. Sudera,Y.S. (1983) Private Communication.

24. Virmont,J. Pellat,R. & Mora,A. (1978) Phys. Fluids **21**,567

CONCLUSIONS

In the course of this work it has been possible to describe several of the physical processes occurring in dense plasmas which have been produced by high power lasers. Measurements have been made of the spectrum emitted when the plasma is irradiated by an electromagnetic wave of frequency, w_o.

It has been shown that light is scattered:-

(a) at a frequency slightly less than w_o by the stimulated Brillouin scattering process.

(b) at a frequency slightly less than $2w_o$ as a result of a harmonic generation process occurring near the critically dense region. The radiation is the result of coalescence of a plasmon and a photon or the coalescence of two plasmons.

The stimulated Brillouin scattering process, dependent on the existence of an ion acoustic wave, whose frequency depends on temperature, has been useful in the context of this study as a diagnostic. The wavelength shift of the scattered radiation has been used to make an independent estimate of plasma temperature (4.4) once the plasma velocity was known from shadowgram measurements [3]. The plasma temperatures deduced (from the Brillouin shifted spectrum) in the underdense region were between 150 and 350 eV for CO_2 radiation and were comparable to those obtained by other workers (Paragraph 2.3). The temperature is expected to be much higher in the vicinity of the critically dense region due to increased absorption via resonance and parametric processes. The second harmonic is generated in the critically dense region. Also X-ray intensities are dependent on plasma density. Hence these two processes provide a means of determining temperatures in the denser plasma. For plasmas produced by CO_2 laser radiation, temperatures of approximately 2keV are found by both techniques. These agree, within $\pm$ 15% with those derived by Gitomer & Henderson shown in figure 2-11.

The original contributions to our understanding of the second harmonic consist of measurements of the red shift, measurements of the relative intensity, the observation of a fine structure within the second harmonic spectrum and the detection of a subsidiary feature red shifted by 0.1 μm for CO_2 laser radiation [1] and by 20Å for Nd laser radiation.

There is fine structure within the main envelope of the second harmonic spectrum obtained with Nd laser radiation. This has a spacing of 1.0 $\pm$ 0.5 Å as may be seen in Figure 4.26. A calculation of the value expected from Cairn's theory for a plasma temperature of 1.5 keV and scale-length of 3.5μm was one Angstrom. In view of the error of measurements, which were $\pm$8%, and the existence of outward motion of the plasma at 10^6 cm.sec^{-1}, giving a Doppler shift of about 0.5Å, the experimental values provide support for Cairn's theory.

A diffuse spectrum was found in the vicinity of the second harmonic where the displacement of $2w_o$ decreases with increasing angle from normal incidence. This spectrum, shown in figure 4.31 appears not to have been reported previously.

There is a linear relationship between the frequency and wave vector (2.39) as may be seen in Fig. 4.36 and which is attributed to the presence of an ion wave whose speed is in excess of 10^7 cm.sec^{-1}

The method of measurement of the 2w spectrum produced by the CO_2 laser caused the fine structure to be integrated over approximately 80 laser shots. As a consequence, detail is lost in those spectra but the shoulder seen in figure 4.3 could be attributed to the fine integrated structure.

In figure 4.39 it was seen that the displacement of the second harmonic spectrum from $2w_o$ was a logarithmic function of the scaling parameter $I\lambda^2$ for plasmas produced by either CO_2 lasers or Nd lasers, i.e.

$$\delta\lambda_{2w} = b \log (I\lambda^2) \qquad (5.1)$$

where $b = 67.5AW^{-1}$. Relation (5.1) is valid for $I\lambda^2 > 10^{12} Wcm^{-2}\mu m^2$ which is above threshold for 2w generation.

In figure 4.40 it may be seen that the spectral shift of the second harmonic is predicted by Cairn's theory to within 20% but the theory of Silin leads to a discrepancy of more than an order of magnitude. This agreement provides support for the ion wave frequency to be correlated with the incident intensity. It also appears that parametric resonance is not the dominant process as required by Krokhin (2.70). The experimentally determined second harmonic spectral shift did not vary greatly with irradiance for neodymium produced plasmas and according to Cairn's theory, the variation should be no more than ±2Å over the intensity range 10^{12} to $10^{13} Wcm^{-2}$. However, in the CO_2 case the experimental values of the 2w shift fell steeply in the range 10^{11} to 10^{12} Wcm^{-2} whereas Cairn's theory predicts a slight rise. The effect of a Doppler shift is negligible here being less than 0.5Å, and does not account for the decreasing shift in the second harmonic with irradiance.

An alternative explanation is given by Burgess [2] who argues that the generating mechanism could be the combination of an instability of resonance absorption, which is due to fluctuations in the density gradient, and wave-breaking.

Burgess [2] has also observed a second harmonic spectral red shift which decreases with increasing irradiance for Nd illumination. The extrapolation in figure 4.39 leads to a threshold value of 10^{15} Wcm^{-2} μm^2, for zero red shift. It is expected at these high irradiances that the dominant absorption mechanism is via turbulent wave-breaking; Sudera [3] has shown the existence of turbulence in the critically dense region by shadowgraphic and interferometric techniques.

The subsidiary feature which appears on the long wavelength side of the 2w harmonic at a position of about +0.1μm with the CO_2 laser and at 20Å for the Nd laser appears not to have been reported elsewhere. Neither Cairn's (Fig.4.37) nor Silin's (Fig 4.38) theories account for this subsidiary feature. Several possible causes have been considered. It has been shown that there are two density gradients in the plasma and hence two scale-lengths. These could lead to the generation of plasmons of different energies (for CO_2 radiation), and

hence lead to two features in the harmonic spectrum, separated by no more than 80Å assuming that the plasma temperature remains fairly constant. Similarly for Nd plasmas a discrepancy of no more than 4Å is expected. Thus several scale-lengths do not account for the subsidiary feature but do offer another explanation of the shoulder seen in CO_2 results (Fig.4.3) and the assymetry seen in 2w spectra for Nd plasmas. Yet another possibility is the existence of resonance and parametric processes which compete to produce the Langmuir waves needed to generate the second harmonic. The electromagnetic wave penetrates to different depths within the plasma as given by the Ginzburg function (φ), Fig 2.4, which also gives an optimum incident angle for maximum resonance absorption. It is noted that the subsidiary feature occurs for Nd illumination where the targets were tilted by at least 15° to the incident direction, indicating resonance absorption to be the dominant process. In these experiments the density scale length was 1.5μm. However, Abdel-Raouf [1] saw a similar effect for CO_2 illumination but with plane targets normal to the incident beam. Here the parametric process is likely to be dominant as the longitudinal wave amplitude is at a maximum along the electric field intensity vector of the incident radiation. In the present study it is concluded that resonance absorption, once again, is dominant for CO_2 generated plasmas (Fig.4.9) with a minimum scale-length of 20μm.

In the resonant region near to the critical density, large magnetic fields are generated Ref. [4]. The magnetic fields must be in excess of 10^6 gauss to give the observed shift in the subsidiary feature arising from cyclotron radiation. In this study, magnetic fields are about a megagauss [1] which would result in a cyclotron frequency of the order of 10^{12} Hz. This could account for the observed subsidiary feature. It is noted that generally magnetic fields are below a megagauss for the irradiances used and are only important in thermal energy transport processes within the plasma.

The scaling factor for the second harmonic intensity with irradiance is between $I^{2.3}$ and $I^{2.4}$, indicating that apart from resonance processes there were contributions by parametric and other processes. The fractional conversion to the second harmonic was 10^{-6} to 10^{-5} of

the incident radiation, well within the range 10^{-6} - 10^{-3} determined by several workers (see refs. 50, 60, 144, 153 in Chapter 2). This fraction is calculated from thresholds and growth rates of the processes from which 2w can arise. For lower atomic charge targets the conversion to 2w was reduced, being 10^{-6} of incident radiation, due to the ion acoustic frequency scaling as $Z^{\frac{1}{2}}$ and larger scale-lengths [3] leading to poor resonance absorption and consequently less second harmonic generation.

To summarise, the above study has given insight into some of the processes which take place when intense laser light is incident on a plasma and which may lead to absorption or scattering of the light. However, much more work is required. An increased range of target materials should be examined, and a broader range of incident radiation wavelength and at higher intensities be used. For CO_2, radiation, improved beam uniformity and use of faster array-type detectors is necessary to obtain time-resolved spectra for direct comparison with plasmas produced by shorter wavelength radiation. Future studies should be made of the processes at higher values of $I\lambda^2$ i.e. above $10^{16} Wcm^{-2}\mu m^2$ where non-linear effects are expected to dominate. At even higher values, $I\lambda^2 > 10^{17} Wcm^{-2}\mu m^2$, relativistic processes become important and novel effects will occur due to the intense magnetic fields having a more pronounced effect on the motion of electrons.

REFERENCES

1. Abdel-Raouf, W.S.(1980) Ph.D. Thesis, Univ. of London.
2. Burgess, M.D.J. Dragila, R & Luther-Davies, B (1984). Optic.Communc.50, 236
3. Sudera, Y. (1983) Private communication.
4. Stamper, J.A. & Tidman D.A. (1973) Physics Fluids, 16, 2024.

APPENDIX A : CO_2 LASER THEORY

INTRODUCTION:

In 1964 Patel [3] succeeded in obtaining low infrared emission from CO_2 gas by exciting the gas in a dc electric discharge. Subsequently higher lasing efficiencies were reported by additions of N_2 and He gases, to the CO_2 discharge, which play significantly different roles. The N_2, acting as an energy storage, efficiently transfers energy to the CO_2 molecule. The He encourages the lower CO_2 levels to depopulate though on a smaller time scale with respect to the N_2-CO_2 gas mixture.

Pulsed CO_2 lasers have been developed from long, narrow discharge tubes containing only a few torr of the gas mixture to large transversely excited atmospheric pressure(TEA) lasers. Power levels of greater than gigawatts(GW) have been achieved with such lasers.

LASER MECHANISM :

The CO_2 laser operates in the 9-11 μm band in the infrared. The laser transitions arise in the change of vibrational levels which are shown in Fig. A.1. The three fundamental modes are designated ν_1, ν_2 and ν_3 representing the symmetric, bending and asymmetric modes respectively. In the symmetric case of frequency ν_1, the two oxygen atoms move in opposite direction whilst the carbon atom is stationary. The asymmetric mode of frequency ν_3 has the O atoms moving together while the carbon moves in the opposite direction. Lastly, the bending mode with frequency ν_2 consists of two degenerate vibrations perpendicular to and within the plane of paper(Fig. A.1).

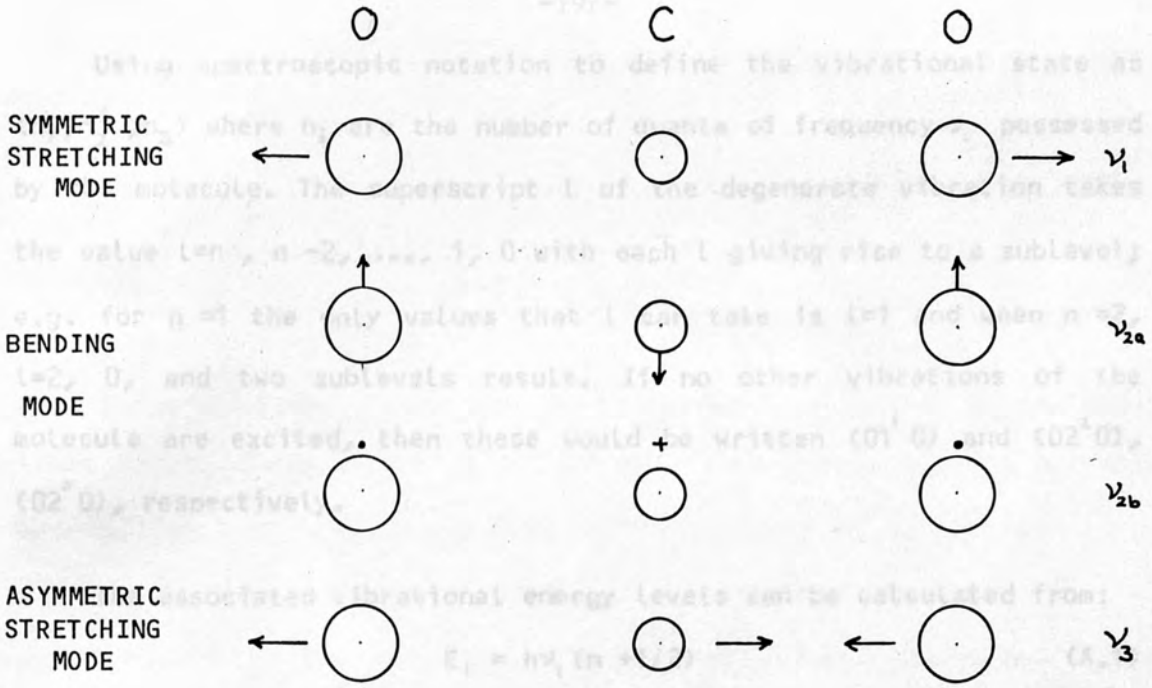

FIGURE A.1 : Normal vibrations of CO_2 molecule [1].

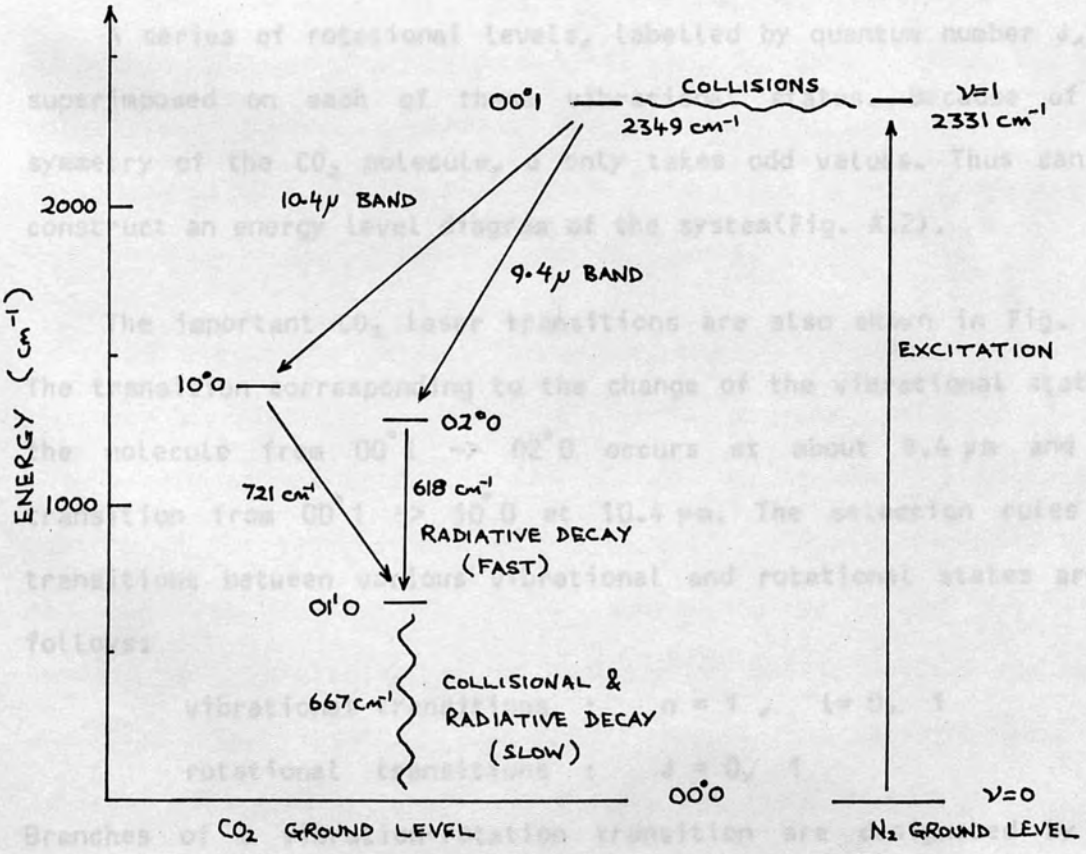

FIGURE A.2 : Energy level diagram for CO_2 and N_2.

Using spectroscopic notation to define the vibrational state as (n_1, n_2^{ℓ}, n_3) where n_i are the number of quanta of frequency ν_i possessed by the molecule. The superscript l of the degenerate vibration takes the value $l=n, n-2, \ldots, 1, 0$ with each l giving rise to a sublevel; e.g. for $n=1$ the only values that l can take is $l=1$ and when $n=2$, $l=2, 0$, and two sublevels result. If no other vibrations of the molecule are excited, then these would be written $(01^1 0)$ and $(02^2 0)$, $(02^0 0)$, respectively.

The associated vibrational energy levels can be calculated from:

$$E_1 = h\nu_1 (n + 1/2) \qquad (A.1)$$

$$E_2 = h\nu_2 (n + 1) \qquad (A.2)$$

$$E_3 = h\nu_3 (n + 1/2) \qquad (A.3)$$

A series of rotational levels, labelled by quantum number J, are superimposed on each of these vibrational states. Because of the symmetry of the CO_2 molecule, J only takes odd values. Thus can now construct an energy level diagram of the system(Fig. A.2).

The important CO_2 laser transitions are also shown in Fig. A.2. The transition corresponding to the change of the vibrational state of the molecule from $00^0 1 \rightarrow 02^0 0$ occurs at about 9.4 μm and the transition from $00^0 1 \rightarrow 10^0 0$ at 10.4 μm. The selection rules for transitions between various vibrational and rotational states are as follows:

vibrational transitions : $n = 1$, $l = 0, 1$

rotational transitions : $J = 0, 1$

Branches of a vibration-rotation transition are designated by the change in J as follows:

$$P = \Delta J = -1, \quad Q = \Delta J = 0, \quad R = \Delta J = +1,$$

with individual lines being denoted by P(J), Q(J), R(J).

In the 10.4 μm band, oscillation occur primarily on the P(18), P(20) and P(22) lines near 10.6 μm. Figure A.3 shows the important spectral lines on which laser emission can occur in CO_2, where the height of the line is proportional to its strength thus giving an indication of their relative gain in the laser.

The separation between the first excited level(ν=1)of N_2 and $00^{0}1$ level of CO_2 is only ~18 cm^{-1} (1/400 eV). Thus energy between $N_2(\nu=1)$ and $CO_2(00^{0}1)$ is transferred with high efficiency as N_2 collides with CO_2 because the energy discrepancy is much less than the thermal energy of molecules in the discharge(~200 cm^{-1} at 300 K). After the laser action in the $He:CO_2:N_2$ mixture the CO_2 molecules quickly decay to the $(01^{1}0)$ vibrational mode where, if helium were not present, they would be trapped. The rate equations for the various relaxation processes have been calculated by Taylor & Bittermann [4] which augment the above discussion. Another important result that follows from the rate equations is that the rotational relaxation rate is very large implying efficient operation of short pulse CO_2 lasers.

The excitation schemes available are either optical, chemical, thermal or electrical though the last is most frequently used. Essentially an electric discharge is applied to the gas mixture and pumping of the laser levels occurs by collisions between electrons in the discharge and the CO_2 and N_2 molecules. In pulsed TEA lasers, however, a uv-preionisation is employed to obtain uniform discharges and high laser outputs. Conversion efficiencies of ~10% have been achieved with such systems, c.f. theoretical limit of ~40%.

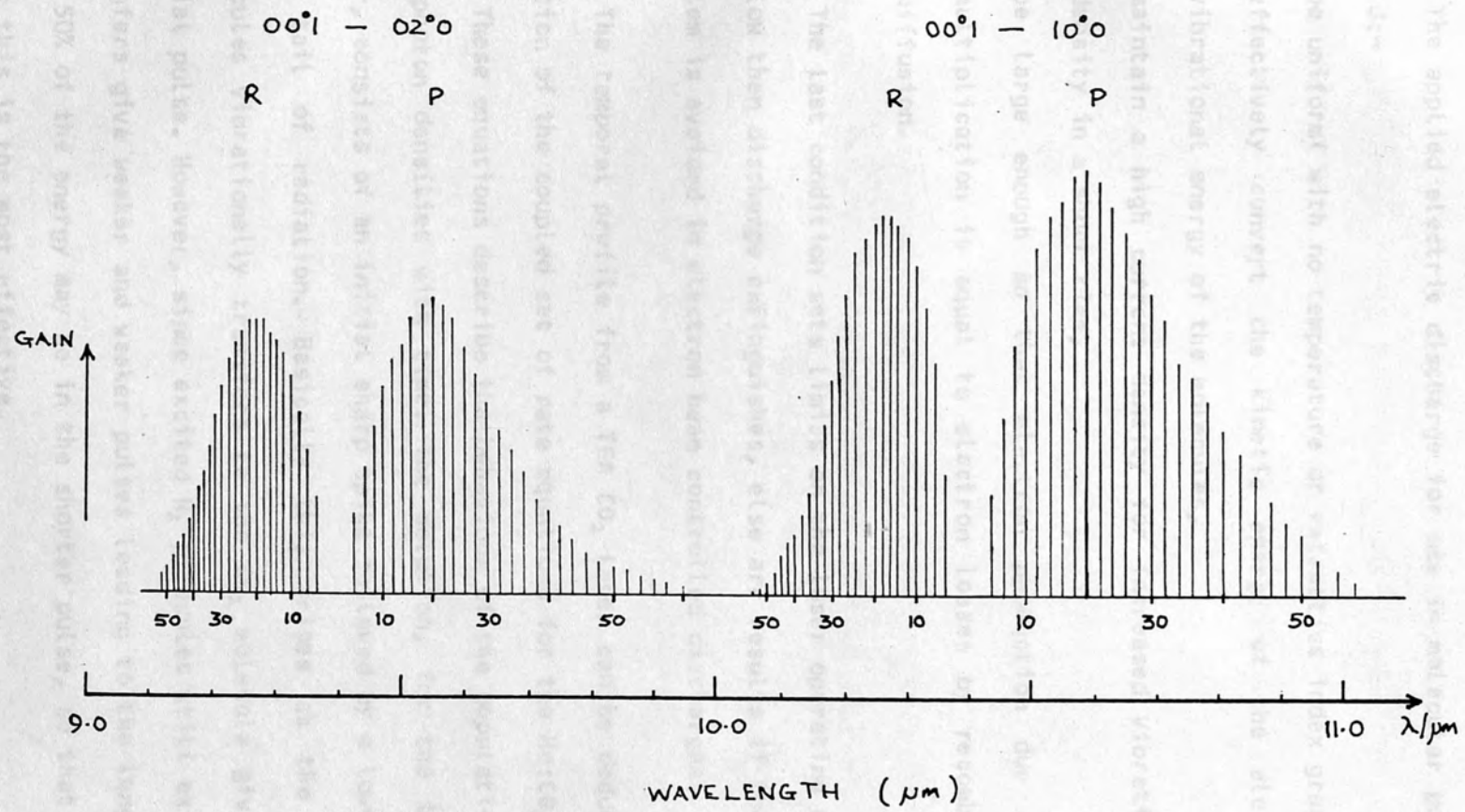

FIGURE A.3 : CO_2 spectrum

PULSED CO_2 LASERS :

The applied electric discharge for use in molecular pulsed lasers should:-

(a) be uniform(with no temperature or refractive index gradients),

(b) effectively convert the kinetic energy of the electrons into vibrational energy of the molecules,

(c) maintain a high current density for increased vibrational energy density in a short time,

(d) be large enough so that electron production due to Townsend multiplication is equal to electron losses by recombination and diffusion.

The last condition sets limits on the laser operating voltages; if too low then discharge extinguishes, else arc results if too high. This problem is avoided in electron beam controlled discharges.

The temporal profile from a TEA CO_2 laser can be deduced from the solution of the coupled set of rate equations for the $He:CO_2:N_2$ mixture [2]. These equations describe the behaviour of the population densities and photon densities with time. The solution, for the laser output power, consists of an initial sharp spike followed by a lower intensity long tail of radiation. Basically this arises as the excited N_2 molecules vibrationally transfers to the CO_2 molecule giving a rapid initial pulse. However, since excited N_2 molecules still exist, further transfers give weaker and weaker pulses leading to the long tail. More than 50% of the energy may be in the shorter pulse, so that in terms of power this is the most effective.

See Duley [1] for further reading on CO_2 lasers and more references.

REFERENCES :

1. Duley,W.W. (1976) " CO_2 Lasers " Academic Press, New York (USA)
2. O'Neill,F. (1976) " High Power Pulsed CO_2 Lasers " RAL Report
3. Patel,C.K.N. (1964) Phys. Rev. Lett. **12**,588
4. Taylor,R.L. & Bitterman,S. (1969) Rev. Mod. Phys. **41**,26

APPENDIX B : FILTERS

The spectral response of the filters used in this study are shown in Figure B.1; viz. 10.69 μm, 7.07 μm, 5.3 μm filters. Also their performance details are presented below in Table B.1

TABLE B.1 : FILTER CHARACTERISTICS.

Filter	10.69	7.07	5.3	μm
Diameter	25	25	20	mm
Peak wavelength	10.69	7.0	5.3	μm
Half peak bandwidth	0.195	2.3	0.6	μm
Transmission	40	50	80	%

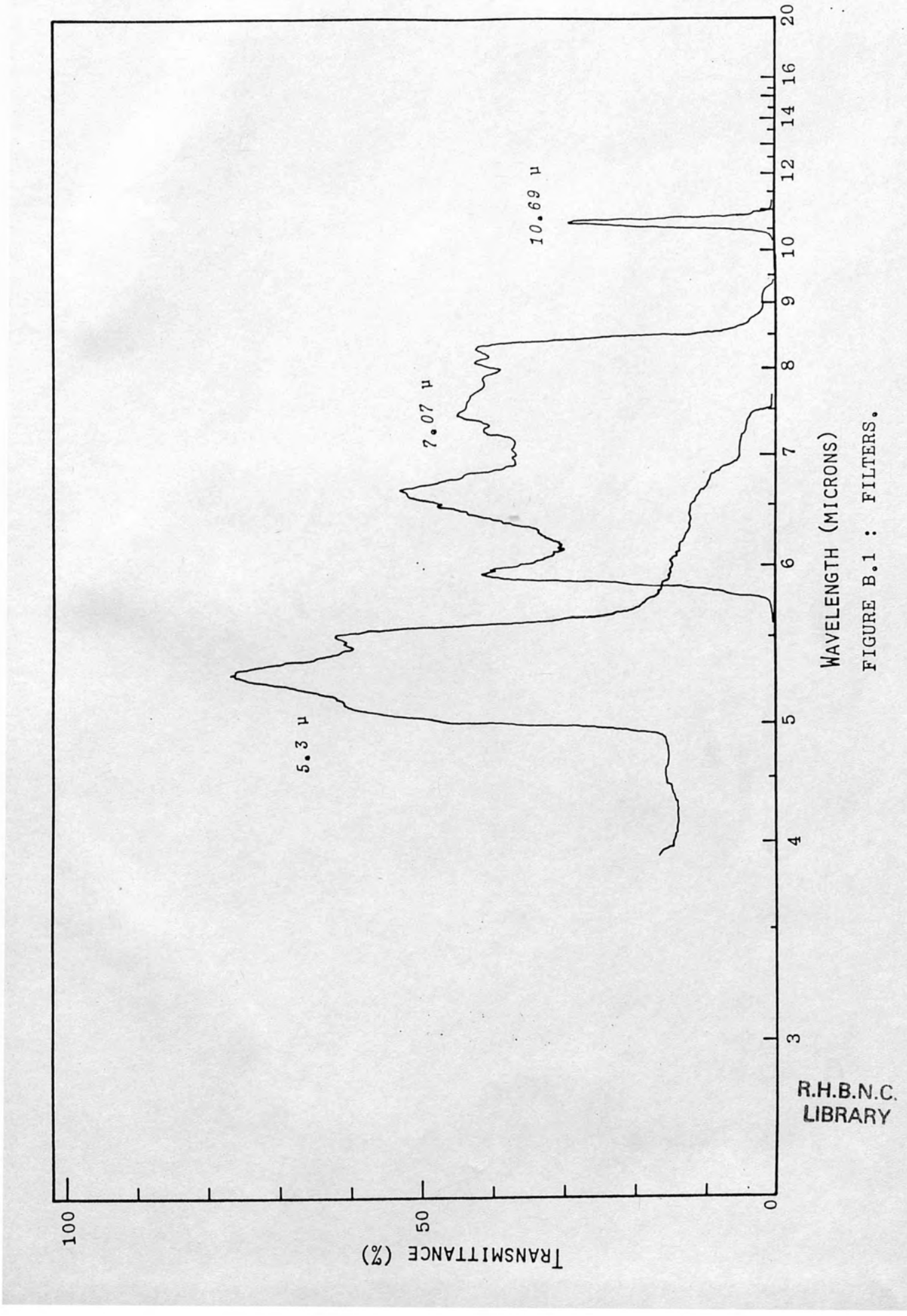

FIGURE B.1 : FILTERS.